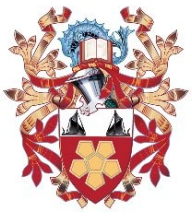

EST 1892

London South Bank University

Helicopter Main Gearbox Planetary Bearing Fault Diagnosis using Vibration Signal Processing Techniques

Linghao Zhou

Supervisors: Prof. Sandra Dudley
Dr. Fang Duan
External supervisor: Prof. David Mba

August 12, 2019

School of Engineering

London South Bank University

This thesis is submitted in partial fulfilment of the requirements for the degree of PhD

Acknowledgements

I would like to express my tremendous gratitude to the supervisory team, Prof. Sandra Dudley, Dr Fang Duan and Prof. David Mba, for their continuous academic support and motivation throughout the course of my doctoral study. Dr Duan has always been very helpful and approachable, she did her best to create a positive and professional environment, for which I will always be grateful. Prof. Dudley has been super understanding, and has provided me with all the supports so that I was able to focus on my study and work. Special thanks go to my external supervisor Professor David Mba, who has not only provided me the opportunity to conduct this study, but also has constantly enlightened me with insightful guidance, constructive comments and his profound knowledge.

Also many thanks to the sponsor organisation of this research, European Aviation Safety Agency (EASA), and my sincere gratitude to Dr Matthew Greaves and Dr Wenyi Wang, for kindly providing valuable helicopter gearbox data that were adopted to complete my study.

Many thanks to my colleagues and friends in London South Bank University, I will cherish the time we shared. Also, special thanks to my colleagues from TWI Ltd, who have been encouraging and motivating me to complete this thesis.

Last and most importantly, I would also like to thank my parents, who raised me with love and care, and are always there for me through up and down.

Abstract

Helicopters are extensively employed as versatile assets for military, transportation, rescue and many other utilities. A healthy and functional Helicopter Main Gearbox (MGB) is critical to ascertain the helicopter's system reliability and flight airworthiness, i.e. the suitability for safe flight. Therefore, it is of great importance to monitor the health status of the MGB. Currently, Health and Usage Monitoring System (HUMS), has been deployed on all medium and large size civil helicopters to perform MGB health status monitoring in United Kingdom. Nevertheless, HUMS has shown insensitivities and a lack of accuracy to detect planetary bearings-related defects, resulting in unfortunate accidents. Therefore, the successful diagnosis of planetary bearing defects in MGB could contribute profoundly to enhance sensitivity of HUMS against such defect type, thus improving helicopter flight safety, and reducing the overall maintenance costs.

This research aims at investigating the diagnosis of planetary bearing faults inside MGB using advanced signal processing techniques, providing diagnostic information that is more accurate and indicative against incipient planetary bearing faults. To fulfil the requirements, experimental work was undertaken on a commercial helicopter MGB to acquire invaluable vibration data. The MGB was operated under various load, speed and fault severities conditions. Diagnosis of the seeded planetary bearing faults was then successfully performed by evaluating and implementing various frequency domain processing techniques. Finally, further evaluation was conducted using another MGB dataset collected from a CH-46E Aft gearbox.

The results of this study have shown that applying various frequency domain signal processing techniques can effectively detect incipient planetary bearing faults. The main contributions of this research include acquiring data from a full scale helicopter main gearbox, proposing and evaluating a non-deterministic weak signature analysis scheme for MGB planetary bearings fault detection, and demonstrating using MGB carrier induced sidebands as a novel spectral feature for planetary bearing diagnosis.

List of Publications

Journal Publications:

L. Zhou, F. Duan, M. Corsar, F. Elasha, and D. Mba, "A study on helicopter main gearbox planetary bearing fault diagnosis," *Applied Acoustics*, vol. 147, pp. 4–14, 2019.

L. Zhou, F. Duan, D. Mba, W. Wang, and S. Ojolo, "Using frequency domain analysis techniques for diagnosis of planetary bearing defect in a ch-46e helicopter aft gearbox," *Engineering Failure Analysis*, vol. 92, pp. 71–83, 2018.

Conference Publications:

L. Zhou, F. Duan, D. Mba, and E. Faris, "A comparative study of helicopter planetary bearing diagnosis with vibration and acoustic emission data," in *2017 IEEE International Conference on Prognostics and Health Management (ICPHM)*, pp. 246–251, IEEE, 2017.

L. Zhou, F. Duan, E. Faris, and D. Mba, "Seeded planetary bearing fault in a helicopter gearbox—a case study," in *International Conference Design and Modeling of Mechanical Systems*, pp. 495–505, Springer, 2017.

L. Zhou, F. Duan, and D. Mba, "Wireless acoustic emission transmission system designed for fault detection of rotating machine," in *Advanced Technologies for Sustainable Systems*, pp. 201–207, Springer, 2017.

L. Zhou, F. Duan, D. Mba, M. Corsar, M. Greaves, S. Sampath, and F. Elasha, "Helicopter gearbox bearing fault detection using separation techniques and envelope analysis," in *2016 Prognostics and System Health Management Conference (PHMChengdu)*, pp. 1–5, IEEE, 2016.

A. Ricardo Mauricio, L. Zhou, D. Mba, and K. Gryllias, "Vibration based condition monitoring of helicopter gearboxes based on cyclostationary analysis," in *Proceedings of*

ASME Turbo Expo 2019 Turbomachinery Technical Conference and Exposition, ASME.

F. Duan, M. Corsar, L. Zhou, and D. Mba, "Bearing defect detection using envelope extraction for dimension reduction," in *Asset Intelligence through Integration and Interoperability and Contemporary Vibration Engineering Technologies*, pp. 137–145, Springer, 2019.

F. Duan, M. Corsar, L. Zhou, and D. Mba, "Using independent component analysis scheme for helicopter main gearbox bearing defect identification," in *2017 IEEE International Conference on Prognostics and Health Management (ICPHM)*, pp. 252–259, IEEE, 2017.

Acronyms

BPFI Ball Pass Frequency of Inner Race.

BPFO Ball Pass Frequency of Outer Race.

BSF Ball-spin Frequency.

CAA Civil Aviation Authority.

CBM Condition Based Maintenance.

CIs Condition Indicators.

CM Condition Monitoring.

DRS Discrete Random Separation.

DTFT Fourier Transform.

EASA European Aviation Safety Agency.

FAA Federal Aviation Administration.

FDR Flight Data Recording.

FFT Fast Fourier Transform.

FT Fourier Transform.

FTF Fundamental Train Frequency.

GMF Gear Mesh Frequency.

HARP Helicopter Airworthiness Review Panel.

HUMS Health and Usage Monitoring System.

IEC Iterative Envelope Cancellation.

IEPE Integrated Electronic Piezoelectric.

LMS Least Mean Square.

MGB Main Gearbox.

NASA National Aeronautics and Space Administration.

NRAD Naval Research and Development Centre.

PM Planned Maintenance.

QPC Quadratic Phase Coupling.

RMS Root Mean Square.

SANC Self-adaptive Noise Cancellation.

SK Spectral Kurtosis.

SPU Signal Processing Unit.

STFT Short-time Fourier Transform.

TSA Time Synchronous Averaging.

VHM Vibration Health Monitoring.

ZCT Zero Cross Time.

Contents

List of Figures

List of Tables

Chapter 1

Introduction

This chapter starts with providing the background of this study in Section 1.1, followed by the research aims and objectives described in Section 1.2. The structure of this thesis is outlined in Section 1.3.

1.1 Background

Modern helicopters are extensively employed for various civil and military tasks, due to their versatility and applicability. They are distinctively different from other types of aircraft, because of their special flying mechanisms and regimes, i.e. the special conditions under which the helicopter flies, as well as the capabilities of performing unique manoeuvres, including direct take-off and landing, hovering, flying backwards and sideways. The helicopter's transmission system is specially designed to achieve these functionalities. It transfers the power from engines to the rotor systems to generate the lift for take-off and to other accessory systems for flight control. The MGB is a key component in the transmission system as its primary purpose is to reduce the high output speed from engines to optimum rotational speed, thus providing adequate torque to drive the main rotors [1]. The ratio between the speed from engine and the speed from rotor shaft defines the reduction ratio. For more sophisticated MGB designs, the outstandingly high reduction ratio is achieved through the use of multi-stage epicycle speed reduction modules. An example of MGB two-stage epicycle modules is demonstrated in Figure 1.1. In this example, the ring gear at the bottom is fixed to the MGB housing. Input speed is firstly reduced through the 1^{st} epicyclic planetary gears, and then further reduced by the epicyclic train comprised of 1^{st} sun gear and 2^{nd} planetary gears. The 2^{nd} carrier plate which connects the 2^{nd} sun gear provides the output speed and torque to the

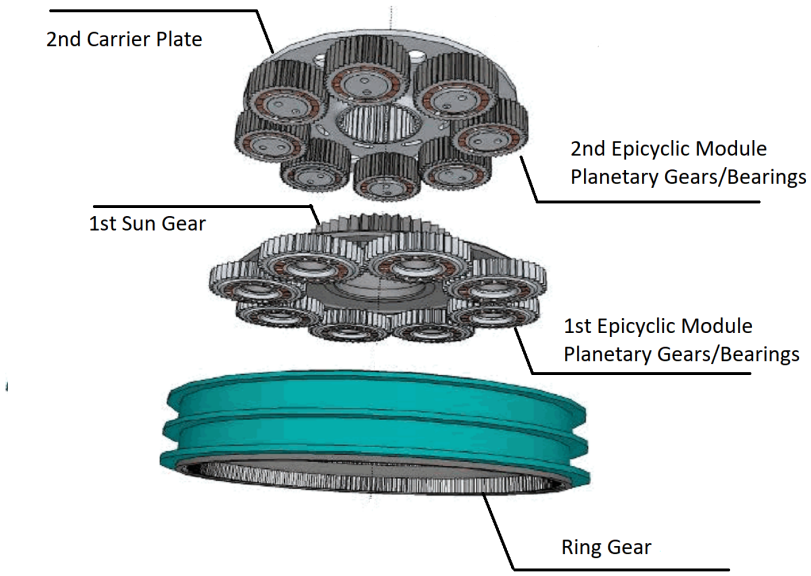

Figure 1.1: Two-stage epicyclic modules [2]

main rotor. The detailed discussion of two-stage epicyclic modules in MGB will be given in Chapter 3 when introducing the MGB adopted in this study.

The speed reduction ratio of the module illustrated in Figure 1.1 can reach 87 : 1, calculated with the output speed from engine to rotor. The requirements of achieving this ratio and the sophisticated structure of speed reduction modules determine that the rotating components such as planetary gears and bearings are under consistent mechanical stresses. Therefore, they are susceptible to cracks, material losses and bearing defects associated key failure modes that can lead to MGB failure, such as small corrosion pits induced cracks, small machining defects induced cracks, sub-surface cracks, gears/bearings spalling, wear due to variations of loads, fracture/deformation under overload and seizure of roller bearing [3]. In the unfortunate event of MGB failure, the helicopter could suffer a rapid loss of power, losing control of flight and eventually crash onto the ground, which endangers flight crew's lives and leads to immeasurable losses [4–6]. Therefore, it is absolutely crucial to monitor the status and conditions of critical helicopter transmission components, to avoid unexpected

helicopter unavailability, increase the flight operation safety and schedule proactive maintenance plans accordingly.

The investigation to develop such a helicopter monitoring system can be traced back to as early as 1982, when the Helicopter Airworthiness Review Panel (HARP) established the need for helicopter condition monitoring improvement [7]. The process was motivated and accelerated by a tragic North Sea accident in 1986 that took 45 lives. The cause of the accident was reported to be collision between de-synchronised rotors, due to a catastrophic failure in forward transmission [8]. Since then, the health and usage monitoring system, HUMS, came into being. In 1990, United Kingdom Civil Aviation Authority (UK CAA) made it mandatory to install Flight Data Recording (FDR) unit on medium and large civil helicopters to monitor aircraft flight status. In 1999, CAA made it mandatory for all heavy rotor-craft registered in the UK to install HUMS. Till this date, many types of HUMS designed by difference companies or organisations are on service, including HUMS from Eurocopter, GE Aviation, Goodrich and Honeywell [9].

HUMS provides two interconnected functionalities, namely health monitoring and usage monitoring. The focus of this research is HUMS helicopter health monitoring, achieved through employing Vibration Health Monitoring (VHM). The basis of VHM is to utilise the vibration data recorded during specific flight regimes to produce Condition Indicators (Condition Indicators (CIs)) by signal processing, which takes place either in on-board Signal Processing Unit (SPU) or at the helicopter ground base station. CIs are statistical parameters which represent the characteristics of the acquired vibration. Through long-term consistent monitoring, a baseline or healthy condition can be established. Deviations to the established healthy condition observed in CIs progressions or breaches to pre-determined CIs threshold usually can be correlated to helicopter system defects. Recommended in Civil Aviation Authority (CAA) issued file CAP 753 [10], vibration data are sensitive to flight regimes, for this reason, it may be desirable to focus data acquisition to particular operating conditions or phases of flight. This also allows the vibration data to be analysed and compared under a similar regime to establish whether a deviation exists from normal condition over time [2].

The deployment of HUMS has brought evident benefits. In [7, 9, 11] the authors all agree

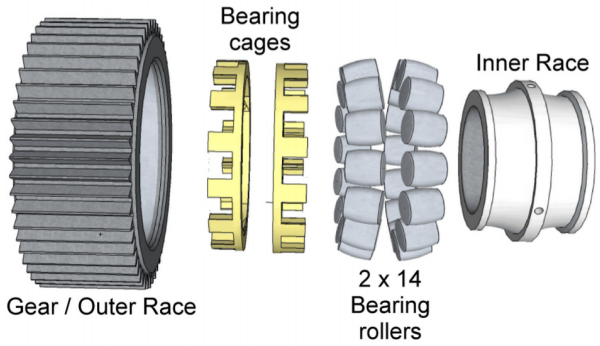

Figure 1.2: MGB planetary gear/bearing [2]

that HUMS' improvements mainly focus on, but not limited to, increasing the aircraft safety and availability, supporting maintenance decision-making, and reducing overall cost. However, concerns exist over the efficacy and validation of HUMS. In 1994, K.F. Fraser expressed uncertainty on using HUMS to monitor multiple drive path components such as epicyclic gears and bearings, whose transmission paths vary continuously. What's more, the helicopter accidents related to MGB malfunctioning happened in recent years have shown that HUMS was insensitive to MGB failure associated with planetary bearings. Some notable accidents are G-REDL (accidents registration number, same hereafter) accident in 2009 [2], G-REDW accident in 2012 [5], and LN-OJF accident in 2016 [6]. In all these accidents, HUMS was either unable to produce meaningful warnings or only able to sense anomalies seconds before completely lost of aircraft control.

Several issues have been identified from reviewing aforementioned accident reports and the discussions with experts from EASA. Firstly, vast majorities of the CIs and analysis are developed and performed with a focus on gear-associated mechanisms, which explains the insensitivities to bearing faults. Such as described in the G-REDL helicopter accident report [2] that only gear associated CIs had pre-set thresholds. The reports also make the recommendation to EASA to research methods for improving the detection of component degradation in helicopter epicyclic planet gear bearings (Safety Recommendation 2011-041). What's more, vibration data is highly modulated by the constant varying transmission paths, due to the sophisticated epicyclic modules. The signal modulation also comes from the unique structure of planetary bearing shown in

Figure 1.2, where the bearing is encircled by the gear, making the gear's inner race also the outer race of the bearing. Therefore, the signals associated with bearings are modulated by the gears during planetary movement. This in turn affects CIs' capabilities of distinguishing two different signals that have similar overall statistical features, making the diagnosis of planetary bearing faults exceedingly challenging. It is noteworthy that the fault originated from the outer race area of the planetary gear/bearing set was the root cause of G-REDL and LN-OJF accidents [2, 6]. Therefore, the planetary bearing outer race fault is of particular interest in this study.

Apart from the CIs and fault mechanism, another detrimental aspect is that MGB's operation produces overwhelming noises, which mask the fault-related signatures and hinder HUMS' effectiveness. It is generally recognised that, frequency domain based signal processing techniques offer powerful filtering capabilities to cope with overwhelming noises and interferences, however, no detailed frequency analysis that is capable of de-noising, demodulation and feature extractions has seen incorporated into development of CIs [12–14], which is also agreed and recommended investigating on from the EASA expert opinions.

1.2 Aims and Objectives

Planetary bearing faults lead to MGB failure, which could result in catastrophic helicopter accidents. Therefore, it is essential to identify possible incipient fault prior to its propagation, thereby improving the overall airworthiness of the aircraft, preventing secondary damage to the other transmission components, and reducing the maintenance cost. Although HUMS has been widely implemented, accidents reports and expert opinions have indicated the needs to investigate on improving its effectiveness against planetary bearing outer race faults, as described in Section 1.1. Therefore, the primary goal of the work presented in this thesis is to study the existing signal processing techniques that offer de-noising, demodulation and signature extraction capabilities to diagnose planetary bearing faults. To fulfil this goal, in addition to studying the state-of-art frequency domain signal processing techniques for bearing fault diagnosis, it is also desirable to undertake experiments of seeded incipient planetary bearing outer

race faults. The experiments contribute profoundly to develop the knowledge on diagnosis of incipient planetary bearing fault under relatively low speed and light load operational conditions, comparing with the research published in [3], which was conducted under severe bearing cracks and extreme loading conditions of MGB. The objectives of this study are elaborated below.

- Investigating the frequency domain signal processing techniques that offer de-noising, gear/bearing signal separation, signal demodulation, and fault-feature extraction. Discuss in detail the theory and evaluate the effectiveness of applying these techniques to planetary bearing diagnosis.
- Undertaking seeded defect tests on real helicopter MGB to collect experimental vibration data. Different test conditions should be carried out in terms of MGB operating speed, load coupled with 2^{nd} epicyclic sun gear, and the severities of outer race defects.
- Applying the selected signal process techniques for planetary bearing fault diagnosis, and validating their effectiveness for the seeded fault. Developing frequency domain signal processing routines that are optimal in diagnosis of incipient planetary bearing faults.
- Conducting comparative studies using helicopter MGB data from a CH-46E helicopter aft MGB.

1.3 Thesis Outline

The rest of the thesis is organised as follows.

Chapter 2 presents the basis of vibration health monitoring, commonly applied CIs, as well as the literature review of the state-of-the art frequency domain based signal processing techniques that benefit bearing fault diagnosis. Chapter 3 describes the details of seeded planetary bearing fault experiment undertaken in SA330 Super Puma MGB. In this Chapter, the experiment rig setup is firstly presented. The seeded defects and the setup of data acquisition are described, followed by the reporting of test conditions and procedures. In the experiment, invaluable vibration data has been recorded from various

test conditions, for post-processing. Chapter 4 details the diagnosis work for the data collected from seeded planetary bearing fault experiment. This chapter will discuss the diagnosis of seeded planetary bearing fault, using the vibration data collected under four different test conditions. Chapter 5 investigates a comparative study using the vibration data collected on a CH-46E helicopter aft gearbox, further validating the results concluded from Chapter 4. Finally, in Chapter 6, the presented work from Chapter 2 to Chapter 5 are summarised. Discussions over the future work that extends this research will also be given in this Chapter.

Chapter 2

Literature Review

2.1 Introduction

This chapter presents a comprehensive literature review on the basis of vibration-based condition monitoring, fundamentals of applying vibration for condition monitoring in HUMS, and details on frequency based signal processing techniques that meet the requirements listed in Chapter 1.

2.2 Vibration-based Condition Monitoring

The rotating machineries have far-reaching applications all over the world and across various industrial sectors. With the ongoing acceleration of technological advancements, the design of the rotating machineries is becoming increasingly complex [15], with lighter and possibly faster rotors, more sophisticated power transmission structures, hence tighter tolerances to mechanical defects. Due to the constant operation under mechanical stresses and/or varying loads in the real environment, rotating machineries are subject to components deterioration and mechanical failure. Therefore, maintenance for a rotating machine is key to ascertain the machine's reliability and maximise the availability, thereby reduce overall cost.

It has been stated in [16] that the first form of maintenance was simple "Breakdown" maintenance, meaning keeping the machine running until failure, only at which point the maintenance would take place. This form of maintenance was incompetent to take actions before failure occurs, thus it was also called "Unplanned" maintenance. An improvement strategy named "Time-based" maintenance or Planned Maintenance (Planned Maintenance (PM)), is to schedule the maintenance based on a recursive time

interval, which partially addresses the issues with breakdown maintenance. However, PM has the limitation of being unaware of the machineries' status and conducting maintenance regardless of their health status, which inherently increases maintenance cost. Modern sensory technology has facilitated a more efficient maintenance strategy, namely condition-based maintenance (Condition Based Maintenance (CBM)). CBM is a preventive maintenance strategy that provides the access of condition or health status information through the employment of sensors, therefore supporting the development of proactive maintenance schedule at the optimal time. Based on the condition-monitoring information, CBM improves the reliability of engineering system [17].

Condition monitoring (Condition Monitoring (CM)) is an essential part of CBM. By installing various sensors and employing a data recording scheme for a certain time period, the baseline or general conditions of the rotating machinery can be established by data processing. CM enables the fault diagnosis possibilities by comparing the established baseline conditions and the subsequent conditions with the progression of time. Deviations of subsequent conditions to baseline or healthy conditions may indicate the existence of potential defects in the rotating system, which could be confirmed with the combination of other system usage information and/or inspections. This is also the basic concept of utilising CIs, which represent a certain condition, to monitor the progression of helicopter's transmission and identify early signs of defects.

There are great numbers of methods that promote the implementation of CM. In [18], it is detailed that vibration, oil analysis, performance analysis and thermography are all widely applied for CM. However, it is also pointed out that, if the monitoring purpose is to be mindful of the internal information from the external monitoring methods while the machines are rotating, two main analysis methods are vibration analysis and lubricant oil analysis. Although lubricant oil analysis could be a decent technique to monitor the overall health conditions of the MGB, it has many limitations to be adopted for planetary bearing fault diagnosis. Firstly, oil analysis cannot reveal the fault locations or fault types inside the MGB; secondly, oil analysis cannot be performed in real-time, the gearbox must be shut down before the inspection; and lastly, if there is no material loss when the defects are propagating, oil analysis will be ineffective. Due to these limitations, oil analysis is

not a competent candidate to diagnose MGB planetary bearing fault, whereas vibration analysis is a suitable candidate. The reasons are discussed in the following paragraphs.

Vibration is a physical phenomenon that presents in operational rotating machineries regardless of their health conditions. Vibration can be induced by various sources in rotating machineries, including rotating shafts, meshing gear-teeth, rolling bearing elements, rotating electric field, fluid flows, combustion events, structural resonance and torsional vibration, i.e. angular rotations induced vibration [18–20]. Because of its ubiquity in all parts of the machine, vibration is highly applicable as the source for investigating the operational conditions and status of rotating machinery.

Besides its inherent applicability, vibration analysis becoming the most prevalent methods for condition monitoring is also owing to its three advantages over other methods. First of all, vibration reacts almost instantly to any differences induced to the rotating system, either because of the change of operating conditions, environmental aspects or faults. This is in contrary to slow reactive method like thermography, brings benefits of faster faults indication. Secondly, the fast development of modern sensory technology has indubitably promoted the implementation of vibration-based CM. As of now, there are massive amounts of accelerometers available on the market, satisfying different requirements such as dynamic range, flat frequency responses bandwidth, sensitivities, temperature ranges, mount type, enclosure size, materials and number of measuring axes. The widely approved Integrated Electronic Piezoelectric (IEPE) accelerometer standard has also contributed to the increasing popularity of vibration analysis. IEPE accelerometers are piezoelectric accelerometers packed with built-in charge or voltage amplifier that transforms the high impedance signal from the piezoelectric material to a low impedance voltage signal. Last but most importantly, as stated in [18], vibration data has enabled many powerful frequency domain based signal processing techniques to be applicable, which facilitate the diagnosis of rotating machinery faults.

As already stated in previous paragraph, the sources of vibration in a running rotating machine are mostly associated with components relative movements, contacts or meshing with each other. These activities are highly likely to be phase-locked with the shafts which

the components are attached to, that is, the speed of the meshing or rotating components are linearly related to the shaft speed. Therefore, the vibration signal obtained from one single accelerometer are usually the mixture of many vibrations induced by repetitive rotating activities. This is specifically true in a MGB, where dozens of gears are meshing together alongside the bearing rolling and shafts rotating simultaneously, to achieve power transmission, as showcased in Figure 1.1 in Chapter 1.1. Therefore, when examining the time-domain information of the acquired vibration signal, the vibrational information that associated with specific rotating component will inevitably be obscured by other vibration activities and/or noises. The use of frequency analysis allows the detailed examinations on the vibration event that are associated with repetitive rotating, and extracts the hidden information associated with the repetitiveness.

The foundation stone of frequency domain analysis is the Fourier Transform (FT). FT is a method of signal decomposition, which converts the signal from time domain to frequency domain. This leads to the original signal as a function of time, to become a complex-valued function of frequency. The most common equation of FT for a continuous signal is given in Equation 2.1:

$$X(f) = \int_{-\infty}^{\infty} x(t) \times e^{-j2\pi ft} dt \tag{2.1}$$

where $X(f)$ denotes the frequency contents transformed from a function of time $x(t)$, and t is the continuous time. f is usually expressed in unit of Hz, which represents "cycles per seconds". This is very intuitively related to the rotating speed of shaft, gears and bearings in a rotating machine.

Due to that the continuous waveforms sensed by accelerometers are analogue, they must be digitalised to discrete sequences in order to be stored for digital analysis. According to the Nyquist Theorem, which is also known as the sampling theorem, to acquire a meaningful reproduction of the analogue signal, the number of samples that are digitalised per second should be at least twice the highest frequency contained in the analogue signal. The number of samples per second is called the sampling rate or

sampling frequency. Considering the discrete time signal, Equation 2.1 is modified to its discrete version, called Fourier Transform (DTFT):

$$X_k = \sum_{n=0}^{N-1} x[n] \times e^{-\frac{j2\pi}{N}kn}, \qquad \text{k = 0, 1, ..., N-1} \tag{2.2}$$

where $x[n]$ is the sampled discrete set of real numbers for all integer n. X_k is the corresponding Fourier Sequences of size N. It can be derived from Equation 2.2, that the computational complexity is $O(N^2)$, where O means the steps performed for computation. $O(N^2)$ reflects that there are N outputs, and each requires a sum of N terms. The most adopted fast computational Fast Fourier Transform (FFT) algorithm proposed by Cooley and Tukey in 1965 [21] managed to reduce the operations required to $O(N\ logN)$ [22], which enormously increased the estimation speed of DTFT for discrete time series. This opens up the possibilities of using modern computer and more complex processing techniques for signal post analysis.

An example of the effectiveness of frequency signal analysis is given in Figure 2.1, where the comparison between two simulated signals is presented. In Figure 2.1(a), a simple 10 Hz sinusoidal wave is plotted. As stated already, Hz is the unit describing the number of repetitive revolutions occur in 1 seconds, in this case the sinusoidal wave occurs 10 times continuously. In Figure 2.1(b), the same signal is mixed with a simulated random noise which has overwhelming amplitude comparing to the sinusoidal wave, therefore it is evident that the pure repetitiveness pattern in the sinusoidal wave has been massively covered, and the original periodic characteristic in time domain is barely observable.

In contrast, both the original pure 10 Hz sinusoidal wave and the noisy signal are processed with FFT using MATLAB signal processing toolbox. The results of their frequency sequences are plotted as amplitude frequency spectrum. Figure 2.2(a) is the original signal's frequency spectrum, where the 10 Hz is distinctly shown. Figure 2.2(b) on the other hand, despite the pollution from the added noise, the 10 Hz frequency is still evident. This unique feature enables various frequency filters to be developed, that are capable of filtering unwanted frequency contents, while reserving the most of the

frequency of interests. It is worth noting that the frequency amplitude of the signal in Figure 2.2(b) is larger than that in Figure 2.2(a). This increase in amplitude is induced by the added random noise, whose energy is constantly distributed in frequency domain. Frequency spectrum analysis is also capable of extracting the fault related frequencies, for example, deviations of frequency components in faulty gears (tooth missing or cracking) to the normal periodic meshing spectrum; rollers of bearing periodic contacting the outer race cracks while rotating and many other scenarios.

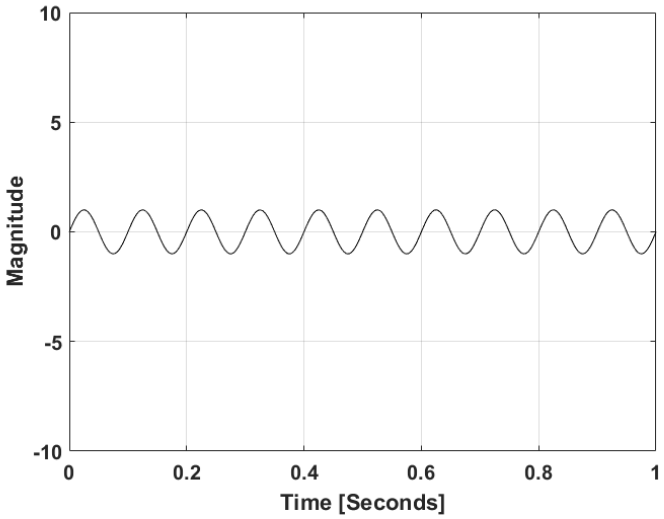

(a) Simulated 10 Hz signal

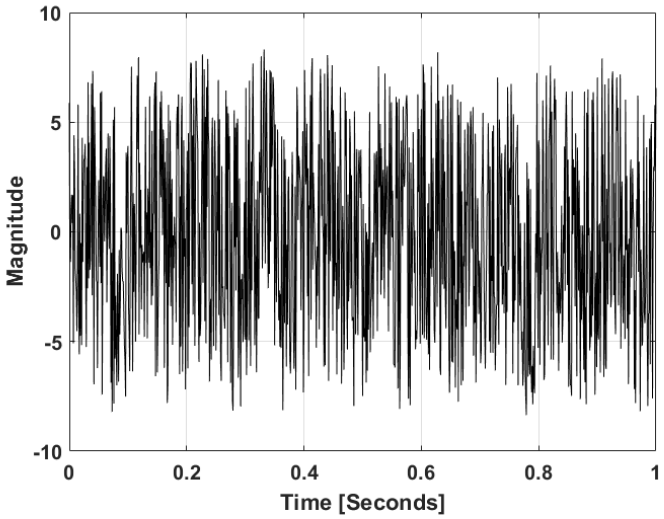

(b) Simulated 10 Hz signal with random noise

Figure 2.1: Comparison between raw and noisy time waveforms

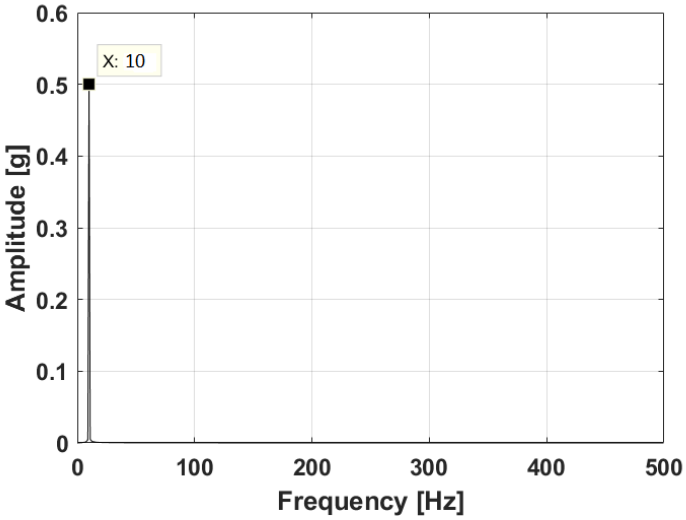

(a) Frequency amplitude spectrum of 10 Hz signal

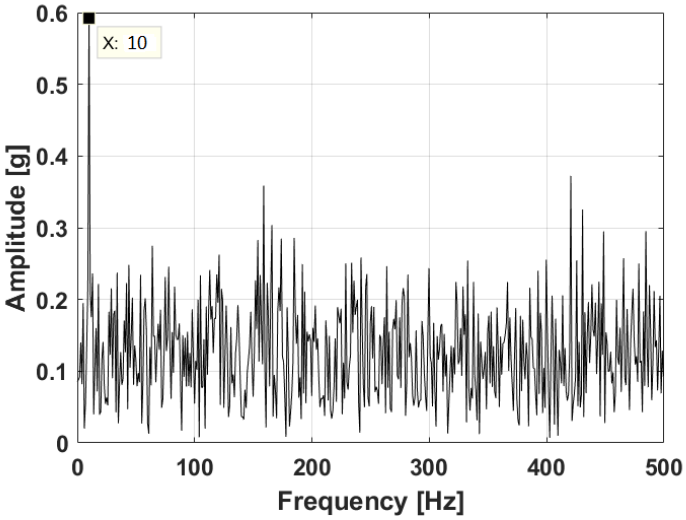

(b) Frequency amplitude spectrum of 10 Hz signal with added noise

Figure 2.2: Amplitude spectrum of raw and noisy time waveforms

2.3 Vibration Health Monitoring Employed in HUMS

2.3.1 Introduction

The importance of CBM and CM using vibration analysis explained in Section 2.2 has been taken upon and elevated to a momentous consideration in this study, that is, the flight safety and aircraft airworthiness. It is therefore particularly important to firstly develop

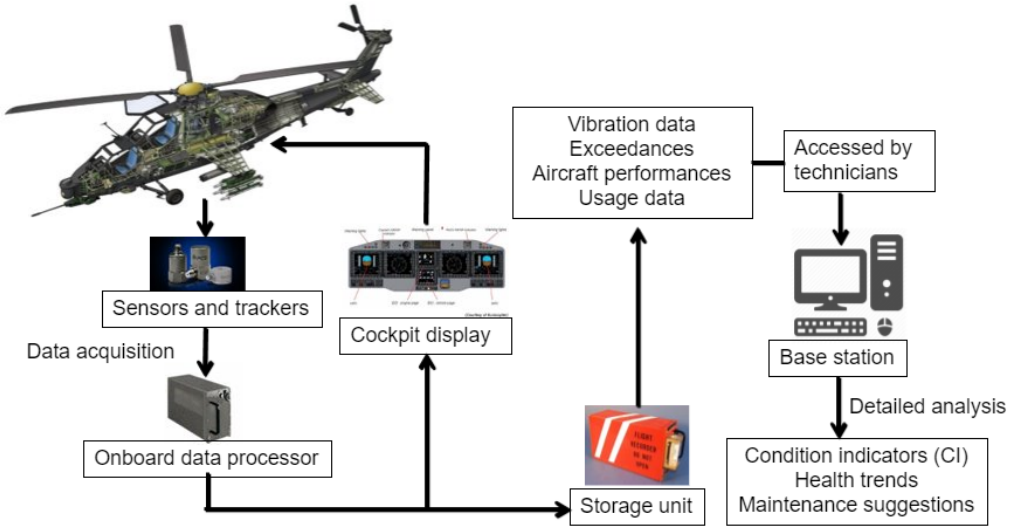

Figure 2.3: HUMS schematic diagram

the knowledge of how Vibration Health Monitoring (VHM) is implemented currently in HUMS. The main resources for this part of the review are research report from EASA [3], CAA issued papers [10,23,24], studies of HUMS [7,23,25,26], and also information from the helicopter accident reports [2, 4, 6, 8].

As stated in Chapter 1.1, the history of HUMS can be traced back to 80s, and the development of HUMS was unfortunately accelerated by a tragic offshore helicopter crash that caused 45 casualties [7]. In [3], an overview of current VHM implementation was presented, summarising that organisations including UK CAA, the US National Aeronautics and Space Administration (NASA), Federal Aviation Administration (FAA) have conducted various surveys to evaluating the effectiveness of HUMS and the method of applying vibration analysis based monitoring programme for drivetrain system health monitoring [27–30].

Figure 2.3 depicts the general process of the working principles of HUMS. By employing multiple sensors and system performance trackers, various kinds of data is either processed for cockpit display or stored to be processed in detail at the ground base station, where the CIs trends are inspected. Within HUMS's working process shown in Figure 2.3, VHM acts as a key technology in collecting vibration data from critical rotary parts and performing the detailed analysis. An example of the VHM in real HUMS was reported in the research published by JW. Bristow [31], where a system

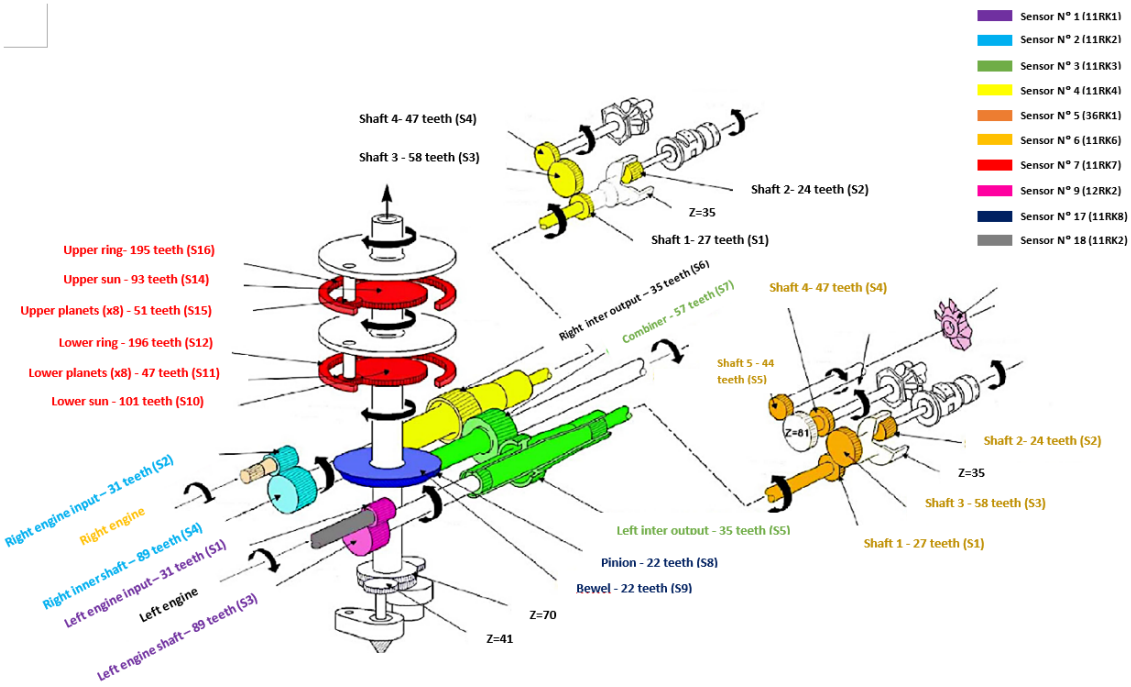

Figure 2.4: Drive train monitoring of EuroHUMS [2]

overview was illustrated, highlighting the functionality included in HUMS of "gearbox vibration analysis".

In the following paragraphs, the principles of accelerometer locations, recording scheme are discussed. Firstly, in terms of the accelerometers locations, Figure 2.4 has shown that 18 accelerometers have been employed across the main rotating parts on the drivetrain, including input shafts from engine (purple and cyan); 1^{st} and 2^{nd} planetary modules (red); right and left output shafts (green and yellow, respectively); and tail gear and shaft systems (dark orange). MGB epicyclic modules are also labelled red in Figure 2.4.

The standard document CAP 753 [10] also listed the instructions on sensory installation, suggesting "the location of sensors and the method of installation have a significant effect on monitoring performance. The design selected should be investigated to confirm that the processed vibration signal-to-noise ratio is acceptable and that it is capable of discriminating the features required to identify potential incipient defects from monitoring".

The data recording scheme has been instructed that "at least the data set for all components

should be automatically obtained on each flight of greater than 30 minutes in stabilised conditions without the need for in-flight pilot action", which is sensible to establish a long-term monitoring. The main signal processing in HUMS is reflected on the procedures of producing CIs, which is reviewed in the next Section.

2.3.2 Condition Indicators Reported in Literature

HUMS is employed to collect all kinds of sensory information, which is then processed and combined to reflect health state of the monitored key components. Condition indicators (CI) are statistical indicators produced from processing HUMS sensory information to assist machinery fault identification. Since Steward proposed useful indicators such as FM_0 and FM_4 in 1977 [32], CIs have been developed rapidly, although most of CIs aim for gear fault detection. Numerous researches have been conducted on this topic. In [20, 33–38], procedures and calculations of common CIs are summarised, tests and validations with experimental data are reported. Various CIs were evaluated and compared in terms of availability, fault response and false positives in study [39]. Specifically, the oil cooler bearing CIs are tested and compared in [40] .

Generally, three types of data are used to generate CIs, namely raw data, residual data and difference data. Raw data is referred to unprocessed vibration data, while residual data is produced by removing drive shaft frequency, gear mesh frequencies as well as their 1^{st} and 2^{nd} harmonics from time synchronised raw data. A difference data is generated by further removing 1^{st} sidebands from residual signals. Global CIs generated from raw data such as RMS value, PP (Peak-to-peak), kurtosis are great for general health indication, but not so effective on incipient defects monitoring. To overcome disadvantages of global CIs, more complicated CIs are developed using residual and difference data. The concept of kurtosis, with certain modifications, is applied extensively in developing these complicated CIs, such as FM_0, FM_4, NA_4, NB_4 and so on, due to its capability of describing how flat or peaky the data is. Traditionally recognised CIs are listed but not limited in Table 2.1 ([41]).

Time Synchronous Averaging and Order Tracking

Table 2.1: Vibration condition indicators

Shaft CIs	Asynchronous/ Synchronous Shaft Order 1, 2, 3 Synchronous Averaged RMS Synchronous Averaged Peak to Peak Synchronous Averaged Kurtosis	
Gears CIs	Residual Kurtosis Residual RMS Sideband Modulation Narrowband Crest Factor Gear Distributed Fault G2-1 Residual Peak to Peak Energy Operator Sideband Index Sideband Level Factor FM0	FM4 & FM4* Energy Ratio M6A & M6A* M8A & M8A* NA4 & NA4* NA4 Reset Amplitude Modulation Phase Modulation Instantaneous Frequency NB4 & B4* NP4
Bearings CIs	Envelope Energy Peak Pick Synchronous Averaged Peak to Peak Frequency Band Energy	

Time Synchronous Averaging (TSA) plays an important role and is extensively applied to calculate various CIs. TSA is described in [42] as an essential algorithmic tool for determining condition of rotating machinery. TSA has been established as a very effective way on extracting repetitive signatures even with large noise for a long time [43, 44]. In practice, TSA is achieved by dividing raw data into segments, where all segments are extracted correspondingly to a specific time record length, whose reciprocal is the gear mesh frequency of interest, i.e. these segments are time synchronised. These data segments may have different data points because of rotational speed fluctuation, thus they are interpolated to contain same integer numbers of data points, and then averaged to produce TSA signal. The TSA process is modelled in equation below [45]:

$$y(t) = \frac{1}{N} \cdot \sum_{n=0}^{N-1} x(t + nT) \tag{2.3}$$

Equation 2.3 describes the filtering process of TSA, which can be modelled as the convolution of raw signal $x(t)$ with N delta functions displaced by integer multiples of time T. Through this process, only the selected frequencies and their corresponding harmonics are retained, while the other frequencies associated components are suppressed. McFadden in [43] described the effect of TSA in frequency domain as a "comb filter ", the higher the value of N is, the better the noise-rejection effect will be. The comb effect of TSA process frequency selectivity is demonstrated in Figure 2.5, where the frequency is converted from Hz to orders, i.e. integer multiplies to the fundamental frequency $1/T$. The Figure demonstrates the TSA process of retaining 8 orders of the fundamental frequency, while suppressing the other frequencies in the spectrum.

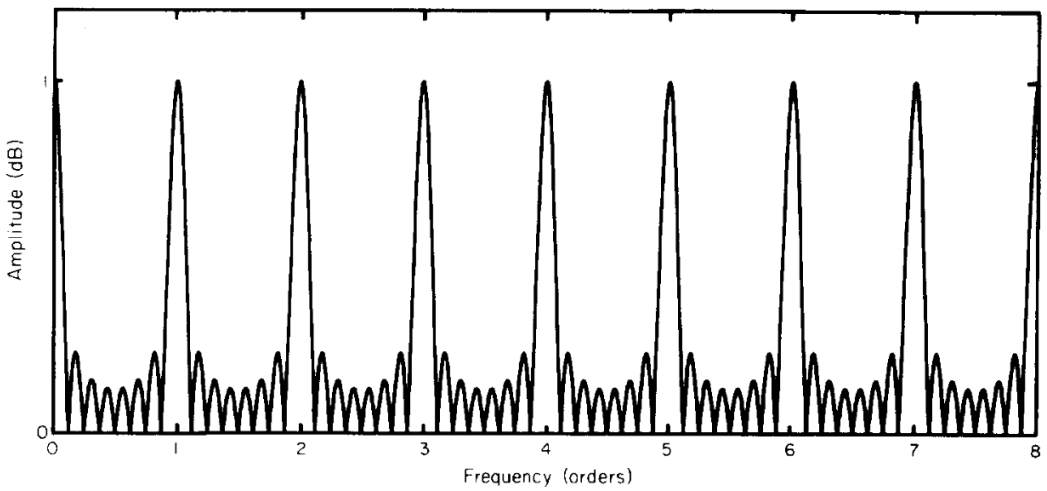

Figure 2.5: TSA filter effect of retaining 8 orders of the fundamental frequency [43]

Order tracking is usually discussed in parallel with TSA simply because that order tracking can be seen as one step of the TSA process. As mentioned before, a successful TSA requires one to know the accurate rotating phase-time information, and guarantee the minimum speed fluctuation. Order tracking is thus used to smooth out the speed fluctuation. As speed fluctuation could also bring in ripples or "smear effect" in frequency domain, hindering fault identification, order tracking is also commonly used independently purely for the purpose of data pre-processing to increase data signal-to-noise ratio. Order tracking is usually achieved by interpolation, which is used to resample data in angular domain, making sure that for every revolution of the shaft,

same integer number of data points are captured regardless of the rotating speed fluctuation. In [46, 47] the effect of order tracking and a very complex computational method for calculating order tracking was presented. Idehara et al. presented and compared different order tracking procedures in [48]. However, in practice, performing order tracking is simpler and approachable. A pseudo code for performing TSA and order tracking with the help of tachometer signal was proposed in [42]:

1. Calculate the Zero Cross Time (ZCT), which is the time when the tachometer readings changed from 1 to 0.
2. For the shaft of interest, interpolate current ZCT_i and ZCT_{i-1} based on gear ratio.
3. Calculate time intervals $dZCT_i$, from the difference of ZCT_i and ZCT_{i-1}.
4. Calculate the resample times, $\frac{dZCT}{N}$, where N corresponds to the largest number of data points among the time records $dZCT_i$ so that minimum speed is guaranteed to avoid data loss.
5. Interpolate data based on information gathered above (Order tracking finished at this step).
6. Accumulate resampled time domain data for M repetitions.
7. Average the accumulated data by M.

When that tachometer signal is not available, demodulating vibration data (acceleration) and utilising speed-related frequency components or their higher harmonics to estimate instantaneous rotating speed could be a possible solution. In [42, 49] and [50], such method was discussed. Summarising these papers, algorithmic steps for estimating instantaneous rotating speed using vibration signal are:

1. Examine high resolution amplitude spectrum of the vibration signal, select the frequency components that related to shaft speed of interest. Noted that in some occasions 2^{nd} or 3^{rd} harmonics may have higher signal-to-noise ratio (SNR) than the fundamental frequency components [42].
2. Bandpass the selected frequency components with appropriate bandwidth. The rule of thumb for selecting bandpass bandwidth is that: the band should be adjusted so as to keep the meshing frequency only, and to remove all parasite frequencies [49].

3. Demodulate the bandpass filtered signal. A convenient method is applying Hilbert Transform, so that the bandpass filtered signal is transformed to analytic signal. Unwrapped instantaneous phase ω of the bandpass filtered signal can be extracted from its analytic transformation.
4. Calculate instantaneous speed (represented by frequency f_{speed}) using equation: $f_{speed} = \omega/(2\pi)$.

It should be noted that this method cannot guarantee an accurate speed estimation if the speed fluctuation is large. In [49], Bonnardot stated that the maximum speed fluctuation is decided by:

$$\delta_{fmax} = \frac{f}{1+2mT_{max}}, \tag{2.4}$$

where f is the minimum average shaft speed, m is the order of selected harmonic, and T_{max} is the number of teeth of driven wheel.

The drawbacks of TSA and order tracking method are mentioned in [51]. TSA is highly dependent on the prior knowledge of the time period of interest T, which is commonly gathered from phase marker or tachometer that is synchronised to drive shaft. If the knowledge of accurate rotating shaft phase-time map is unknown, Randall citeRandall2011 stated that even 0.1% of speed fluctuation will cause jitter of typically 1K data points. Another problem of applying TSA that being talked a lot, especially in the area of bearing defect diagnosis, is that the TSA comb filter can only bandpass one set of frequency component and its harmonics. It could be a tedious job to apply TSA for separating nondeterministic (i.e. random) bearing signal, and deterministic (i.e. periodic) gear signal. The reason that bearing signal is not considered to be pure periodic is due to the randomness induced by the inherent slip of the rollers.

Demonstration of CIs

Some popular CIs shown in literature are introduced hereforth.

Root Mean Square (RMS) has been widely applied as an overall indicator for condition

monitoring. It represents the effective value of the signal within a certain time period. Given a set of n discrete signal $x_1, x_2, ..., x_n$, the corresponding RMS of this signal is:

$$x_{RMS} = \sqrt{\frac{1}{n}(x_1^2 + x_2^2 + \cdots + x_n^2)} \tag{2.5}$$

The downside of RMS is that, it is insensitive to incipient faults whose amplitude is not enough to emerge through the averaging process of RMS. RMS is also applied as a prerequisite for other CIs, such as:

$$CF = \frac{S_{PP}}{S_{RMS}}, \tag{2.6}$$

where CF is short for crest factor, S_{PP} is peak-to-peak (PP) signal and S_{RMS} is root-mean-square signal. From the definition we can gather that the idea of CF is evaluating the weighing of PP value against total rms value of the signal. CF has the similar problems as RMS, that is, if the noise or interferences are overwhelming and determining the peak amplitude, the fault associated signals will not be detected.

The zero-order figure of merit (FM_0), can be calculated by:

$$FM_0 = \frac{S_{PP}}{\sum_{i=1}^{N} A(i)}, \tag{2.7}$$

where $A(i)$ is the i^{th} mesh frequency harmonics. Compared with CF, FM_0 focuses on the energy spread on tested gears' harmonics. As suggested from the definition, FM_0 is designed to detect gear-associated faults.

Energy ratio (ER) is given by:

$$ER = \frac{\sigma(d)}{\sigma(r)}, \tag{2.8}$$

where r and d represent residual data and difference data respectively. The idea of ER

is that as crack propagates, signal energy is transferred from regular meshing signals to wider signal band. Hence ER could be utilised as an indicator for severe wear. However, in the early development stage of the bearing fault, due to its negligible signal energy, not much information will be passed on to wider signal spectrum.

Kurtosis is defined as:

$$Kurtosis = \frac{N \cdot \sum_{i=1}^{N} (S_i - \bar{S})^4}{\left[\sum_{i=1}^{N} (S_i - \bar{S})^2\right]^2}, \tag{2.9}$$

where N is the number of data points, S_i is the i^{th} point of data S. $\bar{S}$ is the mean of the data set. Kurtosis is hence described as fourth centralised moments, normalised by the square of variance. Similarly, with difference signal d rather than raw data S, we can calculate FM_4:

$$FM_4 = \frac{N \cdot \sum_{i=1}^{N} (d_i - \bar{d})^4}{\left[\sum_{i=1}^{N} (d_i - \bar{d})^2\right]^2} \tag{2.10}$$

The difference signal of gearbox in a good condition is assumed to be primarily Gaussian distributed [52]. Therefore when defect occurs, large peaks are likely to emerge in difference signals. However, FM_4 and kurtosis are all reported to only effectively detect damage on limited number of gear teeth [35]. As the defects propagate, series of large peaks are generated and the overall waveform becomes flat. FM_4 and kurtosis hence decrease, providing obscure information.

NA_4 is developed to address the aforementioned issues of kurtosis and FM_4. It is defined as:

$$NA_4 = \frac{N \cdot \sum_{i=1}^{N} (r_i - \bar{r})^4}{\left[\frac{1}{M} \cdot \sum_{j=1}^{M} (\sum_{i=1}^{N} (r_i - \bar{r})^2)\right]^2}, \tag{2.11}$$

where r is residual data, M is the total number of data sets that are used for variance averaging in denominator. By averaging variances of different sets of data within the same data records, the value of NA_4 can increase when multiple cracks occur. A very intuitive diagram of generating CIs is provided in [38] and illustrated in Figure 2.6, which represents the general procedures of the CIs described above.

The efficacy of CIs on different types of defects and CIs' issues have been discussed in large numbers of researches. Zakrajsek et al. compared FM_0, FM_4, NA_4 and many others using experimental gear pitting fatigue crack data, reaching a conclusion that FM_4 and other kurtosis concept based CIs all lost sensitivity to defects when they propagated [33]. Antolick [39] reported that FM_4 was not effective to be adopted as a consistent diagnosis indicator. NA_4 was effective but data burdensome. Sideband index, which is defined as the average amplitude of the sidebands of the fundamental gear mesh frequency, was effective at spiral gear sets fault detection. In [38], the authors conducted research using gearbox vibration data, and stated that neither kurtosis nor skewness followed fault trends, other CIs such as NA_4 and FM_4 showed 60% false positives. Additionally, CIs that specifically target bearing defects draw much less attention. In G-REDL accident investigation report [2], it is stated that no online bearing CIs were designed and installed on-board of the helicopter. In [40], the effectiveness of bearing energy and bearing shock pulse energy were tested and compared as bearing CIs. Spectral analysis was performed on bearing defect diagnosis using vibration data collected from a helicopter by Keller and Grabill in [53]. The issues with these researches are that, they were conducted on simple gear or bearing systems, whose mechanical faults were much easier to detect; and researches did not discuss the condition where gears and bearings are sharing same races, resulting in more complex vibration recordings. To investigate the diagnosis of helicopter planetary bearing faults, frequency domain based analysis should take place to deal with the complex structure. The frequency domain based analysis techniques are reviewed in the next section.

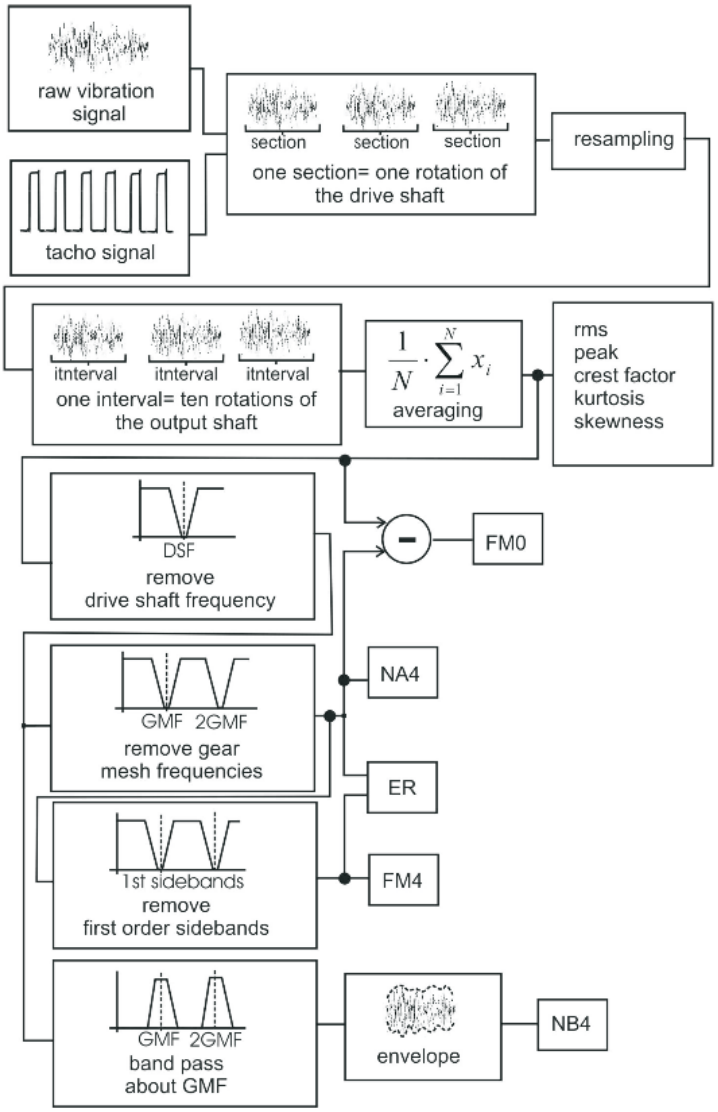

Figure 2.6: CIs generating process, [38]

2.4 Frequency Domain Based Signal Processing for Bearing Diagnosis

In Section 2.2 and 2.3, the basis of applying vibration analysis for condition monitoring, signal processing (production of CIs) and also the powerful utility of frequency analysis have been summarised. To fulfil the requirements stated in Section 1.2, and to fully utilise the potentials of frequency domain based signal processing, various signal processing techniques for bearing diagnosis are reviewed.

2.4.1 Bearing Fault Frequencies

The fundamentals of applying frequency domain analysis to diagnose incipient bearing fault are using FFT to extract the fault induced repetitive signals and present them in spectrum. The fault repetitive signals are caused by the contact between rollers and cracks while the bearing is spinning. There are four frequencies of particular interest, which are associated with four types of bearing fault. Using the Figure 2.7 below as a demonstration:

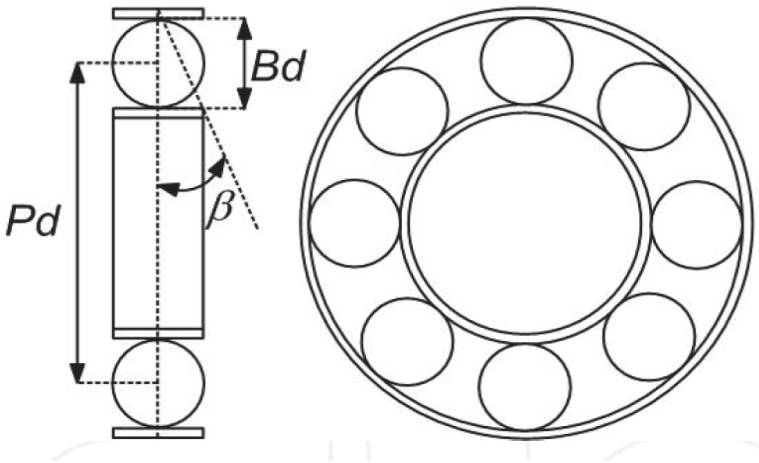

Figure 2.7: Demonstration of simple bearing [54]

where the parameters are representing:

Bd : Ball diameter
β : Contact angle of the ball on the race
Pd : Bearing Pitch diameter

The equations below are given for calculating the frequency components that are associated with four types of bearing faults, namely Fundamental Train Frequency (FTF), Ball-spin Frequency (BSF), Ball Pass Frequency of Outer Race (BPFO), Ball

Pass Frequency of Inner Race (BPFI) [54, 55]:

$$FTF = \frac{1}{2} f_r \left(1 - \frac{P_d}{B_d}\right) \tag{2.12}$$

$$BSF = \frac{1}{2}\frac{P_d}{B_d} f_r \left[1 - \left(\frac{B_d}{P_d}\cos\beta\right)^2\right] \tag{2.13}$$

$$BPFO = \frac{n}{2} f_r \left(1 - \frac{B_d}{P_d}\cos\beta\right) \tag{2.14}$$

$$BPFI = \frac{n}{2} f_r \left(1 + \frac{B_d}{P_d}\cos\beta\right) \tag{2.15}$$

where f_r represents the bearing rotating speed, and n is the number of rollers. Equation 2.14 is extensively applied in later Chapters where the planetary bearing outer race diagnosis is performed.

2.4.2 Cepstrum Editing

Although in [45], the author stated that the process of TSA and order tracking is vital, without which most of the separation job cannot be done, it is not usually guaranteed that the tachometer signal is available. In addition, the repetitive procedure for TSA is tedious in terms of separating bearing signals. Therefore, Cepstrum editing, which does not require order tracking is drawing more and more attention [56]. The first concept of Cepstrum was invented in 1960s initially for speech analysis [57]. It was described as "power spectrum of the logarithm of the power spectrum ". The calculation of complex Cepstrum is usually defined as [58]:

$$Cepstrum = F^{-1}[ln(X(f))], \tag{2.16}$$

where F^{-1} is the inverse fast Fourier transform ($IFFT$) operator, and $X(f)$ represents Fourier transform of time domain data $x(t)$. So that:

$$X(f) = F[x(t)] = A(f) \cdot e^{j\phi(f)} \tag{2.17}$$

$$ln[X(f)] = ln[A(f)] + j\phi(f) \tag{2.18}$$

This is the concept of complex Cepstrum. If the phase $\phi(f)$ is set to be zero, then C becomes the so-called "real Cepstrum". The frequently used terms *quefrency* and *lifter* are specifically developed in Cepstrum domain, corresponding to *frequency* and *filter* in frequency domain respectively, reflecting the inverse relationship of these two domains. R.B. Randall [56] did a thorough research on Cepstrum history and development.

Cepstrum analysis transforms signal in time domain firstly to frequency domain, then to "quefrency" domain. Editing components in quefrency domain, for instance, eliminating certain quefrency components, will suppress all corresponding frequency components including harmonics and sidebands in frequency domain. While phase $\phi(f)$ can be conveniently set to zero to generate the real Cepstrum, it cannot be inversed back to time domain directly after being edited due to the loss of phase information. In [56, 58–61], researches all concluded that for bearing fault diagnosis, it is usually unnecessary to use complex Cepstrum, since the editing on complex Cepstrum cannot be observed directly in time domain, and the edited complex signal phase may have distortions. Thus a modified real Cepstrum editing method is advocated, which reserves the phase information from FFT, and then combines phase information with edited real Cepstrum. Therefore, the edited real Cepstrum can be inversed back to time domain for post-analysis.

In Randall's research [58], the effect of Cepstrum editing being able to suppress unwanted sidebands was discussed. It is well demonstrated in Figure 2.8 that Cepstrum editing, unlike TSA, does not completely remove discrete gear mesh frequencies through repetitive averaging, but suppresses the interferences of periodic sidebands. In [62], the authors set the entire quefrency zone to 0 except for quefrency at the very beginning. They explained that the bearing damage related components, which are not strictly periodic, will not present any strong peaks in the absolute value of the Cepstrum and will not be affected by the liftering. In practice, this is equivalent to the operation of:

$$x_{edited}(t) = F^{-1}\{\frac{FFT(x)}{|FFT(x)|}\} \tag{2.19}$$

This method is very efficient computation-wise. An exponential window based Cepstrum

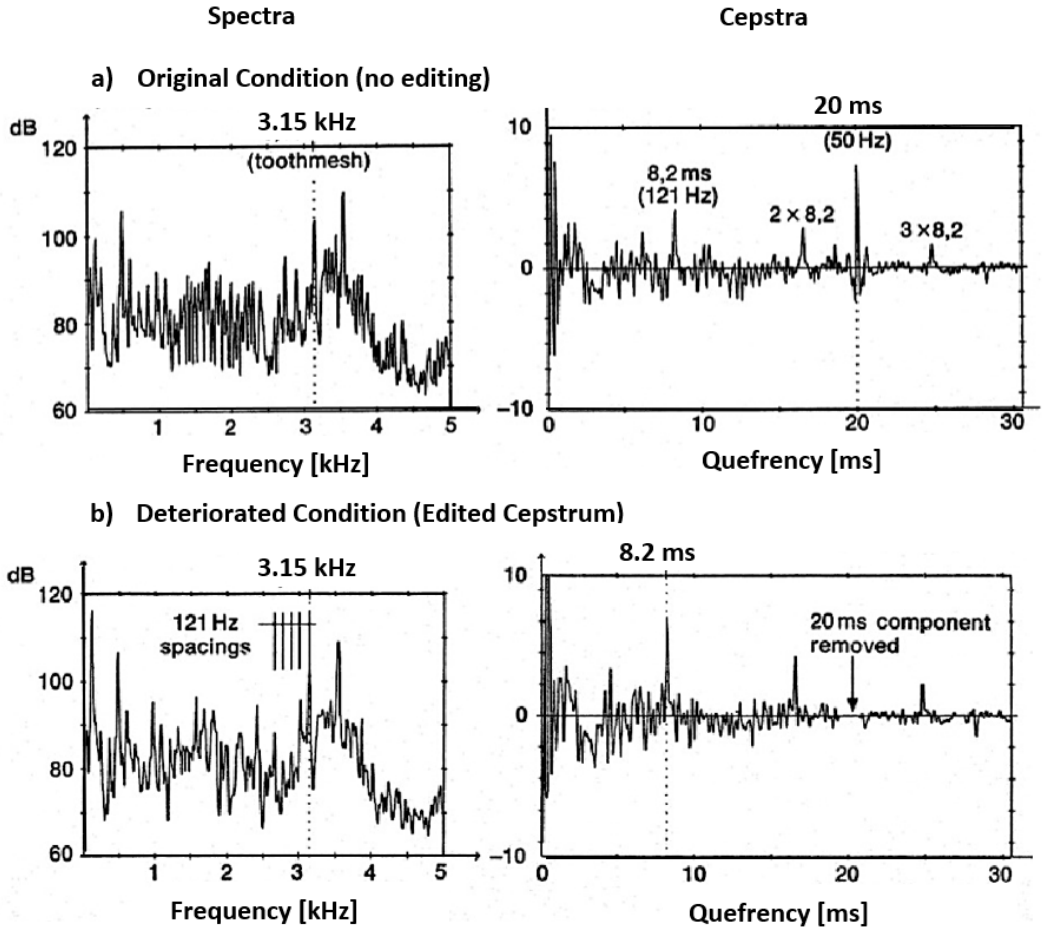

Figure 2.8: Demonstration of cepstrum editing [58]

editing method was proposed in [58], which essentially is liftering Cepstrum with an exponential window with the form of $e^{-\sigma \cdot t}$, where σ is a time constant. The idea is to smoothly suppress low frequency components and pass high frequency components and resonances which could be fault related.

2.4.3 Self-adaptive Noise Cancellation and Discrete Random Separation

It is generally recognised that the vibration signals acquired from a complex mechanical system, which contains shafts, gears, bearings and so on, are overall stationary. The frequency spectrum of such signal is usually a mixture of discrete frequency components excited by periodic gear meshes and shaft rotating, continuous frequency components related to mostly random noises, and nondeterministic bearing signals [18, 45, 63].

In [64], it is stated that the task of decomposing discrete and continuous spectrum is actually not easy to solve in practice. The most widely adopted ideas to separate these two types of signals are utilising their different statistical properties. Wold's theorem provides theoretical support for realising the separation idea [65]. The theorem states that for any stationary process $X(n)$, the representation exists:

$$X(n) = p(n) + r(n), \tag{2.20}$$

where $p(n)$ and $r(n)$ represent a deterministic process and a nondeterministic zero mean process respectively. In addition, $p(n)$ and $r(n)$ are not correlated. Deterministic signal $p(n)$ could be perfectly predicted from its past value, while nondeterministic signal $r(n)$ cannot. Wold's theorem basically guarantees that decomposing vibration signal into periodic and random signals is always possible, and the decomposition results of $p(n)$ and $r(n)$ are unique. It is also stated that the correlation time of a signal is positively proportional to its periodicity, e.g. a pure periodic signal has infinite correlation time which means it can be predicted theoretically from any arbitrary past values without prediction error. In contrast, nondeterministic signal cannot be perfectly predicted after a certain amount of time, when its current value lost correlation with its past values. Because of the natural slip existed in bearing while rolling, the correlation time of bearing defect related signal is theoretically shorter than that of a periodic gear mesh signals. Thus, they can be separated using adaptive filters that adaptively predict and filter periodic signals.

Adaptive noise cancellation (ANC) is a process that requires two inputs, namely a targeted signal and a reference signal (usually noise signal captured separately). ANC utilises adaptive algorithms, most prevalently Least Mean Square (LMS) and its varieties, to adaptively filter targeted signal until eventually the output and the reference signal has the least prediction error. If a noise signal is used as a reference, the final output of ANC should then be subtracted from targeted input signal to acquire noise-free results. However, in practice it is not always guaranteed that a reference noise signal is available. Information from a signal accelerometer is not sufficient to support the

application of ANC. In [66], Ho and Randall demonstrated the technique of using the targeted signal itself with a carefully selected delay as a reference signal, for bearing defect diagnosis. This technique is named Self-adaptive Noise Cancellation (SANC). The time delay in the reference signal is carefully selected, so that at that time point, the periodic signal has not lost its correlation with past values, but the bearing signals which has more random features due to rollers and slips are not correlated. Therefore, in the target signal, since only periodic part can be perfectly predicted, the output will resemble the deterministic part gradually, leaving the filtered error to be random signals consist of bearing and Gaussian noise. In [59, 64, 67–69] and many other articles, the concept of SANC has been discussed extensively. The schematic diagram of SANC is demonstrated in Figure 2.9.

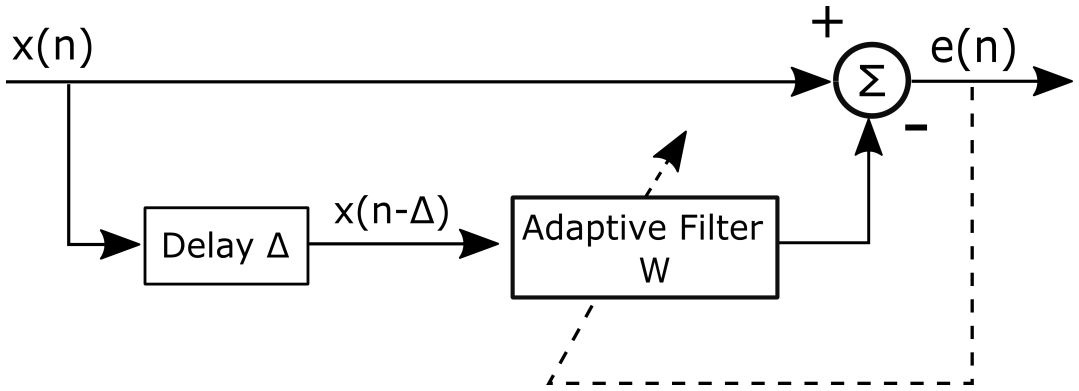

Figure 2.9: Schematic diagram of SANC [67]

The adaptive filter's coefficients are adaptively updated with the reference of output error $e(n)$. For the mostly adopted LMS method, the adaptive rule is defined as:

$$h_i^{n+1} = h_i^n + \mu \times e(n) \times x(n - \Delta - i) \tag{2.21}$$

$$e(n) = X(n) - \bar{X}(n), \tag{2.22}$$

where μ is the forgetting factor which determines the adaptation step, Δ is time delay. h_i with i from 1 to N represents the total filter coefficients with length N. $\bar{X}$ is the filtering output. In [64], a very thorough guidance was given on how to choose the factor Δ and N, while the recommendation on μ was directed to classic articles [70, 71].

Discrete-random separation (DRS) is a simplified algorithm compared with SANC.

SANC's processing results highly depend on the proper selection of μ, Δ and N introduced above, which need to be treated carefully in practice. In [72], J. Antoni and R.B. Randall introduced DRS as an adequate substitute for SANC, which provides much faster computation for the same or slightly compromised filtering results, with a trade-off of longer filter length. However, DRS does not require any adaptation process, while utilising FFT contributes to a significant reduction in processing time. With the same core idea of correlation difference, DRS constructs the filter with the help of frequency response function (FRF). This is achieved by blocking original data into several windowed segments to prevent frequency leakage, and then calculating FRF of each block with its corresponding delayed signal which should have exact same length. This result is averaged to produce a normalised indicator, with value ideally from 0 to 1, where 0 stands for random frequency components which are unstable due to the delay and averages, while 1 represents stable frequency components. A filter thus can be developed and applied back on time series signals. The process is defined as:

$$H(f) = \frac{E[G_b(f) \times G_a^*(f)]}{E[G_a(f) \times G_a^*(f)]}, \tag{2.23}$$

where $E[\cdot]$ is expectation operator. G_a and G_a^* are conjugate pairs of current windowed segment's FFT, and G_b is its delayed signal's FFT. This method has been extensively discussed in [18, 45]. Multiple articles have claimed successes on applying DRS for bearing and gear signal separation, the reported successes of applying SANC or DRS can be found in [67, 69, 73–75] and [76].

2.4.4 High Order Spectral Analysis and Bicoherence

The notion of frequency decomposition can be traced back to hundreds of years ago [77]. Fourier Transform analysis, especially the extensively applied FFT algorithm, has really simplified the process of detecting the existences of periodic defects that occur within rotating machineries.

Power spectrum is a powerful tool for estimating signal power distribution in frequency domain. However, as explained in [78–80] and [81], it is generally recognised that power

spectrum, as a second order statistics, cannot provide sufficient phase information such that a non-linear correlation among frequency harmonics cannot be detected. For instance, in a complicated frequency power spectrum, frequencies and harmonics that represent existences of potential defects can be easily masked by noises, gear meshes or sidebands induced by amplitude modulation. In these circumstances, Quadratic Phase Coupling (QPC), an indicator that describes non-linear phase interactions between two harmonic components can be helpful. QPC is a phenomenon that the sum of the phases at frequency $f1$ $(\phi 1)$ and frequency $f2$ $(\phi 2)$, is the phase at frequency $f1+f2$ $(i.e. \phi 1+\phi 2)$. As described in article written by Halim et al. [80], it can be an indicator of non-linearity in the vibration signal, and reflects the emergence of fault. High order spectra analysis, specifically bispectrum and bicoherence, is especially good at detecting QPC, compared with normal second order analysis, *i.e.* power spectrum analysis. The superiority of bicoherence in detecting QPC was demonstrated in [78].

The concept of high order spectral is explained as follows [78]. The r^{th} moment μ_r of a real-valued signal $x(t)$, is defined as:

$$\mu_r = E[x^r(t)], \tag{2.24}$$

where $E[\cdot]$ denotes the expectation operator. From the Equation (2.24), it is obvious that when $r=1$ and $r=2$, μ_1 and μ_2 simple are the mean (1^{st} order moment) and power or variance (2^{nd} order moment) of signal $x(t)$. Following the same pattern, μ_3 is known as *skewness* which is commonly used to measure data asymmetry (if the signal is pure Gaussian, μ_3 =0). And a more well-known normalised 4^{th} order moment μ_4/μ_2^2, is called *kurtosis*, which has been introduced in Section 2.3.2.

With these concepts introduced, the 2^{nd} order moment function R_2 (commonly referred to as autocorrelation function) and its relationship with power spectrum $S_2(f)$ can then be

defined as:

$$R_2 = E[x(t) \times x(t-\tau)] \tag{2.25}$$

$$S_2(f) = \lim_{T\to\infty} \frac{1}{T} E[X_T(f) X_T(f)^*], \tag{2.26}$$

where τ represents a time delay, X_T denotes the FFT of signal $x(t)$ over a time T. Therefore, R_2 and $S_2(f)$ can be connected via Fourier Transform. Similarly, the bispectrum as a decomposition of 3^{rd} order statistics R_3, is defined as:

$$S_3(f_1, f_2) = \lim_{T\to\infty} \frac{1}{T} E[X_T(f_1) X_T(f_2) X_T(f_1+f_2)^*] \tag{2.27}$$

Therefore, the bispectrum of signal $x(t)$ is really an evaluation of the relationship between two frequency components f_1 and f_2 that both exist within meaningful frequency range of $x(t)$. In practice, it is the normalised version of bispectrum that is adopted generally, which is named bicoherence. This is because bispectrum estimation is not completely variance independent from power spectral properties of a signal [78]. The normalisation of bispectrum produces bicoherence, which is a set of values ranging from 0 to 1, with 1 representing the existence of very strong QPC. The simplified definition of bicoherence is given [80]:

$$bic^2 = \frac{|E[X(f_1)X(f_2)X(f_1+f_2)^*]|^2}{E[|X(f_1)X(f_2)|^2]E[|X(f_1+f_2)|^2]} \tag{2.28}$$

Similar to the periodicity property of FFT, bicoherence and bispectrum also have a symmetric property in the entire $[f_1, f_2]$ frequency plane. The researches of [82–84] have shown that it is sufficient to only calculate bicoherence in the first quadrant where both f_1 and f_2 are positive, and satisfy the conditions that: $f_1 > f_2 > 0, f_1 + f_2 < \frac{f_s}{2}$. This range defines a non-redundant area for bicoherence, which is named "the principle domain". Bicoherence has been reported to be applied in machine fault diagnosis in [85–87].

2.4.5 Envelope Analysis

Envelope analysis has been established as a benchmark technique for bearing fault diagnosis. It excels at revealing repetitive information hidden in signals' envelope, mitigating the effect of speed fluctuation, amplitude modulation, and additive noise [18, 45]. Weak repetitive signals generated by bearing rolling are modulated and amplified by the structural resonance from the bearing cages, while the gear signals are not highly affected by such effect [3]. Therefore, envelope analysis benefits considerably from band-passing vibration signal in a certain high frequency band, where the frequency resonances associated with planetary bearings are dominant [88]. The envelope of band-passed high resonance signal is then obtained by performing Hilbert transform (HT). By examining the envelope spectrum of the band-passed signal, the diagnostic information of faulty bearing signals can be extracted for defect identification. It is because of the use of spectrum analysis, envelope analysis is also commonly referred as envelope spectrum analysis. The effect of envelope analysis conquering speed fluctuations and modulations are described in [18]. In Figure 2.10, it was demonstrated that even with speed fluctuations, envelope spectrum can still reveal repetitive spikes signatures in frequency domain. It can bee seen that with added random noises, the time domain signal retains the similar waveforms, while showing severe changes in spectrum. The envelope analysis performed in Figure 2.10 mitigated the interferences, and preserves the frequency components in envelope spectrum.

Most prevailing method nowadays to obtain envelope of bandpass signal is Hilbert Transform (HT), which is a four-step executional-wise process [89]:

1. Conduct n-points FFT on time series $x(n)$, acquiring $X(f)$
2. Create a vector H of n points , whose elements are 1 for $n = 1$, $\frac{n}{2} + 1$, 2 for $n = 2 \cdots \frac{n}{2}$ and 0 for the rest of H
3. Calculate $X(f) \times H$
4. Inverse FFT of the sequence calculated in step 3 and returns the first n elements

The result of HT gives out an analytic signal, i.e. complex signal has no negative frequencies. The absolute values of HT signals form the envelope of original signal.

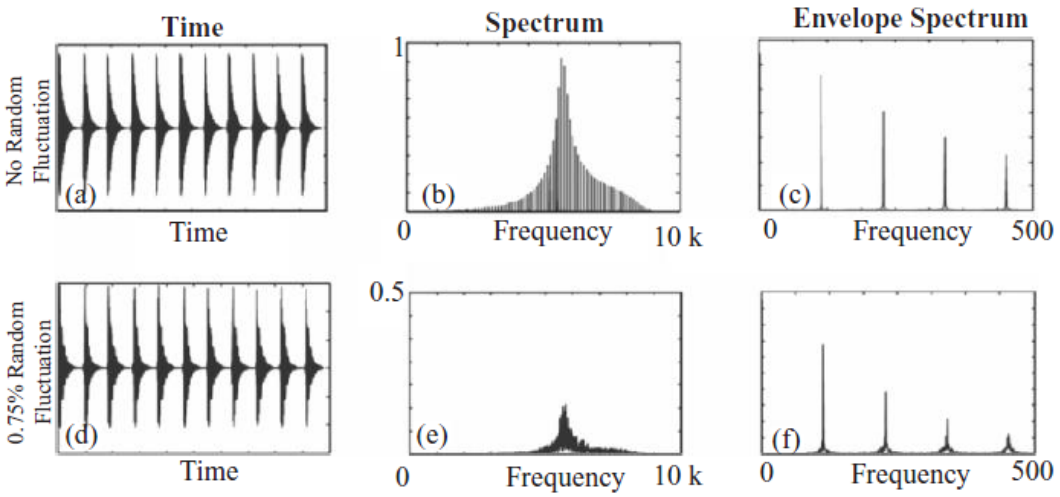

Figure 2.10: Benefits of envelope spectrum [18]

In [90] the process of envelope analysis involving bandpass and HT was discussed, reinforcing the feasibilities of using envelope analysis on the diagnosis of complex gearbox systems.

2.4.6 Spectral Kurtosis and Kurtogram

As described before, the essence of envelope analysis is selecting an optimal demodulating centre frequency and bandwidth. In practice, this was used to be a mechanical problem, rather than a mathematical decision. In [88], a process of determining resonances frequencies was demonstrated. In Figure 2.11, it was shown that the resonance was selected in the range of [11000 Hz, 13000 Hz], so that the centre was 12000 Hz.

In [45], it is stated that there was a recommendation on using a hammer tap testing to find out bearing housing resonances before the actual bearing tests, which was inconvenient. This problem now can be solved mathematically with the help of a statistical tool called Spectral Kurtosis (SK). Kurtosis, which has been introduced in section 2.3.2, is not effective as a local defect indicator, simply because when dealing with signals that have complicated frequency information, the value of Kurtosis is not responsive to small impulses excited by a local bearing defect. However, the Kurtosis value of signal buried in certain frequency band can make a difference. The technique of

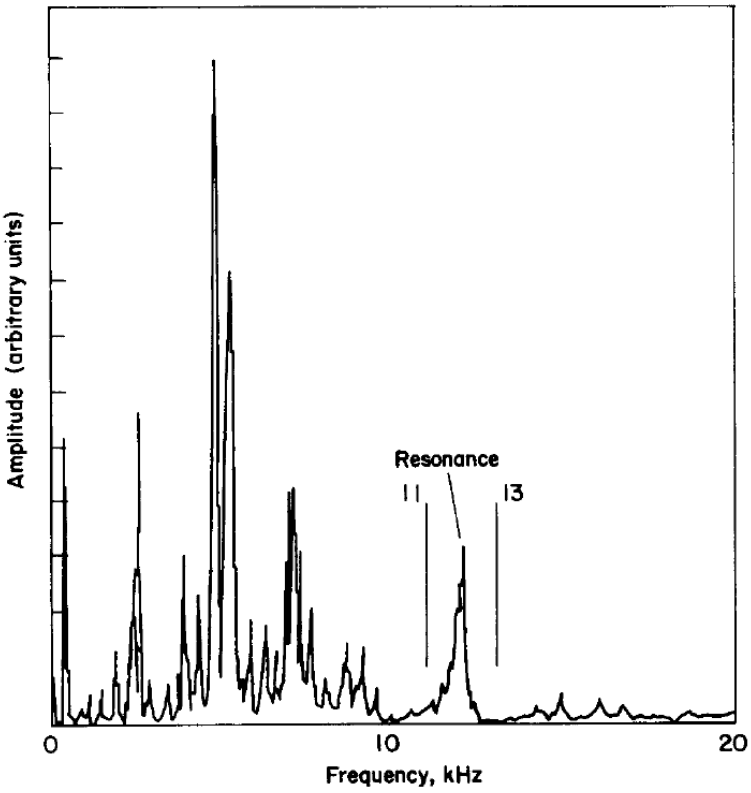

Figure 2.11: Vibration spectrum from bearing life test in literature [88]

extracting Kurtosis value in different frequency band is SK. SK was first devised by Dwyer in [91] for detection of "randomly occurring signals " [92]. The initial definitions were vague and cumbersome. J. Antoni gave a detailed study of SK in [93, 94], which not only provided a more simplified and clarified definition of SK, but also demonstrated the potential applications of SK on bearing defect diagnosis. In [45], the concept of SK was recapitulated, and developed into a more decision-making friendly tool called Kurtogram. SK and Kurtogram are discussed consecutively below.

Firstly, SK of a time-domain signal $x(t)$ is produced from Short-time Fourier Transform (STFT), $X(t,f)$, which is a local Fourier transform at time t with a sliding window moving across the entire signal record. Therefore, the spectral kurtosis is defined as [45]:

$$K(f) = \frac{E\{|X(t,f)|^4\}}{E\{|X(t,f)^2|\}^2} - 2, \tag{2.29}$$

where $E[\cdot]$ is the expectation operator, therefore $E\{|X(t,f)|^2\}$ is considered as the power

spectral density (PSD) of the signal at time t. It is very interesting that Antoni also gave out a physical interpretation of $K(f)$. When $X(t,f)$ is seen as a function of t, $X(t,f)$ is actually the complex envelope of signal $x(t)$ bandpass filtered around frequency f. Therefore, $K(f)$ can be interpreted as the kurtosis of averaged complex envelope of signal $x(t)$ at time t, with a short-time window corresponding to certain narrowband filtering activity around frequency f_{centre}. Noted that f_{centre} is not reflected in the definition equation of SK. The physical interpretation is demonstrated in Figure 2.12.

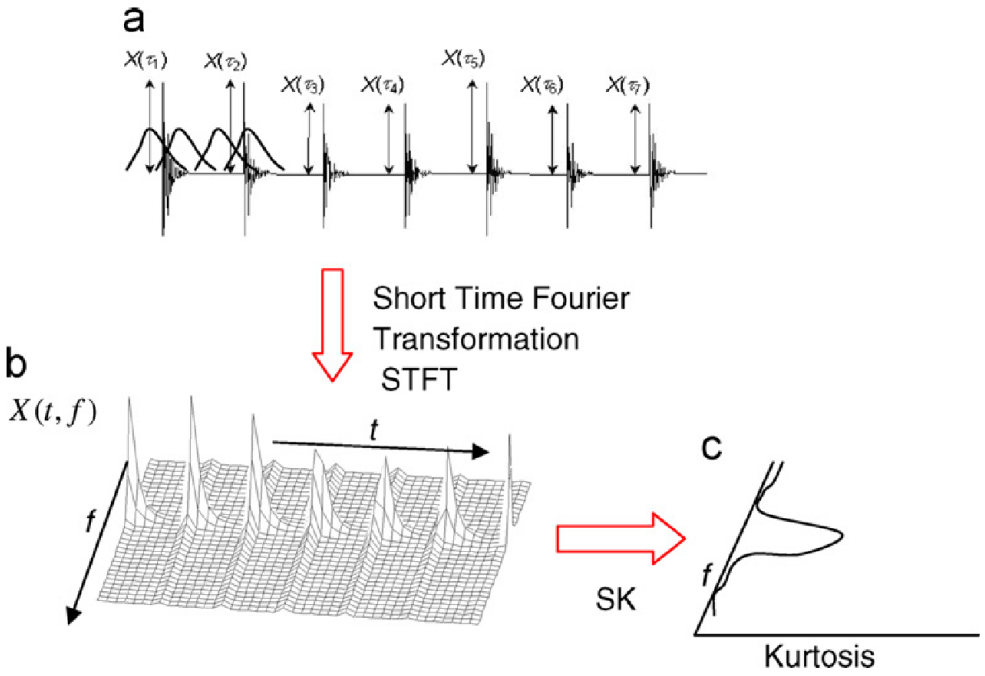

Figure 2.12: Calculation of SK from STFT [45]

In Figure 2.12 (a), a time signal with series of short-time impulses is windowed and transformed into time-frequency domain using STFT. In time-frequency domain, the frequency components $X(t,f)$ are further averaged along time t, and then kurtosis values of averaged $X(t,f)$ are calculated to get SK in Figure 2.12 (c).

As stated above, f_{centre} is not reflected in SK definition Equation (2.29). Therefore, the whole process of determining the frequency band which contains most impulsive signatures is still tedious. J. Antoni thus proposed a way to calculate SK not only as function of t and f, but also as function of frequency bin Δf. So that the value of SK in different centre frequency and bandpass bandwidth can be reflected in a colour map.

Since Kurtogram is able to provide suggestions on possible bandpass centre frequency as well as bandwidth, application of envelope analysis is much more simplified. However, it is noticed that the indication of Kurtogram is not absolutely correct, especially in our cases where multiple gear mesh frequencies and harmonics exist. Thus the final parameters of f_{centre} and Δf for envelope analysis demodulation sometime needs to be chosen wisely and tested with data. Regardless, the application of Kurtogram, especially fast computation algorithm of Kurtogram developed by the same researcher [95], is very useful and always worth trying. Applications of Kurtogram on bearing fault detection using vibration signals have been reported in [96, 97].

2.4.7 Iterative Envelope Cancellation

The effectiveness of envelope analysis is heavily dependent on the selection of the optimal structural resonances, as discussed in previous section. If the optimal demodulation band is unable to be discovered, it could be tedious to manually select and test every possible resonance in frequency domain.

One solution for this issue is to use a very efficient and fast-calculative algorithm, namely the Iterative Envelope Cancellation (IEC). This algorithm was proposed recently by Ming et al. [98], which utilised iterative envelope calculations to suppress gear mesh signals in frequency domain. Their research specifically studied the effect of Hilbert transform on discrete gear mesh signals and random bearing signals. Mathematical deduction was elaborated in their study, concluding that through iteratively calculating signal squared envelope using Hilbert transform and subtracting DC components, the discrete frequency components suffer larger attenuation in amplitude, compared with that of bearing-related components. The reasons are that bearing-related signals can be modelled as a train of high frequency transient impulses, while gear meshes are periodic cumulations. Square envelope of the signal potentially introduces cross-terms between these two types of signals, weakening the pattern of periodic cumulations. The schematic diagram of iterative envelope cancellation is demonstrated in Figure 2.13.

In Figure 2.13, the stop point of the iteration is determined by control factor η, which is defined as [98]:

$$\eta = \frac{|2 \times \langle Env^{k-1}, Env^{k} \rangle|}{\langle Env^{k-1}, Env^{k-1} \rangle + \langle Env^{k}, Env^{k} \rangle}, \tag{2.30}$$

where k represents current iteration index, $\langle \cdot \rangle$ represents inner product operator. η described the extent of difference between current k iteration calculated signal envelope with $k-1$ iteration envelope. For instance, $\eta = 1$ means the two envelopes are exactly the same, hence more iterations of calculation are redundant. Based on processing experiences, stop factor η_0 should be wisely chosen between 0.8 up to 0.95 for distinct gear mesh suppression and subsequent envelope spectrum analysis.

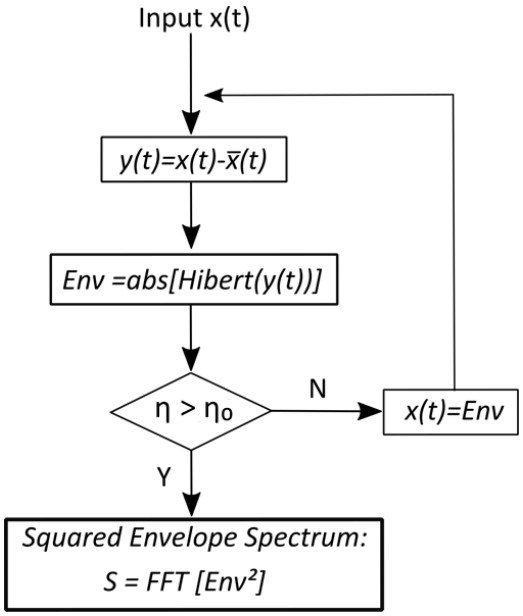

Figure 2.13: Schematic diagram of iterative envelope cancellation

Iterative envelope cancellation solves the problem of traditional envelope analysis by evading the selection of optimal frequency band. Instead, the application of sub-optimal frequency band is remedied by iterative calculations and high-pass the input signal at a relatively high frequency where resonance spikes are more concentrated, which only requires rough knowledge from observing frequency spectrum of input signal. There has been reported success in using this method for planetary bearing fault diagnosis [99].

2.5 Summary

In this Chapter, firstly the fundamentals of vibration-based CM and vibration frequency analysis are investigated, followed by the introduction of VHM employed in HUMS, where the commonly used CIs are also discussed. Next, the frequency domain processing techniques that are relevant to the aims identified in Section 1.2 have been reviewed. Some of the techniques may not be originally developed for vibration data processing, such as Cepstrum analysis. However, these techniques have been applied in studies and proven to be effective in certain use cases. The introduced signal processing techniques are summarised in Table 2.2, in terms of their category, effectiveness (High, Medium and Low), Computation (Fast, Medium and Slow) and their dependencies to work. The most prominent analysis techniques, however, are Cepstrum editing, SANC, Discrete Random Separation (DRS), Envelope analysis, Kurtogram and IEC.

In conclusion, although VHM has seen widely application in HUMS, its processing is still focusing on gears, and the techniques employed are mostly time domain based statistics (such as RMS, energy, kurtosis) which can result in inaccurate and misleading outcome. Frequency analysis as demonstrated in Figure 2.2(b), is a competent candidate for more detailed signal analysis that can achieve de-noising, gear/bearing signal separation and extract the most relevant frequency band for envelope analysis. For the reviewed signal processing techniques, although successes are found in bearing diagnosis, not many of them have been applied in diagnosis for planetary bearing in MGB, which is a challenging task. To further validate these frequency analysis techniques, experiments should be undertaken on real helicopter MGB with seeded planetary bearing outer race defects. The experiments are described thoroughly in Chapter 3.

Table 2.2: Summary of reviewed signal processing techniques

Processing technique	**Effectiveness**	**Computation**	**Dependencies**	**References**
TSA Order Tracking	High	Medium	Tachometer; Interpolation	[42–51]
Cepstrum Editing	Medium	Fast	Knowledge of system	[45, 56–60, 62]
SANC	High	Slow	Parameters selection	[59, 64, 66–71]
DRS	Medium	Fast	TSA/ Order tracking; Induced error	[18, 45, 72] [67, 69, 73–76]
Bicoherence	Slow	Low	Stationary signal	[77–87]
Envelope Analysis	Highly	Fast	Locate resonances	[18, 88–90, 107]
SK	Medium	Medium	Susceptible to noise	[45, 91–97]
IEC	Medium	Fast	Parameters selection	[98, 99]

Chapter 3

Seeded Defect Tests Performed on Planetary Bearings in SA330 Helicopter MGB

3.1 Introduction

In Chapter 2, it is summarised that validating the reviewed frequency domain signal processing techniques on MGB planetary bearing fault diagnosis is required. To fulfil this requirement, it is essential to gather valuable experimental data from operational helicopter MGB. For this reason, a *Category A* Super Puma SA330 helicopter MGB was adopted. *Category A* with respect to helicopters means a multi-engine helicopter designed with engine and system isolation features, and is capable of maintaining adequate performance for continued safe flight or safe rejected take-off in the event of engine failure [108]. A test rig that was capable of driving this MGB was designed and assembled by a Cranfield University team, lead by Prof. David Mba. The rig consists of a high speed direct current (DC) drive motor to provide adequate initial drive speed; speed-increasing gearboxes for multi-stage speed acceleration and drive MGB; an absorption dynamometer adopted as adjustable load on top of the 2^{nd} epicyclic output shafts; and a lubrication system to circulate lubricant in MGB during tests.

In the following sections, the setup of the test rig will be described first. The rest sections present information of performing the seeded tests, including data acquisition, sensory information and test procedures.

3.2 The MGB Test Rig Setup

3.2.1 Introduction of the SA330 MGB

In Chapter 1.1, Figure 1.1 demonstrates the common structure of two-stage epicycle modules in MGB. In this study, the adopted SA330 MGB has the similar structure. The external appearance of SA330 MGB is shown in Figure 3.1.

Figure 3.1: SA330 MGB without loading

The details of gearbox are listed in Table 3.1.

Table 3.1: Gearbox details of SA330 MGB adopted

Description	Values
Model Description	330 ARG
Assembly Number	32 600000
Serial Number	ACF 35 36
Manufacturing Date	03/02
Input Drive Speed	22841 rpm
Output Drive Speed	265 rpm
Maximum Continuous Power	1300 kW
Temperature Limit	340 °C

The internal structure of MGB is presented in the Figure 3.2. It patently demonstrates the complete speed reduction process, which starts from the high engine speed and ends at the aft reduction gear system. Notably, the output 265 rpm to the main rotor system, which is coupled with the 2^{nd} epicyclic carrier plate, is derived from the Forward reduction, bevel gear reduction and finally the two-stage epicyclic reduction systems. The relationships between reduction gears and the fundamentals of planetary speed reduction system are elaborated in the following paragraphs.

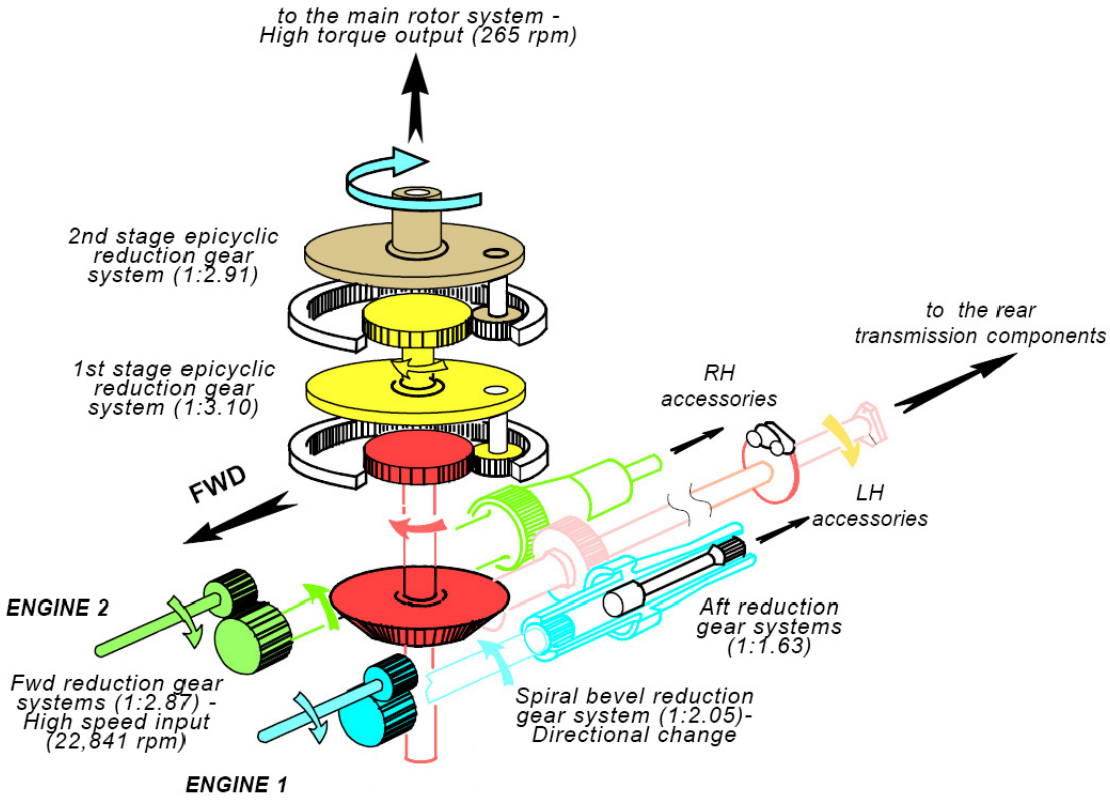

Figure 3.2: SA330 MGB internal structure [109]

Before introducing the complex planetary speed reduction system, firstly a simple two-gear speed reduction system is discussed. As shown in Figure 3.3, two gears are meshing together, where G_1 on the left is labelled as the drive gear and has a total teeth number of $N_1 = 20$. G_2 is the gear driven by G_1 that has a teeth number of $N_2 = 30$. Since the two gears are coupled together, the number of teeth that are meshed in a certain period should be the same for both of the gears. Considering the angular velocity of G_1, G_2 is ω_1 and ω_2 respectively, the below relationship is true:

$$N_1 \times \omega_1 = -N_2 \times \omega_2 \tag{3.1}$$

$$\omega_2 = -\frac{N_1 \times \omega_1}{N_2} \tag{3.2}$$

Therefore, based on the Equation 3.2, it is conclusive that given N_2 is larger than N_1, the angular speed ω_2 will be a smaller value than ω_1. In this case, ω_2 will be $2/3$ of ω_1, calculated with the given N_1, $N2$ value. The minus symbol is indicating that G_1, G_2 are spinning in different directions.

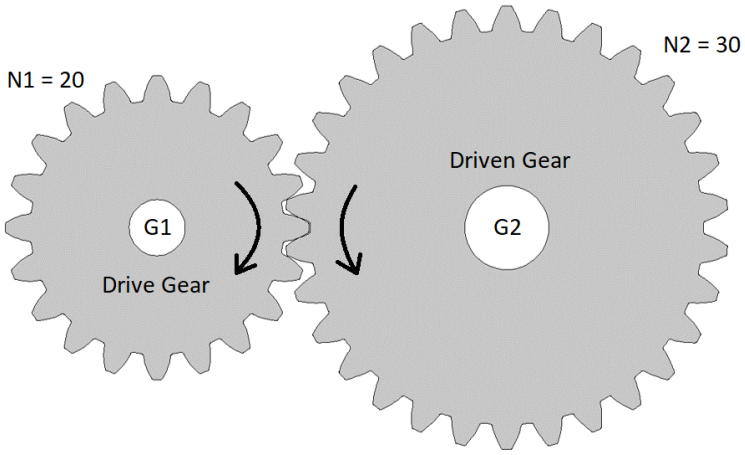

Figure 3.3: A simple two-gear reduction system

With the fundamental of gear speed reduction explained, the planetary speed reduction system will be discussed here. A demonstration of planetary speed reduction system is illustrated in Figure 3.4. Most commonly, a planetary speed reduction system consists of a ring gear, planetary gears, a sun gear and a carrier gear. The system works in a way resembles the planetary system, that the planetary gears orbit around the sun gear in the centre, with the ring gear acts as a boundary. The carrier gear is usually connected to planetary gears, providing a reduced speed output when the sun gear is the driving gear. There are numerous ways of operating this system, such as fixed ring gear, fixed carrier gears and fixed sun gear. In our study, the epicyclic module internal casing is considered to be a fixed ring gear, therefore only the speed ratio of this mode is relevant. However, in order to calculate the speed ratio, it is often convenient to assume the condition where

the carrier gear is fixed and planetary gears are idle for simplifying the deduction of speed ratio equations.

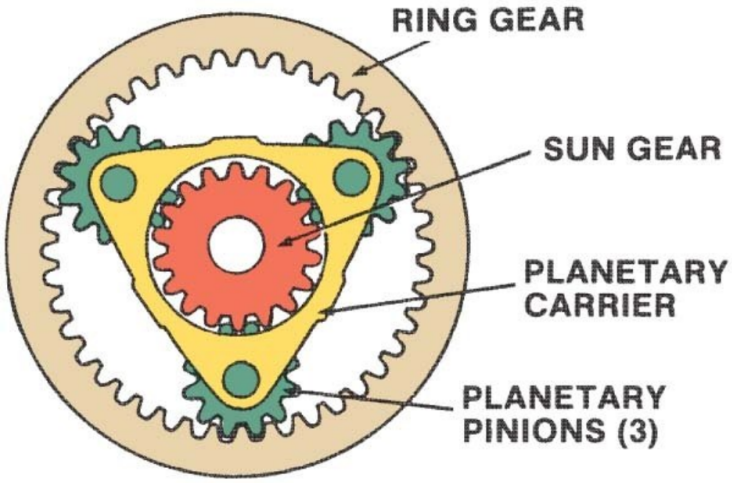

Figure 3.4: Demonstration of planetary gear train [110]

The deduction of equations to calculate the speed ratio in a planetary reduction system is explained here [111]. When the carrier is fixed and planetary gear is idle, the speed ratio is only relevant between the sun gear and ring gear. Using N_s, N_r to denote the number of sun gear teeth and the number of ring gear teeth respectively, and ω_s, ω_r as corresponding angular speed, combining the Equation 3.1, the speed ratio R is:

$$\begin{aligned} R &= \frac{\omega_s}{\omega_r} = -\frac{N_r}{N_s} \\ &= \frac{\omega_s - \omega_c}{\omega_r - \omega_c} \end{aligned} \tag{3.3}$$

Equation 3.3 is true if considering the angular velocity as a relative speed to the carrier speed ω_c. Equation 3.3 is also fundamental for estimating the condition, where in our case, speed of ring gear $\omega_r = 0$, thus:

$$\frac{\omega_s - \omega_c}{-\omega_c} = -\frac{N_r}{N_s}, \text{ so that } \frac{\omega_s}{\omega_c} = 1 + \frac{N_r}{N_s} \tag{3.4}$$

Equation 3.4 is used in the rest of the thesis for calculating the speed reduction ratio in SA330 MGB. Given the pinion (drive gear), wheel (driven gear) pairs information from drive shafts and planetary gears teeth information, the speed ratios from all MGB parts in Figure 3.2 are listed in Table 3.2.

Table 3.2: MGB speed reduction ratios

Parts name	Pinion teeth	Wheel teeth	Speed ratio
First parallel shaft from engines	23	66	2.87:1
Second parallel shaft to bevel stage	35	57	1.63:1
Bevel stage to 1^{st} epicyclic module	22	45	2.05:1

Module name	Sun gear	Ring gear	Planet gear	Speed ratio
1^{st} Epicyclic	62	130	34	3.10:1
2^{nd} Epicyclic	68	130	31	2.91:1

The overall speed reduction rate is easily calculated from combining the individual reduction rate shown in Table 3.2. By simply multiply the rate, the speed reduction from engines to main rotors is calculated to be $R_{overall} = 86.51 : 1$. That is to say, if the input speed generated from the engine is 22841 rpm, then the output speed provided to the main rotor will be reduced to approximately 265 rpm. This result is agreed with the information shown in Figure 3.2. To illustrate the ratios, the schematic diagram of the test rig is shown in Figure 3.5, which showcases how the components are connected in a systematic view.

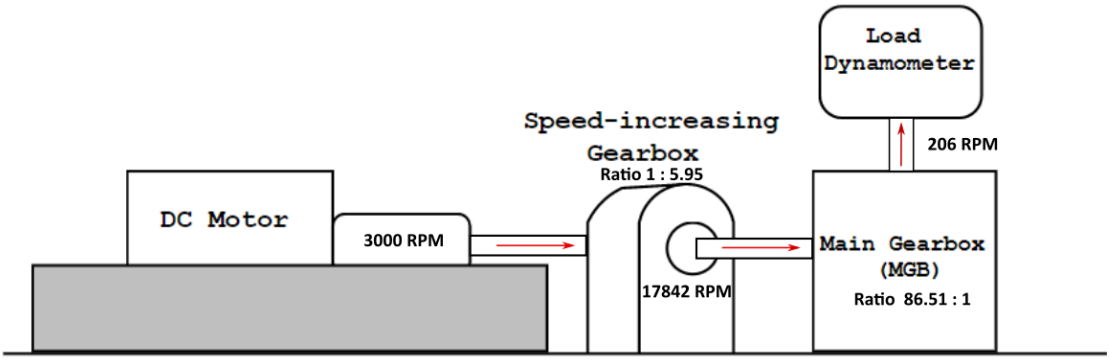

Figure 3.5: Schematic diagram of the test rig

3.2.2 Inside the Epicyclic Module

Figure 3.6 demonstrates the whereabout of 1^{st} and 2^{nd} epicyclic modules. Specifications of planetary bearings for both modules are documented in Table 3.3. Figure 3.7(a) demonstrates 2^{nd} epicyclic planetary bearings, which are driven by 2^{nd} epicyclic sun gear and ring gear shown in Figure 3.7(b). Bearing outer race defects were seeded on one of the planetary bearings in Figure 3.7(a).

Figure 3.6: Demonstration of MGB epicyclic modules [109]

Table 3.3: Number of planetary bearings and their corresponding rollers

	Planetary bearings	**Number of rollers**
1^{st} Epicyclic module	8	17
2^{nd} Epicyclic module	9	13

3.2.3 Other System Components

Helicopter MGB employed in this study comprises a forward module that connects the DC drive motor, a bevel stage reduction module, two aft modules to drive accessory systems and a two-stage epicyclic module. Planetary carrier at 2^{nd} epicyclic module is responsible for driving the dynamometer. The internal configuration of MGB system is demonstrated

(a) 2^{nd} Planetary gears/ bearings (b) 2^{nd} Epicyclic module ring and sun gears

Figure 3.7: MGB 2^{nd} epicyclic module

in Figure 3.2. Working principle of MGB is described here: high input speed is generated from engines (DC motors in this study) to forward module. Input speed is reduced at parallel shafts and intermediate shaft, and the rotational direction of the speed is altered to vertical by spiral bevel gear. Rotation speed is further reduced through 1^{st} and 2^{nd} epicyclic modules, which contain of 8 and 9 planetary gears respectively. Main rotor output speed is synchronised with 2^{nd} epicyclic carrier plate. Aft module output is used to drive other accessory systems and tail rotors.

Figure 3.8 demonstrates the test rig in assembled and read-to-go state. The test rig consists of a SA330 MGB, a speed-increasing gearbox, a DC motor and a dynamometer. The DC motor is able to generate 3000 rpm speed. The speed-increasing gearbox connected with DC motor can significantly boost the speed up to 17842 rpm to drive one of the MGB's input shaft. The absorption dynamometer was installed on top of the 2^{nd} epicyclic module, creating desired loading for MGB.

In this study, as the emphasis was on monitoring epicyclic stages of the MGB, two aft module outputs were left idle. The rig was adjusted to allow only one high speed input to be effective as shown in Figure 3.9, which limited the input power of the rig to 350 kW. This value was further scaled-down to approximately 293 kW, by the output speed limitation of the speed-increasing gearbox.

As the information for MGB has been stated in Table 3.1, the rating of the other components including the DC electric motor, the speed-increasing gearbox, and the

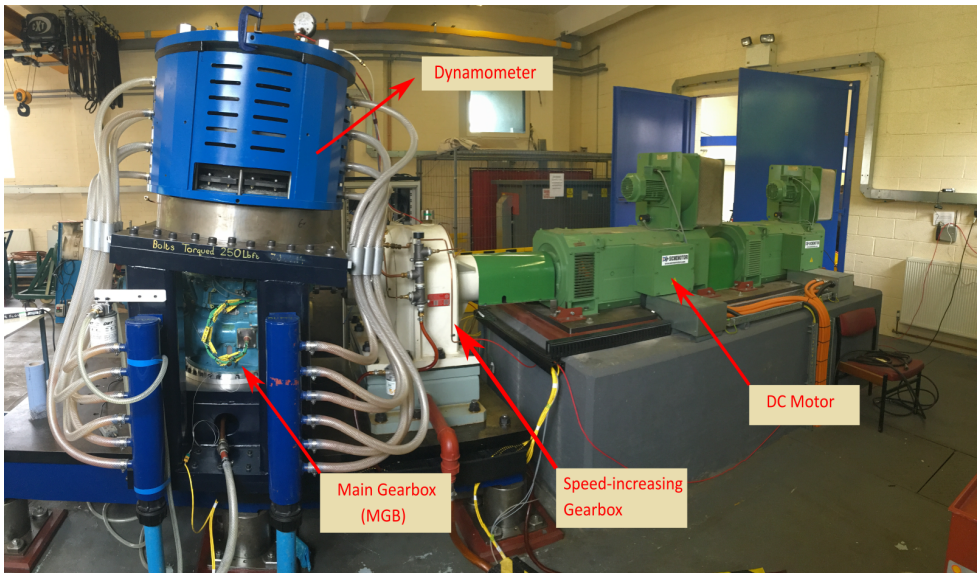

Figure 3.8: Demonstration of MGB test rig

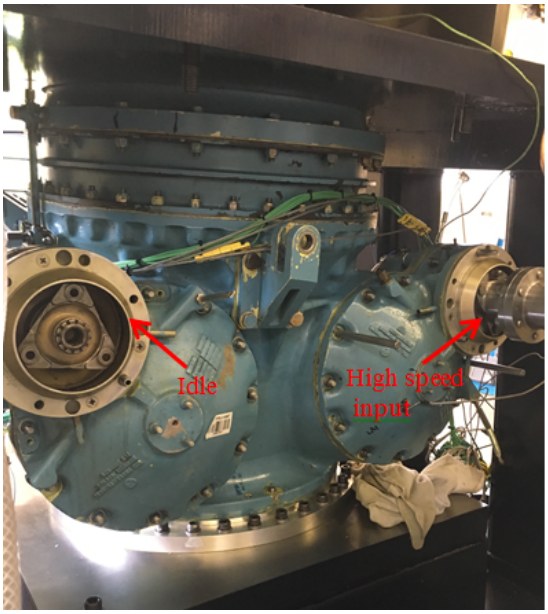

Figure 3.9: Demonstration of single input shaft

dynamometer will be given in the following paragraphs.

DC Electric Motor

The driving speed and force for the MGB is produced by DC electric motor, namely the Sicmemotori (P/N: NP225 KS5 PVA/B3) shown in Figure 3.10. The motor is a tandem drive DC motor, which has a combined maximum speed of 3000 rpm. The operating specifications of the motor are summarised in Table 3.4

Figure 3.10: Schematic diagram of the test rig

Table 3.4: Specifications of DC electric motor [109]

Description	Value
Maximum Output Power	750 (kW) at Tandem Drive
Maximum Rotational Speed	3000 rpm
Max Continuous Torque	1193 Nm at max speed
Type of Cooling	Forced Ventilation

Speed Increasing Gearbox

The speed-increasing gearbox from Compact Orbital Gears Limited (P/N: F5030) was employed to accelerate the speed from DC motor before coupling and driving the MGB. Figure 3.11 shows the ratings of the speed-increase gearbox. The operating specifications are summarised in Table 3.5

Table 3.5: Specifications of speed-increase gearbox [109]

Description	Value
Speed ratio	5.947:1
Maximum Input Rotational Speed	3000 rpm
Maximum Output Rotational Speed	17842 rpm

Dynamometer

Lastly, to simulate the loading of MGB, the dynamometer, a Wichita AquaMakks clutch

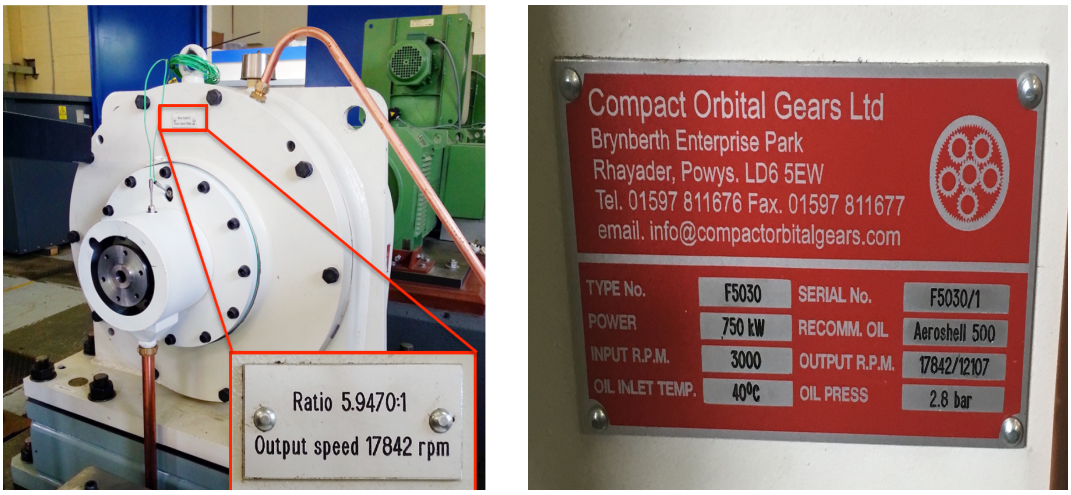

(a) Speed increasing gearbox front-view [109] (b) Ratings of the gearbox

Figure 3.11: Speed increasing gearbox

and brake system (P/N: 7-325AM-B-1300) was selected. It was installed on top of the MGB 2^{nd} epicyclic carrier plate. Figure 3.12 illustrated the installation of dynamometer. The dynamometer is capable of absorbing the power generated by the MGB operated at 17842 rpm input speed [109].

Figure 3.12: Dynamometer installed on top of MGB

The transmission train diagram of the MGB is depicted in Figure 3.13, where the number of gear teeth for each module is indicated. The gear ratio information and transmission paths are used to for determining the sensitive sensor axis, and the calculation of the significant frequency components.

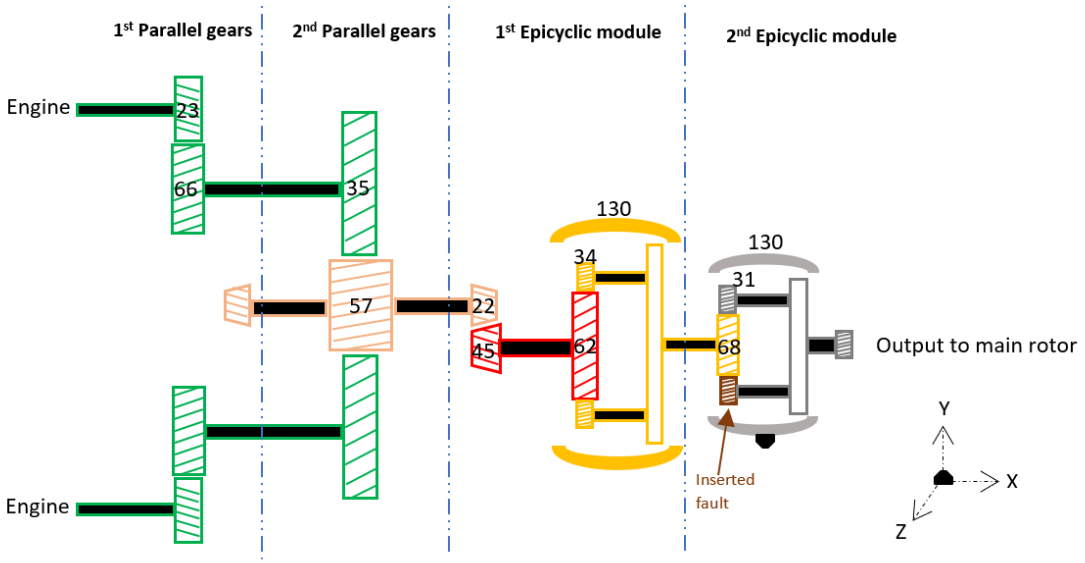

Figure 3.13: MGB transmission schematic diagram

3.3 Description of Seeded Bearing Defect Tests

3.3.1 Planetary Bearing Components and Seeded Bearing Outer Race Defects

After the components and assembly of the test rig are introduced in Section 3.2, creating and seeding planetary bearing outer race defects will be discussed in this section. To insert incipient defects on outer race of 2^{nd} epicyclic planetary bearing, a 2^{nd} epicyclic planetary bearing was disassembled as shown in Figure 3.14. The dissembled bearing has two layers of inner race and outer race, two sets of rollers and cages. There are 13 rollers for 2^{nd} planetary bearings, and 17 rollers for 1^{st} planetary bearings. The geometry details of 2^{nd} planetary bearings are listed in Table 3.6.

Based on the information presented in Table 3.6, the outer race fault related frequency component, namely the BPFO, which is caused by bearing roller periodically hitting the

Table 3.6: Geometry details of 2^{nd} planetary bearings

Description	Values
Number of rollers	13
Pitch diameter [P_d]	63.65 [mm]
Roller diameter [B_d]	12.5 [mm]
Contact angle [β]	$\approx 0^{\circ}$

cracks while spinning, can be calculated using the Equation 2.14. With the speed of bearing spinning f_r adopted as a variable, the calculation is given in Equation 3.6, which will be extensively applied in Chapter 4 when discussing the diagnosis of seeded faults.

$$BPFO = \frac{n}{2} f_r \left(1 - \frac{B_d}{P_d} \cos\beta\right) \tag{3.5}$$

$$= 5.2235 \times f_r \tag{3.6}$$

To insert defects of various sizes, EASA suggested that considering the double-race

Figure 3.14: The components of 2^{nd} planetary bearing

bearing design, it was essential to have the minor defect covers no larger than half of the selected outer race layer length, while major defect should cover the full race length. This recommendation has made this study distinctly different from the research reported

in [3], where the minor fault and major fault had 10 mm and 30 mm width respectively, with the length covered one layer of the race. Therefore, the diagnosis of the seeded incipient defects in this work is more challenging. With this consideration in mind, the outer race cracks were created using mechanical tools. Dimensions of minor and major defects are recorded in Table 3.7. Pictures of minor and major defects are demonstrated in Figure 3.15. Faulty bearings were located at 2^{nd} epicyclic module, which has been shown in Figure 3.6, between 1^{st} and 2^{nd} carrier plates.

Table 3.7: Dimensions of seeded bearing defects

Coonditions	**Length [mm]**	**Width [mm]**	**Depth [mm]**
Minor Defect	5	3	1.5
Major Defect	8	6	2.5

(a) Minor Defect

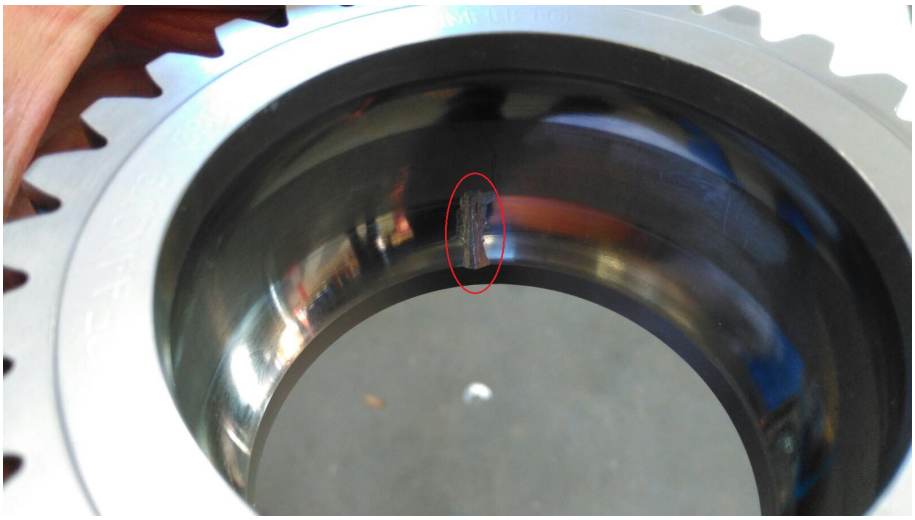

(b) Major Defect

Figure 3.15: Demonstration of seeded defects

3.3.2 Data Acquisition System Setup

In this section, the setup of the data acquisition system for the experiments will be discussed, including the sensors' installation, the adopted sensors, and the adopted data cards.

The rules of selecting sensors are platform and mission specific according to [30]. Generally, requirements of sensor installation are that: firstly, sensors should be installed as close as practical to the components they are intended to monitor [112]; secondly, sensors should be small enough so that the mechanical structures of monitored components are not affected. Cost of adding accelerometers in certain locations must not outweigh the benefits [113].

Referring to established accelerometers' installation in HUMS, emphases are on monitoring gears, bearings and shafts. Usually, a planetary speed reduction gearbox contains one or more layers of epicyclic modules. SA 330 helicopter MGB adopted in this study has 2 epicyclic modules, and thus the positioning of the accelerometers matters. In [114], it was stated that both 1^{st} and 2^{nd} epicyclic modules were monitored, before an update of system which reassigned one sensor to 1^{st} epicyclic module only, and another sensor at left aft module. This was then proven to have rendered all HUMS data and made analysis invalid. It is thus conclusive that accelerometers should be attached close to components which sensors are intended to monitor. Moreover, in [9], specific guidance has been given as sensors should be placed on critical drivetrain components and other components of high interest. Sensors mounted should have clear energy transmission paths from the specific components being monitored. Lastly, the sensor should be oriented such that the sensitive axis is aligned with the predominant axis of vibration.

In [11], an informative introduction showcasing the accelerometers installed in HUMS system was provided. The presented HUMS system utilised accelerometers and index sensors to continuously monitor rotor system and drivetrain. Accelerometers were mounted on the input and output of each major drivetrain assembly. In HUMS fact sheet [26] provided by Honeywell, it is clearly stated that 7 accelerometers have been

installed at engine-gearbox systems, including 2 at main gearbox input, 2 at engine turbines, 2 at engine accessory gearbox and 1 at main gearbox quill as shown in Figure 3.16.

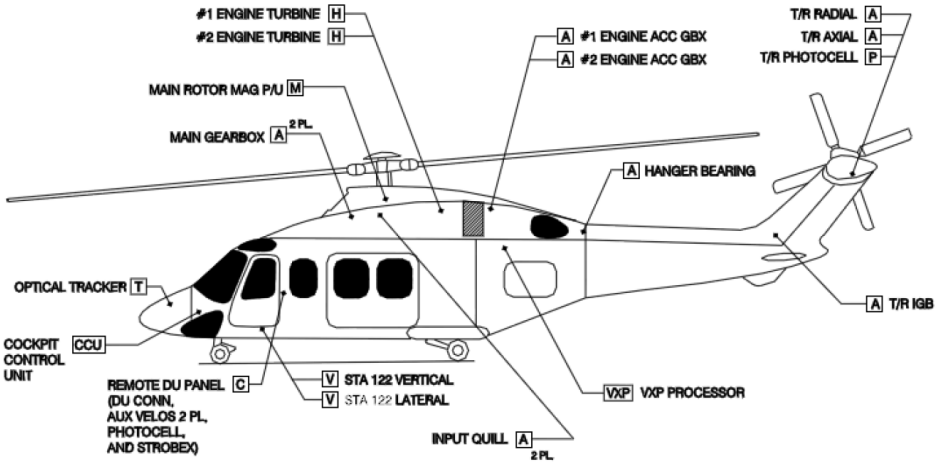

Figure 3.16: Demonstration of Honeywell HUMS [26]

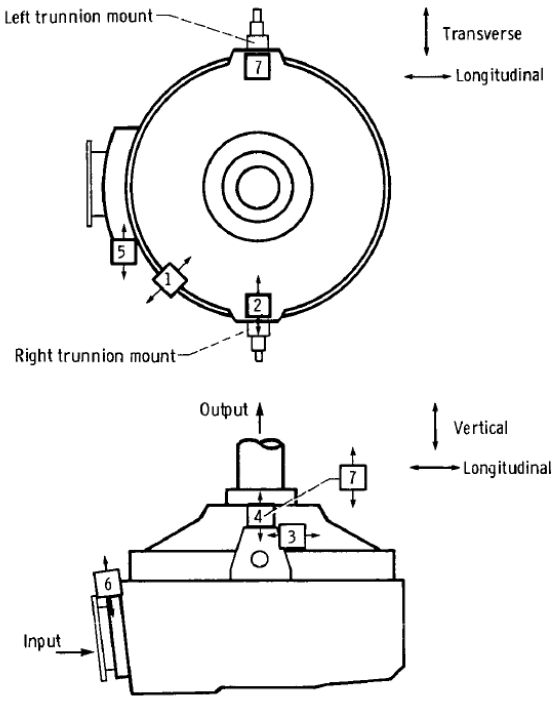

Figure 3.17: Demonstration of accelerometer locations on OH-58A MGB [27]

In [27], it is stated that 7 accelerometers were installed to monitor MGB, illustrated in Figure 3.17. Although the featured MGB was relatively an old type, the selection of

sensor locations suggested that covering possible planetary area is important for MGB health monitoring.

Combining all the knowledge aforementioned, 4 accelerometers were selected to be installed for this study, including 2 triaxial and 2 uniaxial sensors. No accelerometers were installed to monitor aft module since aft modules were left completely idle. The exact locations of 4 accelerometers were documented in Table 3.8. Pictures illustrating such arrangements are shown in Figure 3.18.

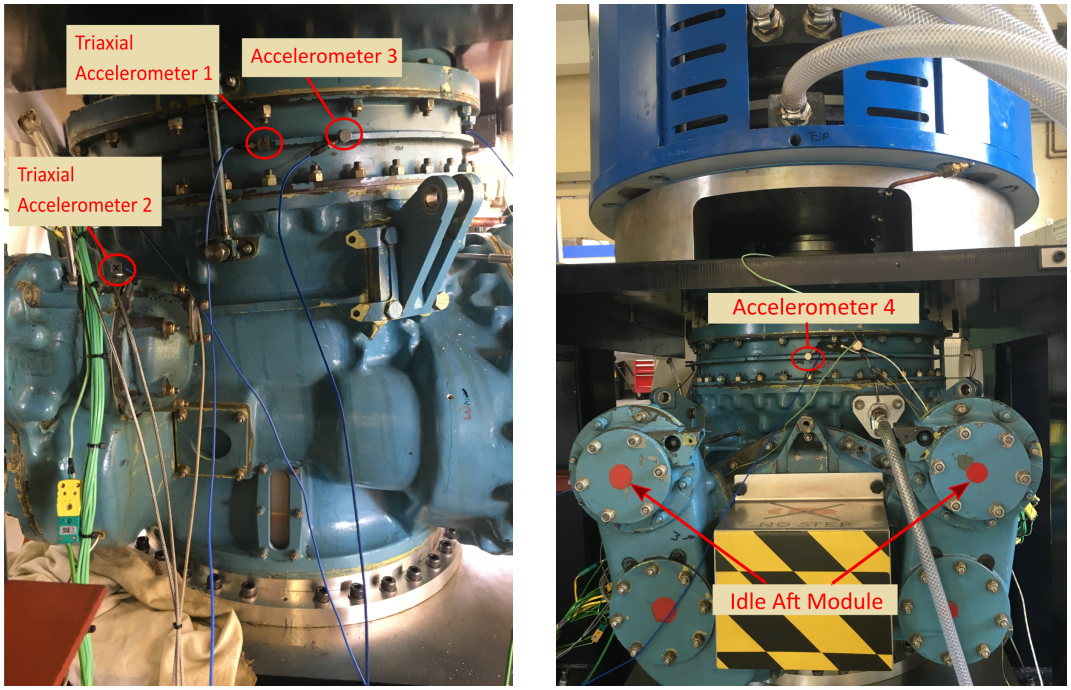

(a) Sensor installation side view (b) Sensor installation front view

Figure 3.18: Demonstration of accelerometers locations on SA330 MGB

Table 3.8: Installation locations of accelerometers

Sensor No.	Sensor Type	Location
1	Triaxial	Middle of 1^{st} and 2^{nd} epicyclic case
2	Triaxial	High speed input module
3	Uniaxial	Middle of 1^{st} and 2^{nd} epicyclic case
4	Uniaxial	Middle of 1^{st} and 2^{nd} epicyclic case

Originally, sensors with high sensitivities 100mV/g were considered to be employed. However, the study in [3] shows that such choice potentially could sacrifice the

measuring range. It was reported that the vibration collected from MGB can reach up to 500 g. Since the upper measuring limit for such sensors is 5V, the maximum monitoring range will be $\pm(5V \div 100mV/g) = \pm 50$ g. This value was proven to be far too small, that the sensors would be saturated. Thus, uniaxial accelerometer PCB 352C03 and triaxial accelerometer PCB 356A43 were selected (Table 3.9). Both of the accelerometers have 10 mV/g sensitivity, 500 g measuring range, and were stud-mounted onto the MGB external case. Vibration data recording was controlled by a computer connected to the main monitor throughout the experiments. Detailed data recording information are summarised in Table 3.10.

Table 3.9: Selected accelerometers

Axis	Model	Sensitivity	Dynamic Range	Resolution
Uniaxial	PCB 352C03	10 mV/g	±500 g pk	0.0005 g rms
Triaxial	PCB 356A43	10 mV/g	±500 g pk	0.0008 g rms

Table 3.10: Data acquisition information

Data Type	Data Card	Software	Sampling Frequency	Recording Length	Spectrum Resolution
Vibration	NI 9234	LabVIEW	25.6 kHz	20 seconds	$\frac{1 \text{ Hz}}{\text{Recording Length}}$

In Table 3.10, the recording length was chosen to be 20 seconds. This was considered sufficient for the diagnosis, because of the high speed of the rotating bearings. For instance, the speed of the planetary bearings under 14000 rpm condition is 11.35 Hz. This means the planetary bearing rotates roughly 220 repetitions in 20 seconds, which is sufficient to diagnose the defects.

3.3.3 Test Conditions and Procedures

The experiment undertaken on the MGB rig consisted of four parts, namely:

1. Test rig commissioning. Run the rig under various load conditions from 100 kW to 275 kW, and input speed from 10,000 rpm to 17,842 rpm input speed conditions,

to ensure full functionality of all aspects of the test rig and emergency lubrication system.

2. Seeded bearing defects tests. Operate the MGB with seeded bearings defects at 2^{nd} epicyclic module planetary bearing outer race, under various input speed and load levels. Vibration data should be recorded for post analysis and fault diagnosis.
3. Full lubrication tests and thermal mapping. Run the test rig under a variety of increasing speed and load conditions to ascertain the thermal equilibrium of various measured parts within the gearbox, and determine the rate to thermal growth for components.
4. Combined dry and mist lubrication tests. Test the performance of mist lubrication method as an emergency lubrication method under no lubrication condition.

As the thermal mapping and mist lubricant test are beyond the scope of this thesis, only the commissioning and the planetary bearing seeded defect test are discussed in this thesis.

The commissioning test was undertaken firstly to validate the setup of the test rig and the data acquisition system. Vibration data were recorded under 150 kW load condition. For the purpose of system validation, no fault was seeded at this point. The commissioning was performed by technicians from Cranfield University.

It was discovered from the commissioning that data collected under 9000 rpm input speed condition had severe data jitters and some traces of data-clipping. The problematic data was collected by sensor at forward module near input shaft. The result was illustrated in Figure 3.19. The two marked peaks at 0.7s and 7.5s occurred right after a sudden data jitter, and the lower part of the data were clipped at approximately -45 g. This observation suggested that, the input shaft connection should be double-checked and sensors with lower sensitivity should be adopted to avoid sensors saturation.

After changing the accelerometers to the ones listed in Table 3.9 to accommodate 500 g measuring range, another series of commissioning tests were undertaken. MGB was operated under 1000 rpm, 3000 rpm and 6000 rpm input speed conditions and a minimum load for commissioning purposes. After running the MGB under 6000 rpm for an extended period, a burning smell was sensed and test rig was shut down immediately

according to emergency protocol. Later inspection discovered that MGB was abnormally warm, while the shaft connection MGB assembly and the speed-increasing gearbox shown in Figure 3.20 were extremely hot. The shaft was then disassembled from the speed increasing gearbox for inspection.

In Figure 3.21(a), the damaged gears are shown. It was estimated that the temperature of the shaft gear was risen up to nearly 300°C. Figure 3.21(b) suggests that the ring gear became fragile, which was broken when being disassembled. After investigation, it was concluded that the MGB fault was contributed by possible misalignment (Figure 3.19) and manufacturing issues of the gears. Lessons learnt from the discoveries are summarised below.

1. It is recommended to perform multiple commissioning tests to fully evaluate the system robustness, this is exceedingly important, especially for validating all aspects and functionalities of helicopter MGB system.
2. The vibration level of a real helicopter MGB can easily rise up to approximately 500 g, which is incomparable by simple bearing system. The level of vibration also aggravates and facilitates the propagation of the incipient faults. On the other hand, the excessive level of vibration contributed by the gear meshes dramatically increases the difficulties of diagnosing incipient planetary bearing faults.
3. A single fault could result in rapid over heating while MGB is in operation, which strengthens the value of diagnosing the MGB defects in its incipient states

With aforementioned in mind, extra cautions were taken when operating the MGB for the planetary bearing seeded fault tests. The relationship of Torque T (Nm), Power P (W) and rotational speed ω (rad/s) is defined in the equation below:

$$P = T \times \omega \tag{3.7}$$

Given that the power P is a constant value during MGB operation, lower speed ω results in an increased torque T. Therefore, safety margins have been added to avoid too much torque being applied to key components.

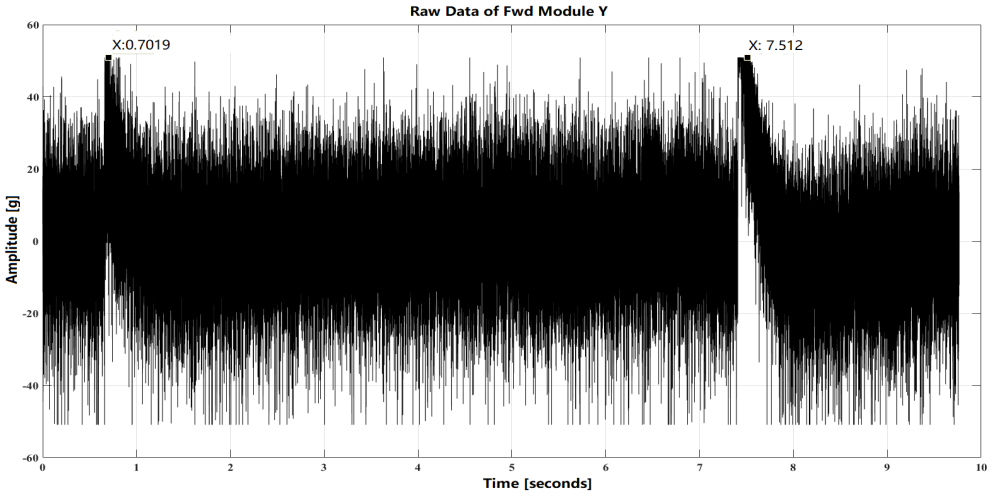

Figure 3.19: Anomaly found in commissioning test

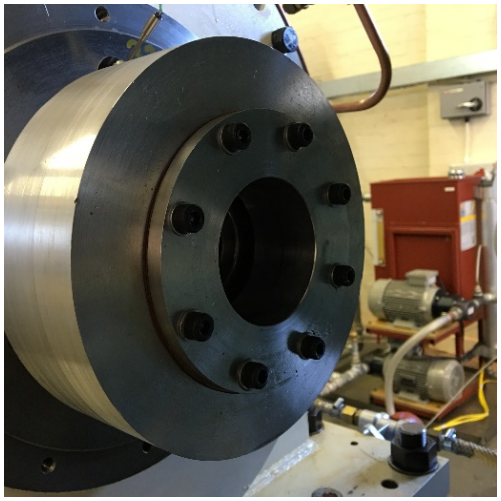

Figure 3.20: Speed increasing gearbox, after disassembling shaft

(a) Faulty shaft gear

(b) Faulty shaft gear and ring gear

Figure 3.21: Faulty gears identified in commissioning test

Having the information in mind, the first condition of seeded defect test was selected to be conducted under 14000 rpm and 100 kW load condition, which according to [3], was the power profile when helicopter remains idle on the ground before take-off. This test condition also enables the investigation on the feasibilities of diagnosing incipient planetary bearing faults without demanding the data from helicopter flying regimes. While the high speed DC motor has a maximum operating speed of 17842 rpm, the other speed condition was selected to be 16000 rpm, with a safety margin considered.

To comply with safety protocols, operations on MGB rig were all conducted from an isolated control room, shown in Figure 3.22. The main monitor in the control room simultaneously updated information of MGB such as input drive speed, DC motor power, temperature of MGB and so on. Emergency stop button was located at control panel, which can be used to shut down the entire system.

Figure 3.22: Control room

Tests under healthy conditions were undertaken first, followed by tests under minor fault and major fault conditions. Between tests of different health conditions, MGB was stripped for at least 3 days to allow the planetary bearings to be replaced. For each test, in between of different speed and load conditions, quick checks on vibration data were performed. The test conditions are summarised in Table 3.11. The 10000 rpm condition test was conducted as a third commissioning, while the extra 16,000 rpm, 220 kW load test was carried out only under major fault condition, for the purpose of acquiring data

near rig operational limitations.

Table 3.11: Seeded bearing defect tests conditions

Speed (rpm)	Health Condition	Load Condition (kW)	Test Notes
10,000	Healthy	80	For commissioning
14,000	Healthy	100, 180	–
	Minor Fault	100, 180	–
	Major Fault	100,180	–
16,000	Healthy	100, 180	–
	Minor Fault	100, 180	–
	Major Fault	100, 180, 220	For only major Fault

3.4 Summary

In this Chapter, the experiments undertaken to acquire vibration data from helicopter MGB, operated under various conditions are described. In Section 3.2, the external and internal structure of the MGB is described and illustrated. The fundamentals of the planetary speed reduction system and the equations for determining the speed reduction ratios are explained. Specifically, the reduction ratios in the adopted SA330 MGB are calculated with the information of sun and ring gear teeth given in Table3.2. The components of the test rigs are introduced, and a schematic view is drawn in Figure 3.5 showing how the rig components were assembled. The seeded bearing defects are described, the size of the seeded defects were decided to be incipient, that the integrity of the planetary bearing was not compromised, making the diagnosis increasingly challenging and rewarding. The description of data acquisition system setup is given afterwards, followed by the explanation of test conditions and procedures. Considerations were given for determining experiments conditions to investigate the feasibility of diagnosing incipient planetary bearing fault in a more relaxed helicopter regime, i.e. ground idle before take-off, further increasing the diagnosis difficulties. A possible imbalance or material issue was encountered during commissioning of the test rig, which lead to an emergency shut down. Key points have been summarised in Section 3.3.3, providing valuable information that can be adopted to other researches

conducted on helicopter MGB. Experimental vibration data has been successfully captured at various test conditions using MGB test rig. To recapitulate, vibration data was collected from eight data channels (two triaxial and two uniaxial sensors). Summarised in Table 3.11, data under three conditions including healthy, minor fault and major fault, two speed conditions including 14,000 rpm and 16,000 rpm and various load conditions were collected for the analysis. The diagnosis work using the collected data will be discussed in detail in Chapter 4.

Chapter 4

Planetary Bearing Fault Diagnosis on SA330 MGB

4.1 Introduction

In Chapter 3, the details of the planetary bearing seeded defect tests undertaken on a SA330 MGB have been presented. In this Chapter, the diagnoses of the seeded defects, including minor defect and major defect, are performed using the collected experiment data.

4.2 Methodology

Over the last two decades, significant researches have been conducted in the study of bearing fault diagnosis. Many of the researches have reported prominent achievements, notably the below techniques: in [66, 69], Ho and Randall implemented self-adaptive noise cancellation (SANC) technique to separate deterministic gear mesh signals and non-deterministic bearing signals. Such technique was further evaluated extensively in [64, 67, 73]. Envelope analysis has been established as a benchmark technique to extract the diagnostic information hidden in high frequency resonances [18, 88, 107]. Antoni and Randall developed Kurtogram based on the concept of SK, and proposed using Kurtogram as a frequency resonance detector in conjunction with envelope analysis [94]. The other techniques that were reviewed in Chapter 2 all have gained success for their own utilities. Implementing the aforementioned techniques has undoubtedly achieved successes on diagnosing bearing fault, but most of these investigations were carried out on simulated data or experimental data taken from bearings in a relatively simple system or test rig. An actual operational helicopter MGB is a very sophisticated mechanical system, containing multiple speed reduction modules and planetary stages. Therefore, vibration data collected from helicopter MGB reflects

complex mechanics of interactions between gears and bearings in MGB that can hardly be simulated. Diagnosis of planetary bearing defects in an operating MGB is eminently challenging, the reasons are summarised below, including but not limited to [115]:

1. Epicyclic modules of MGB can achieve a large reduction rate of approximately 86:1 (calculated based on test rig MGB). Such functionality is achieved by a sophisticated multi-stage epicyclic speed reduction structure, which are formed by many planetary gears and bearings. This structure further complicates signal transmission paths for accelerometers, hence vibration data collected are highly modulated, which potentially masks fault related signatures.
2. Decided by the structure of planetary gear/ bearing set, gears and bearings share same races, resulting in overwhelming gear meshes signal masking planetary bearing signals that are inherently weak. Thus, faulty signatures excited by contacts between defects and rollers/ cages are difficult to be extracted.
3. An operating helicopter MGB, especially in high-speed mode, generates extremely large noise from the gear meshes and shaft rotations. Signal-to-noise ratio is not idea for direct clear diagnosis under such harsh circumstances.
4. Traditional HUMS CIs are generated based on statistical characteristics of vibration data, however, the information that these statistical features convey can be misleading. For example, kurtosis can be used to describe if the collected vibration data contains more peaks than a normal distributed data. Thus, an increase in kurtosis usually indicates the development of defects. However, kurtosis will lose its validity once the initial defects propagate into more distributed or severed defects, when the value of kurtosis starts to decrease.

To investigate on diagnosis of planetary bearing outer race defects, using the vibration data collected from the experiments in Chapter 3, below steps were followed to validate the effectiveness of the frequency domain processing techniques aforementioned.

1. Perform a data quality check to make sure that no obvious data breakage has occurred during acquisition.

2. Perform FFT analysis and bicoherence analysis, investigating the feasibilities of applying high-order frequency analysis for planetary bearing fault diagnosis.
3. Based on the primary results from previous steps, investigate the necessities and effectiveness of gear/bearing signal separation techniques on removing the interfering gear meshes.
4. Evaluate the effectiveness of envelope analysis and IEC to identify the fault-associated frequencies defined in Equation 2.14. Additionally, analysis such as SK, and manual structural resonance extraction are to be performed to acquire optimal centre frequency and bandwidth for envelope analysis and IEC.
5. Establish a routine that is optimal for helicopter planetary bearing diagnosis.

4.3 Data Quality Overview

As discussed in previous Section, firstly the raw waveform of the vibration data was checked prior to detailed signal processing. In Table 3.8, it has been described that four accelerometers were employed, where two were triaxial and the other two were uniaxial. For triaxial accelerometers, X, Y, Z was used to denote the directions of their sensitive axes. X axis was in the tangential direction to the MGB case, Y axis was in the radial direction to the MGB case and Z axis was in the vertical direction. Based on the axis feature, the vibration waveforms recorded under 14000 rpm, 100 kW condition are plotted, showing the 6 channels of data from triaxial accelerometers, namely forward module X, Y, Z axes (sensor 2 in Table 3.8) and epicyclic module X, Y, Z axes (sensor 1 from Table 3.8) in Figure 4.1 to Figure 4.6. The data from uniaxial accelerometer (sensor 3 from Table 3.8) is plotted in Figure 4.7. Basic information is observed that:

1. From the observation of epicyclic module data (plotted from Figure 4.1 to Figure 4.3), the vibration data recorded in X channel has the smallest amplitude, which was less than 80 g, whereas the data from Y and Z channels are relatively similar. This observation indicated that, when the planetary bearings were rolling with the carrier and passed by the accelerometers at epicyclic module, the radial and tangential directions have had the most impact from the epicyclic planetary bearings.
2. From the observation of the forward module data (plotted from Figure 4.4 to

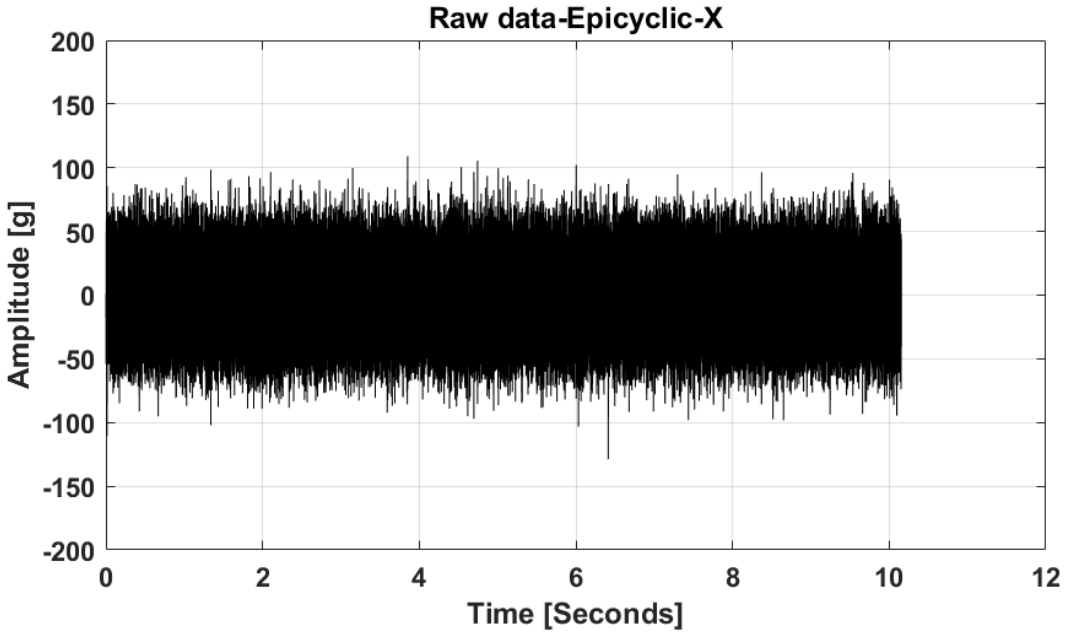

Figure 4.1: Triaxial accelerometers 1 recording from epicyclic module, X-axis

Figure 4.6), the data in Y channel has the largest amplitude of nearly 500 g. However, the transmission paths from the 2^{nd} planetary faulty bearings to the forward module are not straightforward, i.e. the signal associated with bearing defects had to pass through the rotating two-stage epicyclic modules before received by Forward Module accelerometers. Therefore, the data from forward modules were primarily recorded to monitor the status of the coupling gears from the speed-increasing gearbox, and were not optimal for planetary bearing diagnosis.

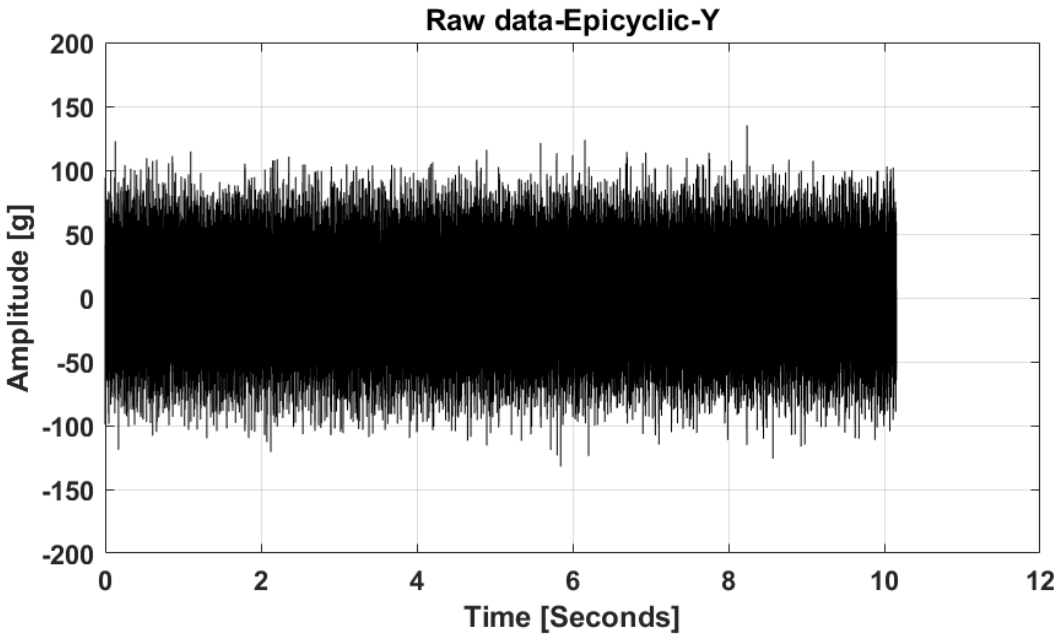

Figure 4.2: Triaxial accelerometers 1 recording from epicyclic module, Y-axis

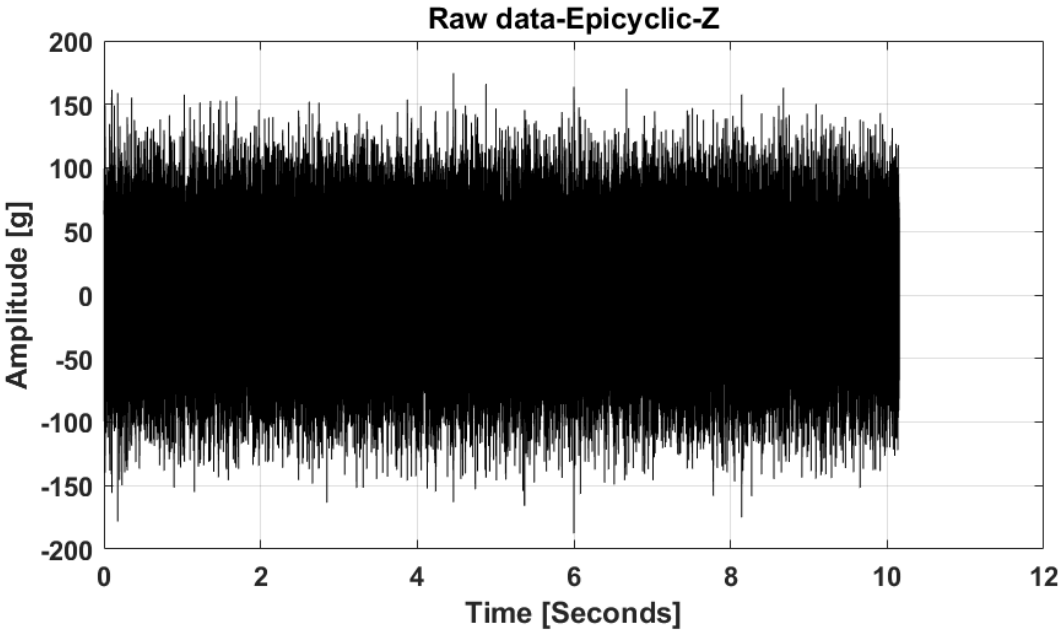

Figure 4.3: Triaxial accelerometers 1 recording from epicyclic module, Z-axis

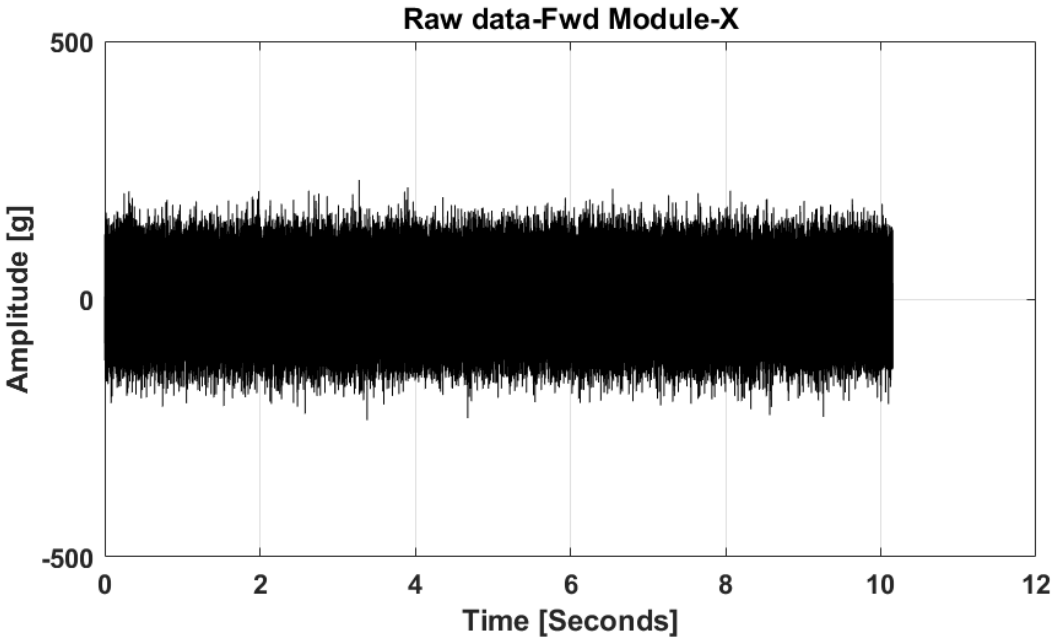

Figure 4.4: Triaxial accelerometers 2 recording from forward module, X-axis

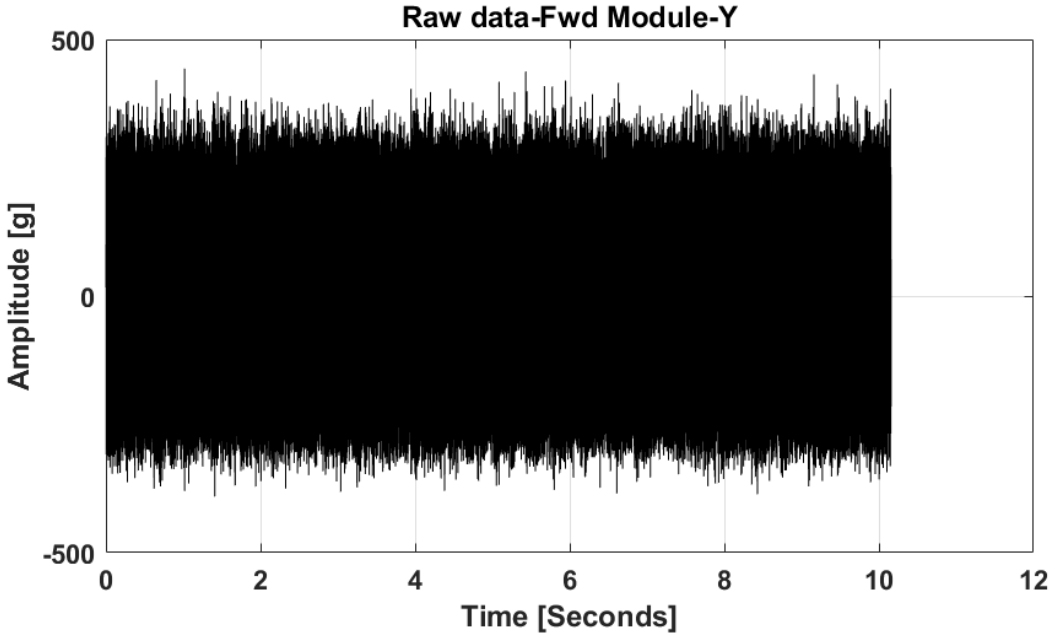

Figure 4.5: Triaxial accelerometers 2 recording from forward module, Y-axis

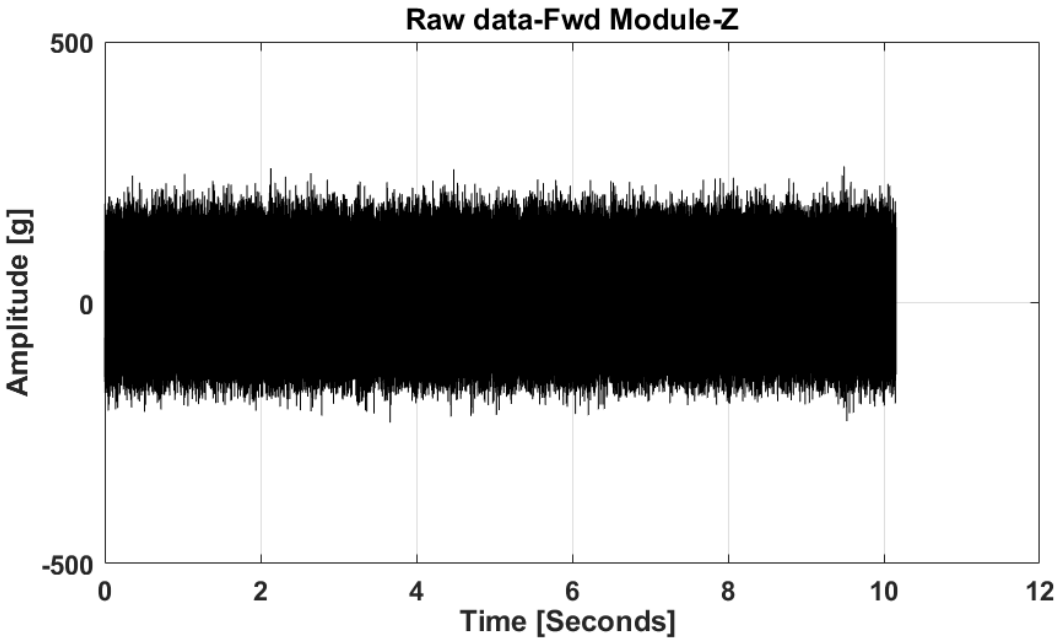

Figure 4.6: Triaxial accelerometers 2 recording from forward module, Z-axis

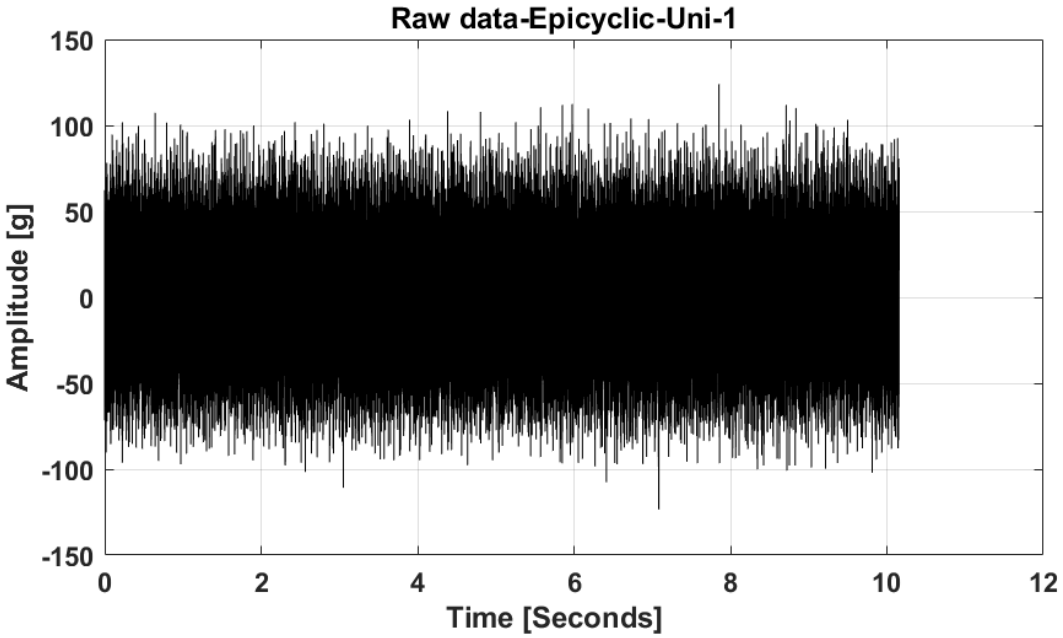

Figure 4.7: Uniaxial accelerometers 3 recording from epicyclic module

Table 4.1: Diagnostic parameters of 14000 rpm, 100 kW condition

Conditions	Load	Speed	F_{sampling}	BPFO	ω_{c1}	ω_{c2}
Healthy	100 kW	14034 rpm	25600 Hz	N/A	7.90 Hz	2.71 Hz
Minor Fault	100 kW	14088 rpm	25600 Hz	59.67 Hz	7.93 Hz	2.72 Hz
Major Fault	100 kW	14120 rpm	25600 Hz	59.81 Hz	7.95 Hz	2.73 Hz

4.4 Investigation on Vibration Data Analysis

4.4.1 Diagnosis on Vibration Data Collected at 14000 rpm, 100 kW Condition

Following the steps described in Section 4.2, the data collected from the speed condition 14000 rpm, load condition 100 kW was firstly examined. Using pre-determined parameters from Table 3.2, and the Equation 3.6 to calculate BPFO, the relevant diagnostic information is presented in Table 4.1, where ω_{c1} is the frequency of 1^{st} epicyclic planetary carrier rotation speed (476.3 rpm), and ω_{c2} is the frequency of 2^{nd} epicyclic planetary carrier rotation speed (163.8 rpm). To investigative results in frequency domain, the unit of speed is converted from rpm to Hertz.

As stated in Section 4.2, after checking the data quality, the candidates for signal processing are shortlisted to data collected from channels including epicyclic uniaxial channel 1, and epicyclic triaxial channel Y, and Z. It was decided that the focus should be on the channel that maintained a straightforward transmission path, and the vibration should be received by the sensitive axis of the accelerometers. Therefore, based on the transmission schematic diagram shown in Figure 3.13, the data from channel epicyclic triaxial Y (radial axis) was selected for the bearing fault diagnosis, while the other channels were only used to provide supplementary information when necessary.

Figure 4.8 shows the amplitude spectrum created using data from epicyclic channel Y, demonstrating the evident link between frequency components to physical gearbox rotating mechanism. A number of dominant frequency components are marked in the Figure 4.8 to support this observation. It can be deduced that these frequencies are all

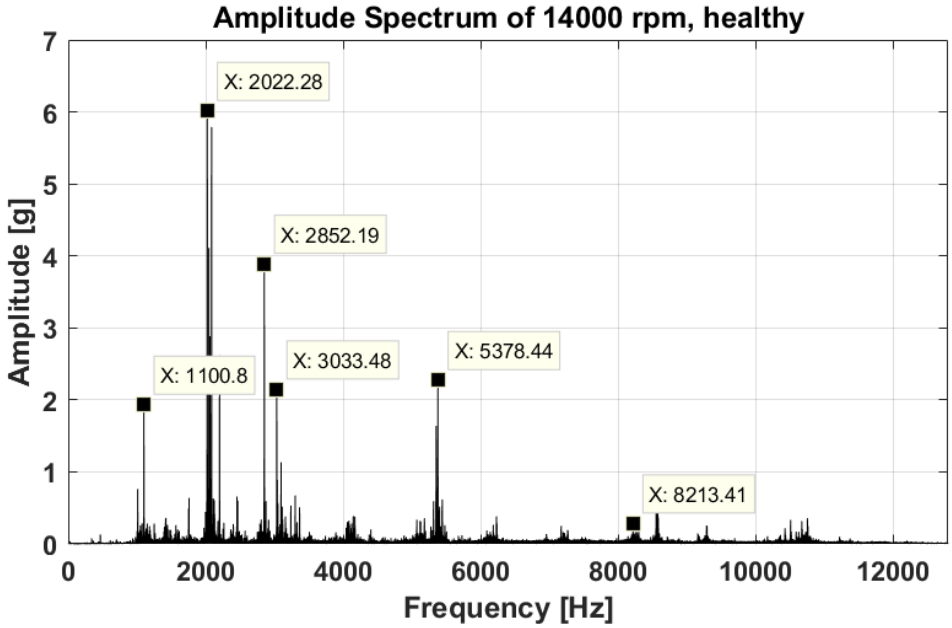

Figure 4.8: Frequency spectrum of healthy condition under 14000 rpm and 100 kW load

related to overwhelming gear meshes or the modulated frequencies induced by the 1^{st} and 2^{nd} planetary carrier plates. The explanations for these frequency components are detailed in below.

1. Frequency 5378.44 Hz: this frequency is the gear mesh frequency of the forward module. High input speed 14034 rpm generated from the DC motor was not reduced at this point. Gear mesh frequency is calculated by multiplying the gear spinning speed with its number of teeth. Therefore, the Gear Mesh Frequency (GMF) is calculated as:

$$GMF_F = \frac{14034}{60} \times 23 = 5379.7\ Hz \tag{4.1}$$

   where 23 is the number of pinion teeth in forward module (Figure 3.2).

2. Frequency 2852.19 Hz: this frequency can be related to the gear mesh frequencies in the aft module. The speed can be deduced from the input speed of 14034 rpm combining the teeth information of forward and aft Module. The calculation is presented in below:

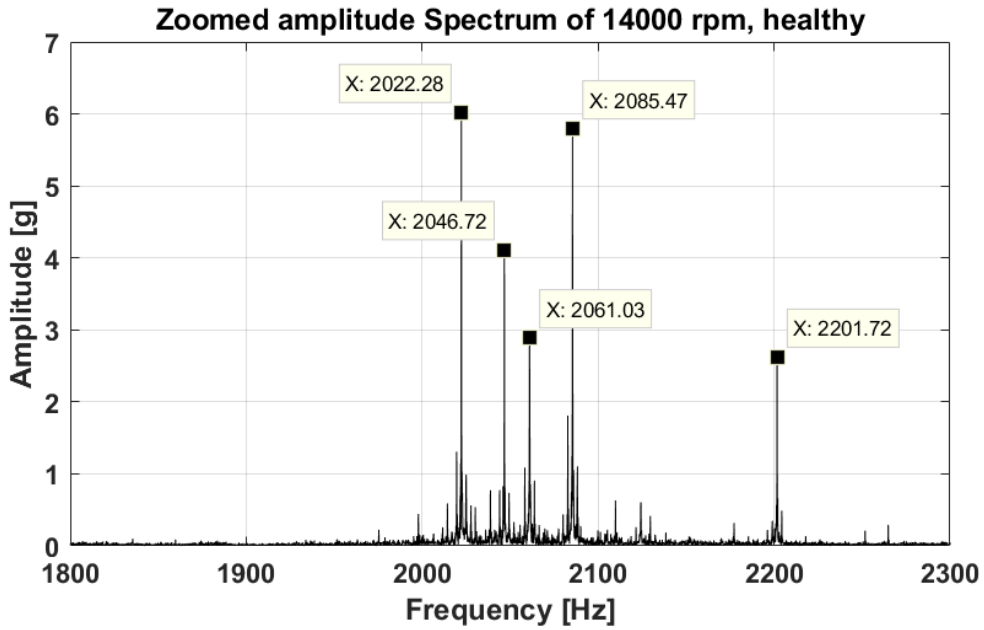

Figure 4.9: Zoomed spectrum of healthy condition under 14000 rpm and 100 kW load

$$GMF_A = \frac{GMF_F}{23} \times \frac{23}{66} \times 35 = 2852.87\ Hz \tag{4.2}$$

where the 23/66 pair is the speed ratio of forward module, and 35 is the number of pinion teeth in aft module.

3. Frequency 1100.8 Hz: this is caused by the gear meshes at bevel stage. Referring to the speed ratio and gear teeth information in Section 3 Table 3.2, the rotating speed at bevel gear is:

$$GMF_B = \frac{GMF_A}{35} \times \frac{35}{57} \times 22 = 1101.1\ Hz \tag{4.3}$$

where the 35/57 pair is the speed reduction ratio from the aft reduction gears; 22 is the number of pinion teeth in bevel gear.

4. Frequency 2022.28 HZ: this frequency can be correlated with the gear mesh frequency from the 1^{st} planetary gears. In order to fully investigate on this frequency component, the frequency spectrum in Figure 4.8 is zoomed to a narrower range of [1800 Hz, 2300 Hz], and shown in Figure 4.9.

   It has been revealed that, 2022.28 Hz and 2046.72 Hz have a difference equal to that between 2061.03 Hz and 2085.47 Hz, which is exactly 24.44 Hz. However,

the difference between the two frequencies in the middle, namely 2046.72 Hz and 2061.03 Hz, is 14.31 Hz. Therefore, these four frequencies are not harmonics of a certain frequency, which usually should have identical intervals. The explanation for this phenomenon is that, they are sidebands induced by amplitude modulation from the planetary movement of the carrier plate. Since the planetary gears were self-spinning while orbiting the sun gears, carried by the carrier rotating in a slower speed, the self-spinning speed of the gears will be modulated by the carrier speed when received by the transducers. It is therefore conclusive that a centre frequency 2053.88 Hz (the average of 2046 Hz and 2061 Hz) is missing in Figure 4.9, due to the amplitude modulation.

To prove this conclusion through calculations, firstly the planetary gear mesh frequency is obtained. There are two methods of calculating this frequency component: using the carrier speed times ring gear teeth number, or using planetary gear self-spinning speed times the number of its gear teeth. For simplicity, using the already given 1^{st} carrier speed ω_{c1} in Table 4.1, we have the 1^{st} planetary gear mesh frequency:

$$GMF_{P1} = \omega_{c1} \times 130 = 7.90 \times 130 = 1027.2\ Hz \tag{4.4}$$

It is obvious that frequency 2054 Hz is $2\times$ of the 1^{st} planetary gear mesh frequency, and the rest frequencies in Figure 4.9 are the sidebands modulated by either $1\times$ or $2\times$ the 7.9 Hz carrier speed. This conclusion suggests that, in a complex MGB, it is common that the frequencies are modulated severely, and cannot be observed directly. But modulation sidebands are helpful for identifying the missing frequencies.

5. Frequency 8213.41 Hz: this frequency is the total gear mesh frequency from the 1^{st} planetary gears. From the Table 3.1, there were eight 1^{st} planetary gears/bearings, therefore the total meshes are:

$$GMF_{Total} = GMF_{P1} \times 8 = 8217.6\ Hz \tag{4.5}$$

From the aforementioned observations and calculations, the links between the primary

rotating components in MGB and the frequency spectrum are established. Additionally, it is conclusive that the even though the accelerometers were placed at 2^{nd} epicyclic module, the spectrum is still dominated by the overwhelming gear meshes from 1^{st} epicyclic module. This finding has inevitably increased the difficulties of diagnosing the fault, which was seeded at 2^{nd} epicyclic module.

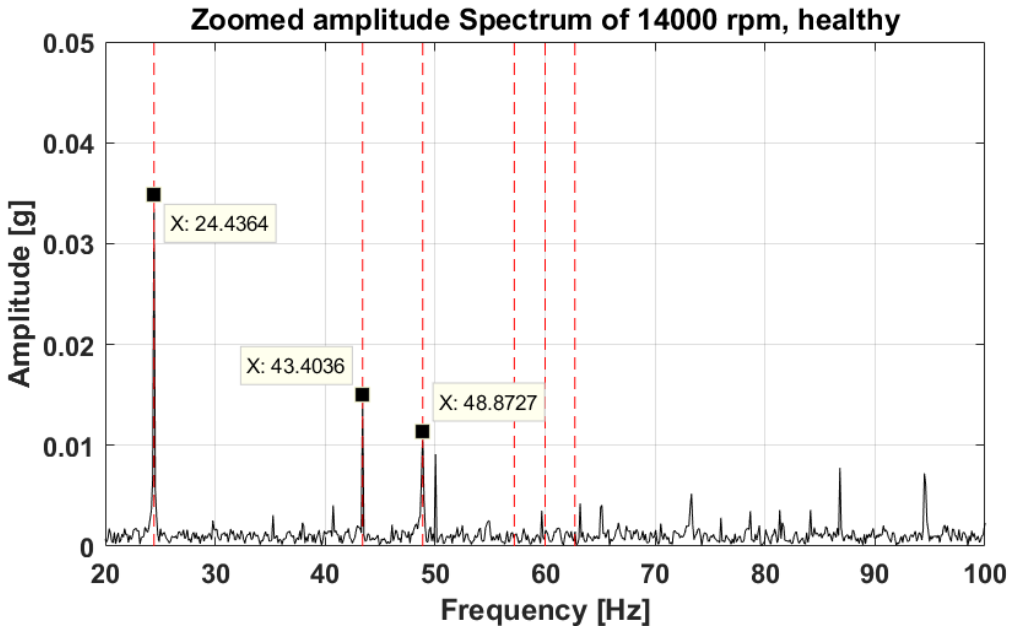

Figure 4.10: Zoomed spectrum of the data, 14000 rpm, 100 kW, healthy

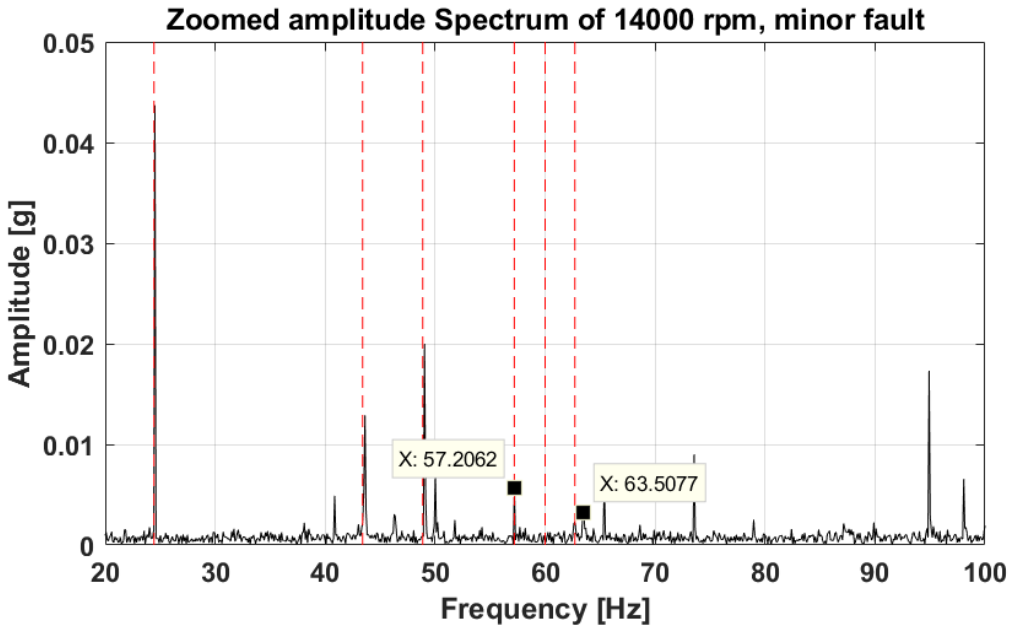

Figure 4.11: Zoomed spectrum of the data, 14000 rpm, 100 kW, minor fault

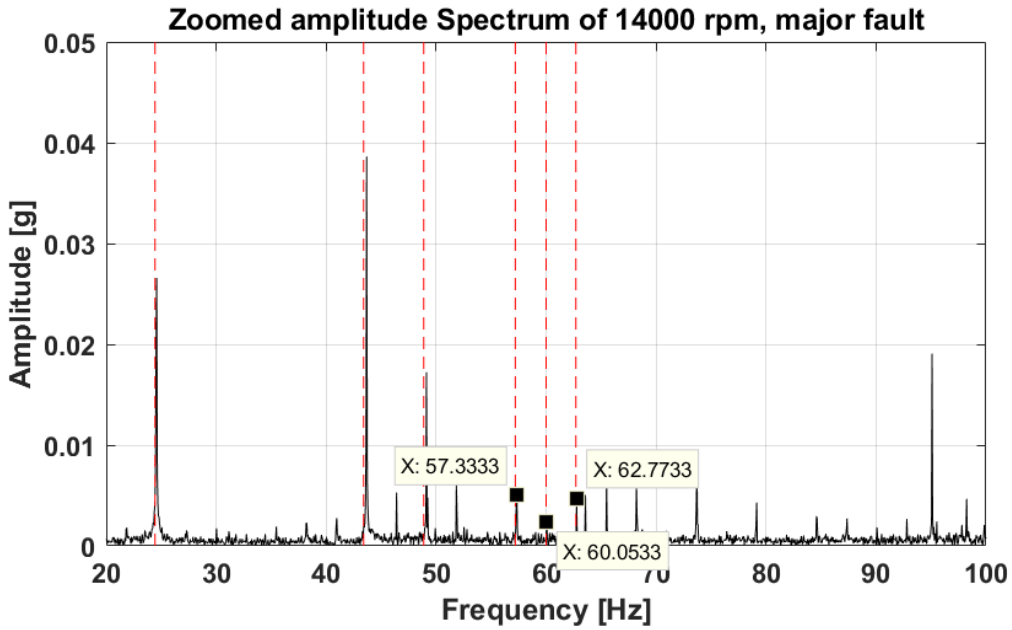

Figure 4.12: Zoomed spectrum of the data, 14000 rpm, 100 kW, major fault

In Figure 4.10, 4.11 and Figure 4.12, the frequency spectra for healthy, minor fault, and major fault are zoomed to [20 Hz, 100 Hz], to discuss the fault-related frequency patterns. In these three graphs, the locations of five relevant frequencies have been highlighted using vertical dashed lines. Due to the slight differences in operational speeds, the frequencies may have a small deviation to the dashed lines. These highlighted frequencies from lowest to the highest are:

1. 24.44 Hz, which is resulted from effect of the nine 2^{nd} planetary gears passing the accelerometers. The calculation is given:

$$\omega_{c2} \times 9 = 2.71 \times 9 = 24.39\ Hz \tag{4.6}$$

   The 48.87 Hz is the 2^{nd} harmonics of this frequency.

2. 43.40 Hz, which is induced from the 1^{st} planetary sun gear speed, modulated by the 2^{nd} planetary carriers. The calculation is:

$$\left(\frac{GMF_B}{22} \times \frac{22}{45} - \omega_{c2}\right) \times 2 = 43.51\ Hz \tag{4.7}$$

3. 57.21 Hz and 62.72 Hz in minor fault conditions shown in Figure 4.11, as

introduced earlier in this section, are sidebands caused by the faulty planetary bearing driven and modulated by the 2^{nd} planetary carrier plates. The calculations are:

$$BPFO + \omega_{c2} = 62.39\ Hz \tag{4.8}$$

$$BPFO - \omega_{c2} = 56.95\ Hz \tag{4.9}$$

Noted that the deviations between calculated values and actual values in the spectrum are caused by the bearing roller slips, and the small variation in MGB operational speed.

4. 60.05 Hz in major fault condition, found in Figure 4.12, is the BPFO calculated in Table 4.1.

It is observed from Figure 4.10, 4.11 and Figure 4.12 that, the frequencies that are not associated with bearing outer race faults, i.e. 24.44 Hz, 43.40 Hz and 48.87 Hz are present in all three conditions. However, the fault related sidebands and BPFO can only be seen in Figure 4.11 and Figure 4.12. Thus, it is conclusive that the primary goal of this study is to further investigate the effectiveness of the frequency domain processing techniques to extract the fault related frequencies, so that BPFO in Figure 4.11 can also be observed, without the interferences from other dominant gear mesh frequencies.

Following the processing steps in Section 4.2, the applicability of high-order frequency analysis, namely the bicoherence method, was firstly investigated. The bicoherence was calculated following the equation:

$$bic^2(f_1, f_2) = \frac{|X(f_1)X(f_2)X^*(f_1+f_2)|^2}{|X(f_1)X(f_2)|^2|X^*(f_1+f_2)|^2} \tag{4.10}$$

where X denotes the frequency components, and X^* is the conjugate pair of the component. Since in previous analysis, the details and validations of frequency related calculations have been given, the calculations of frequency components will be simplified in the rest of the Chapter. The diagonal slice of the calculated bicoherence matrix were selected, and shown from Figure 4.13 to Figure 4.15 for healthy, minor fault

and major fault conditions respectively. The relationship of a specific frequency component f and its 2^{nd} harmonics $2 \times f$ are revealed in this diagonal bicoherence plot. Conclusions can be drawn that the gear meshing frequencies and their harmonics have phase correlations. In all three conditions, bicoherence values at 24.22 Hz (9×2.73 Hz), 49.22 Hz ($2\times$ 24.22 Hz), 234.4 Hz (14000 rpm input speed) and 468 Hz ($2\times$ input speed) are eminently distinct. In minor fault and major fault condition, these values have several Hertz offsets caused by speed fluctuation. There are no distinct bicoherence indications of the BPFO in all three conditions. This indicates that, bicoherence is a method of detecting phase correlations between frequency components and their harmonics, and it is insensitive to bearing-related signals, which are not completely deterministic. Additionally, performing bicoherence analysis is very computational heavy, resulting in a compromised frequency resolution in order to improve the efficiency. This also contributed to the unsuccessfulness of detecting incipient BPFO components. Therefore, bicoherence is not ideal for the purpose of this study.

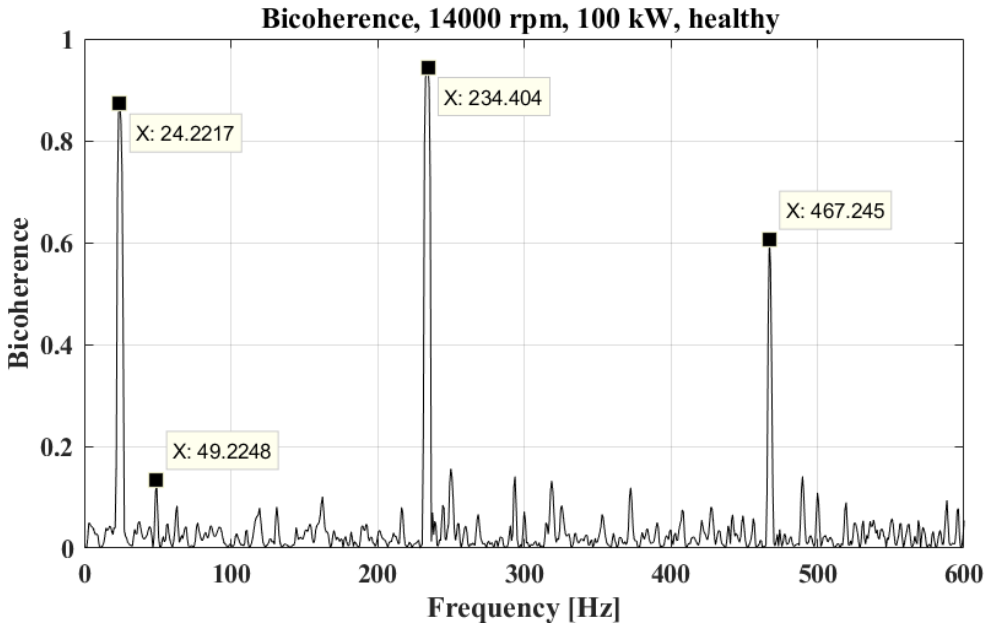

Figure 4.13: Bicoherence of healthy condition, 14000 rpm, 100 kW

The bicoherence results have shown the necessity of removing deterministic gear related frequencies. Additionally, as shown in Figure 4.11 and Figure 4.12, same conclusions can be drawn that dominant gear mesh frequencies should be removed to extract the bearing related nondeterministic signals. Randall's study [45] suggested that applying

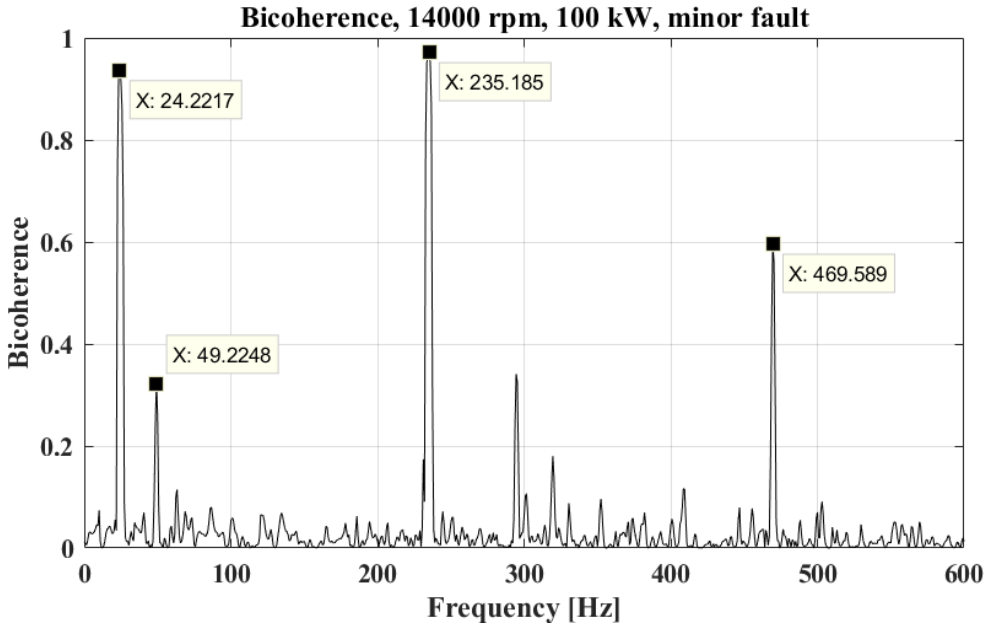

Figure 4.14: Bicoherence of minor fault condition, 14000 rpm, 100 kW

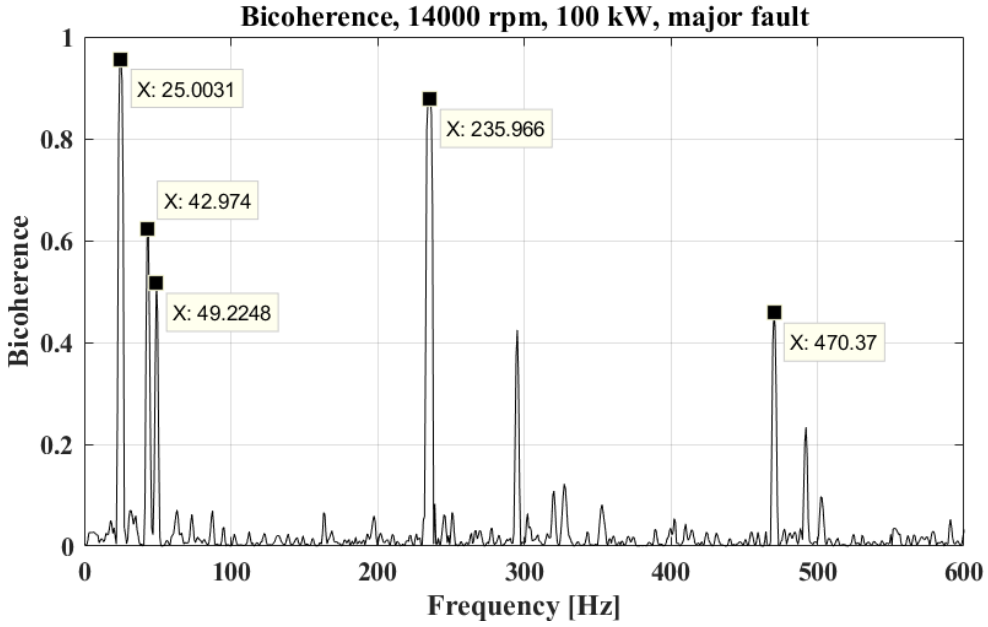

Figure 4.15: Bicoherence of major fault condition, 14000 rpm, 100 kW

gear and bearing signal separation using SANC technique will improve signal-to-noise ratio eminently. SANC was thus applied to process the data. The parameters of the SANC filters are critical. As explained in Chapter 2, SANC works well when the delay signal is properly selected so that the deterministic gear signals remain correlated while nondeterministic bearing signals are not. Based on the recommendation from [45], the

delay has been selected with the consideration of at least 20 times the period of the frequency band, where the demodulation is likely to take place. As in our study, the demodulation frequency can be up to 10k Hz with a bandwidth of 400 Hz, a good estimation of the delay, denoted as d, can thus be given as:

$$d = \frac{1}{400} \times 20 \times 25600 = 1280 \tag{4.11}$$

The delay d was used to develop the SANC filter, whose effects are shown in Figure 4.16 and Figure 4.17. The two figures both show that the deterministic frequencies in raw data are suppressed across the entire frequency domain, notably the 2030.77 Hz, 2864.15 Hz, 5376.49 Hz, 8592.34 Hz in minor condition, and correspondingly 2034.45 Hz, 2869.33 Hz, 3051.68 Hz, 5410.77 Hz, 8607.79 Hz in major condition, which are all related to gear mesh frequencies as explained earlier in this section. This result indicates that SANC is very powerful in preserving most nondeterministic signals that are associated with bearings, and it is applicable to planetary gear/bearing signal separation with proper delay selected.

After the separation, Kurtogram was performed to determine optimal bandpass frequency bandwidth and centre frequency for envelope analysis, where latter is used as a bearing fault identifier. The result of the produced Kurtogram is given in Figure 4.18 using minor fault data. The MATLAB code was provided by the inventor of Kurtogram algorithm, Dr. J. Antoni. It was discovered that applying SANC in 14000 rpm, 100 kW condition was not successful.

In Figure 4.18(a), the most impulsive frequency band detected by Kurtogram in the SANC filtered signal is centred in 150 Hz, with a bandwidth of 100 Hz. This is to say that Kurtogram has detected that the most impulsive frequency components are hidden in the frequency range of [100 Hz, 200 Hz], which is apparently inaccurate from Figure 4.16, showing no resonances in this frequency range. Although, the spectral kurtosis has been detected to be slightly higher than that shown in the Kurtogram of original signal in Figure 4.18(b), similarly, the correct resonance frequency was not detected.

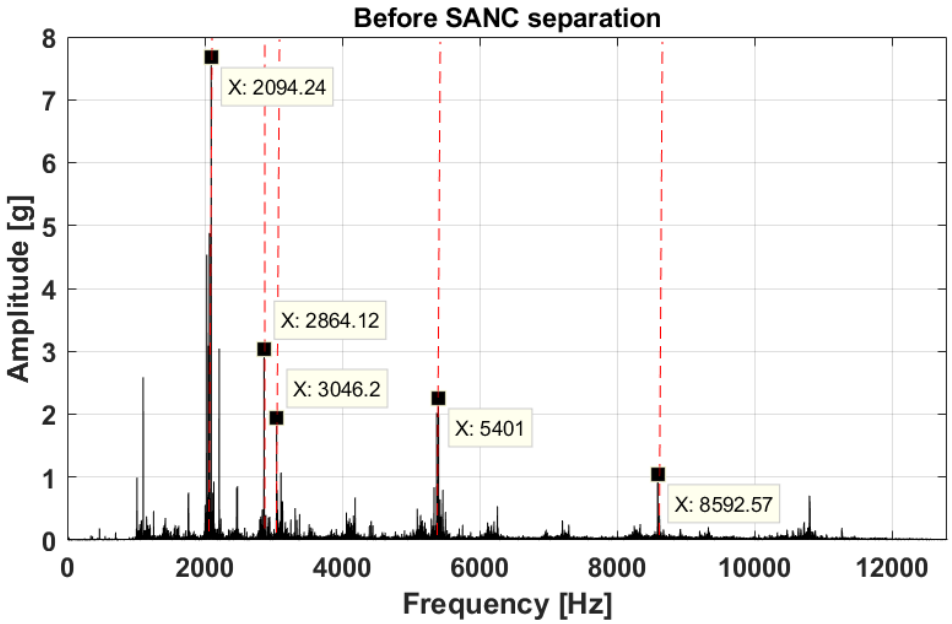

(a) Before separation

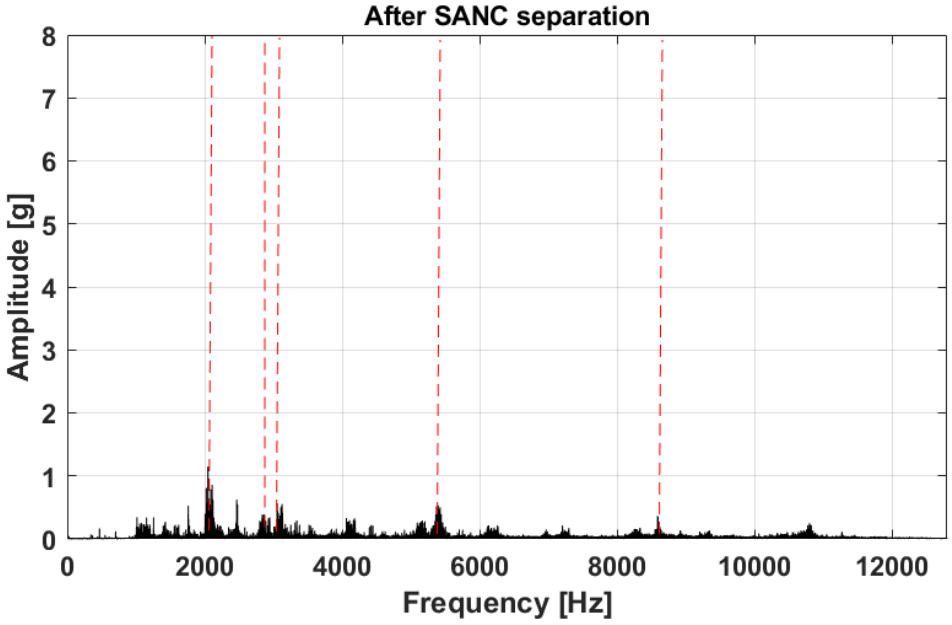

(b) After separation

Figure 4.16: Demonstration of SANC separation, 14000 rpm, 100 kW minor fault condition

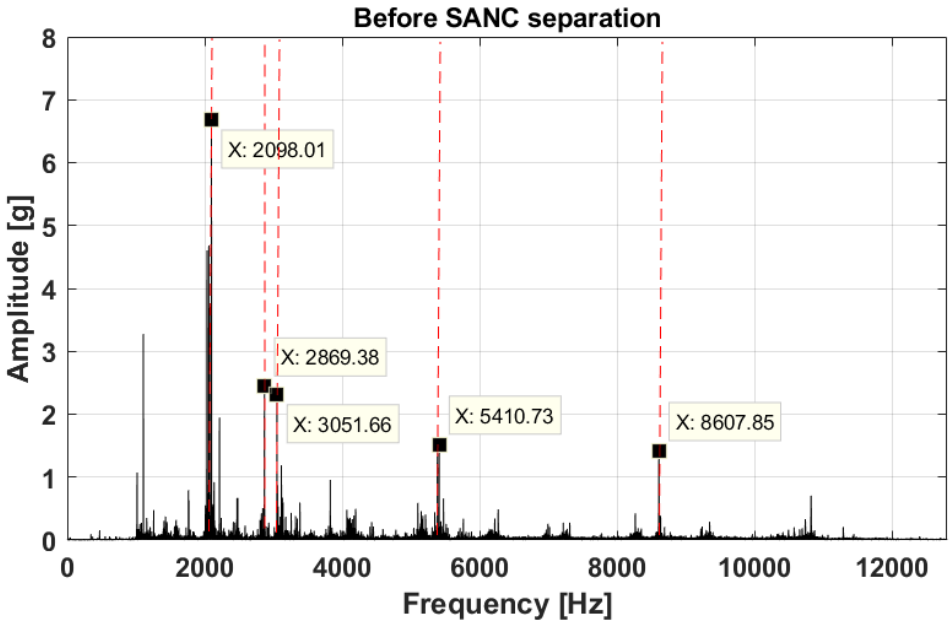

(a) Before separation

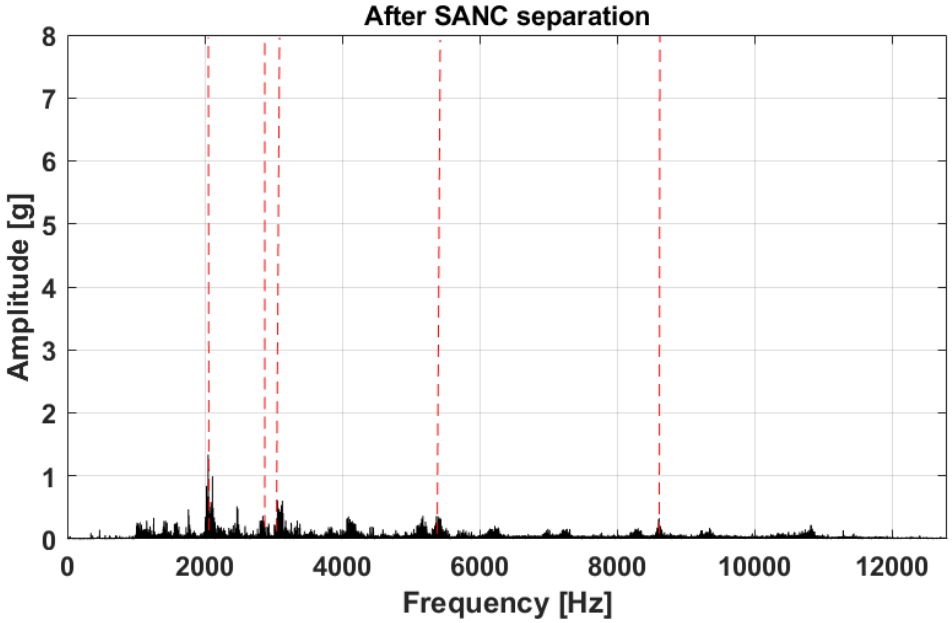

(b) After separation

Figure 4.17: Demonstration of SANC separation, 14000 rpm, 100 kW major fault condition

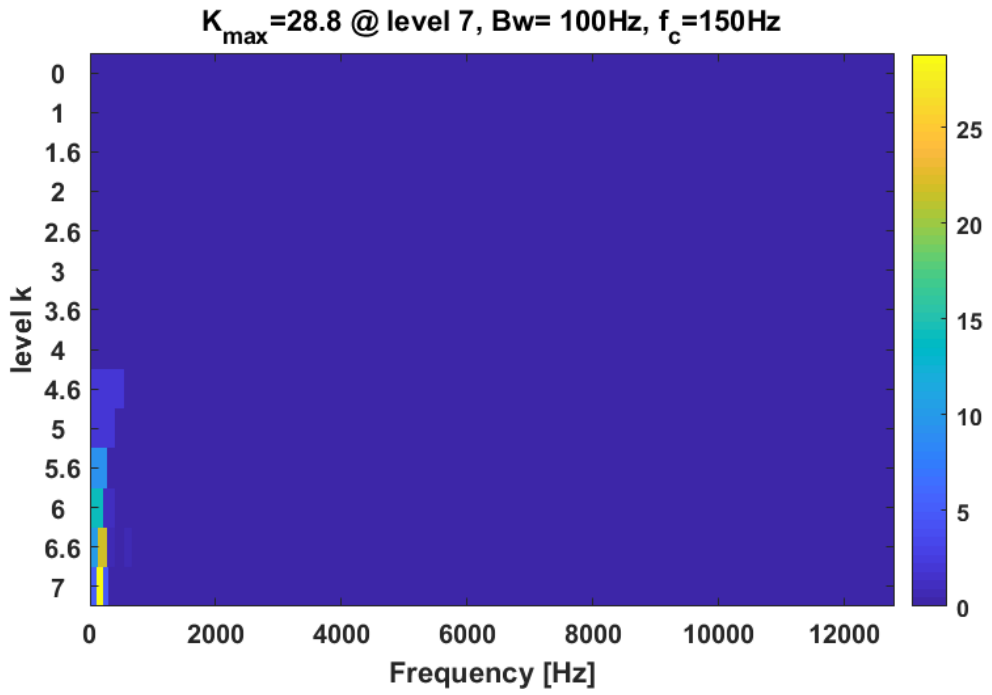

(a) Kurtogram of SANC processed data

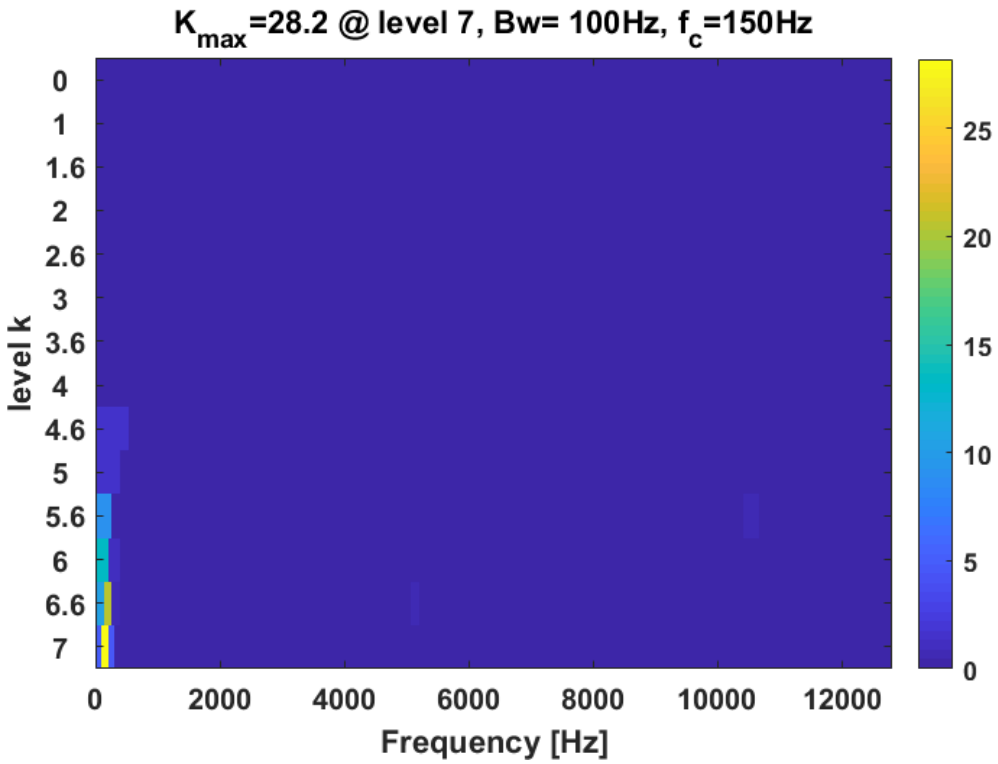

(b) Kurtogram of original data

Figure 4.18: Demonstration of Kurtogram results, 14000 rpm, minor fault condition

Therefore, it is necessary to perform a manual investigation on the possible high frequency resonances, where the bearing signals were amplified in envelope by the structural resonance during the tests. Also, the gear mesh related frequency resonances must be avoided to mitigate the influences from gears. From what has been demonstrated in Figure 4.16, similarly to Figure 2.11, resonance above 10000 Hz is a prominent candidate, as it has no strong correlations with the other gear mesh frequencies, and it is not induced by the accelerometers' self-resonance frequency (above 30 kHz, see Appendix A). The frequency amplitude spectral of data from minor and major fault conditions are produced after the SANC separation, shown in Figure 4.19 and Figure 4.20.

In Figure 4.19 and Figure 4.20, it is demonstrated that the resonances have been identified with central frequency. The same analysis has been conducted for healthy condition to extract the bearing associated resonances for comparisons. The selected centre frequencies and the bandwidth for demodulation are listed in the Table 4.2.

Table 4.2: Centre frequency and bandwidth for envelope analysis, 14000 rpm, 100 kW

Conditions	Centre Frequency [Hz]	Bandwidth [Hz]
Healthy	10754.7	1000
Minor Fault	10798.5	1000
Major Fault	10819.1	1000

With the centre frequencies and bandwidth for demodulation selected, the envelope spectra for health, minor fault and major fault condition are produced in Figure 4.21. It has been presented that, for healthy condition, the 2.68 Hz drive frequency from the 2^{nd} epicyclic carrier is distinct, as well as the 24 Hz modulation frequency from the nine planetary gears. However, the fault frequency BPFO around 60 Hz cannot be found. The same is true for the fault related sidebands.

For minor fault condition, the BPFO has been evidently revealed in Figure 4.22, comparing with the FFT analysis result shown in Figure 4.11, where no BPFO can be found. This result indicates that envelope analysis is effective in extracting the hidden bearing signatures preserved in the waveform.

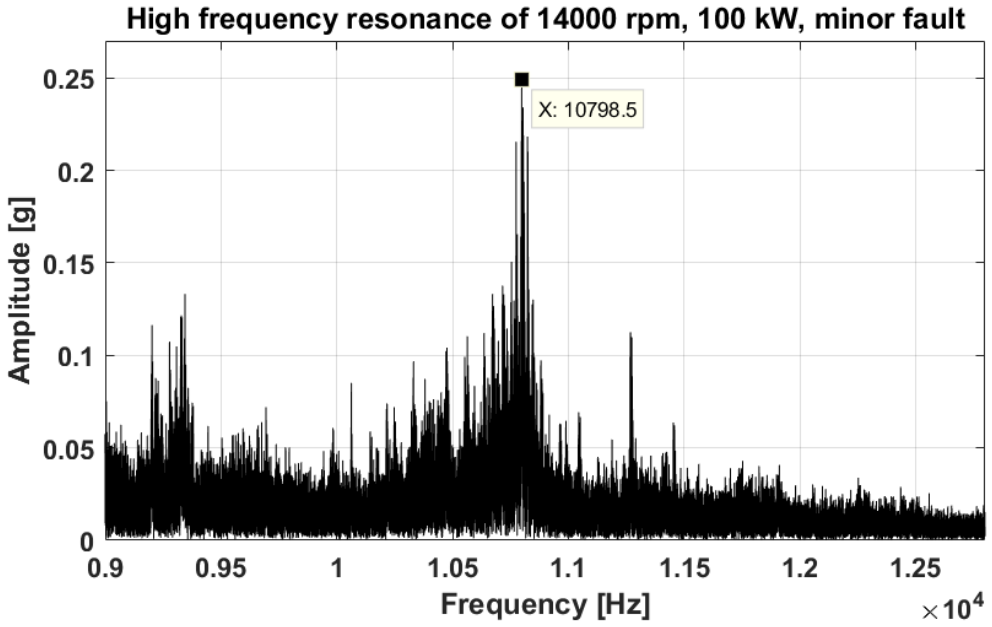

Figure 4.19: Resonance frequency, 14000 rpm, minor fault condition

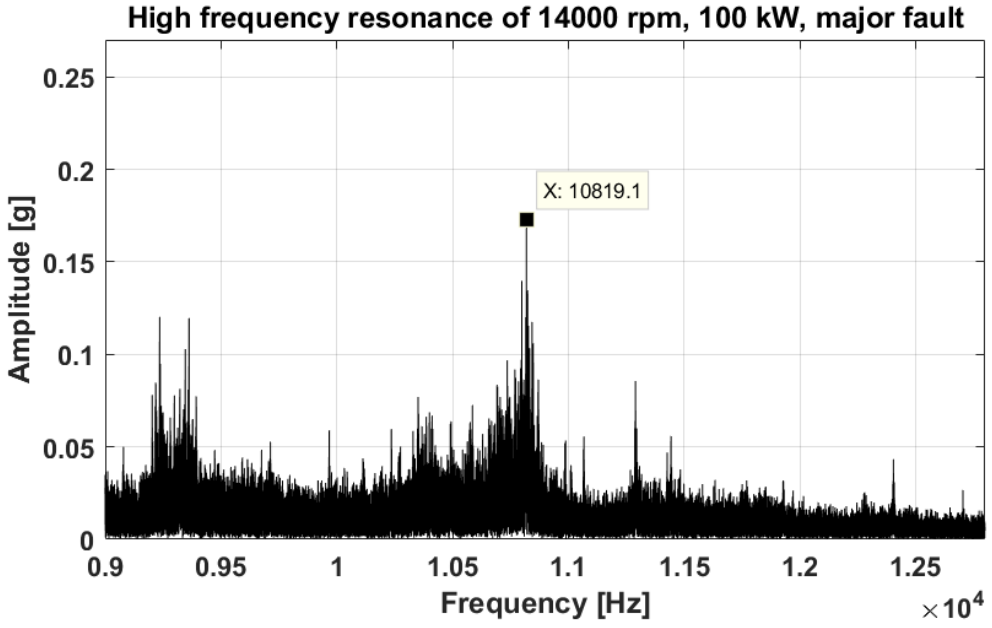

Figure 4.20: Resonance frequency, 14000 rpm, major fault condition

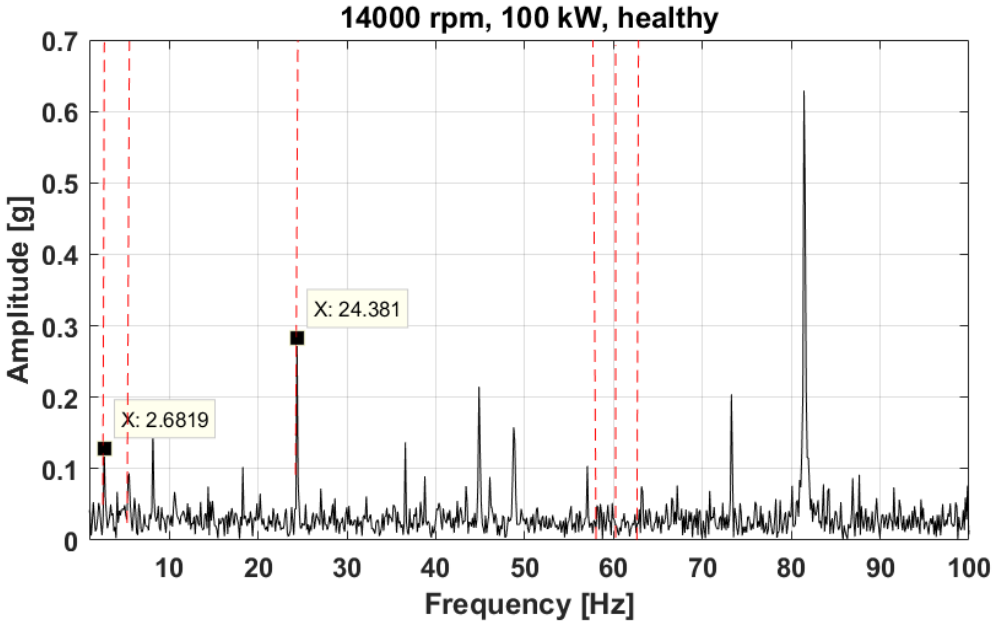

Figure 4.21: Envelope spectrum of 14000 rpm, 100 kW, healthy condition

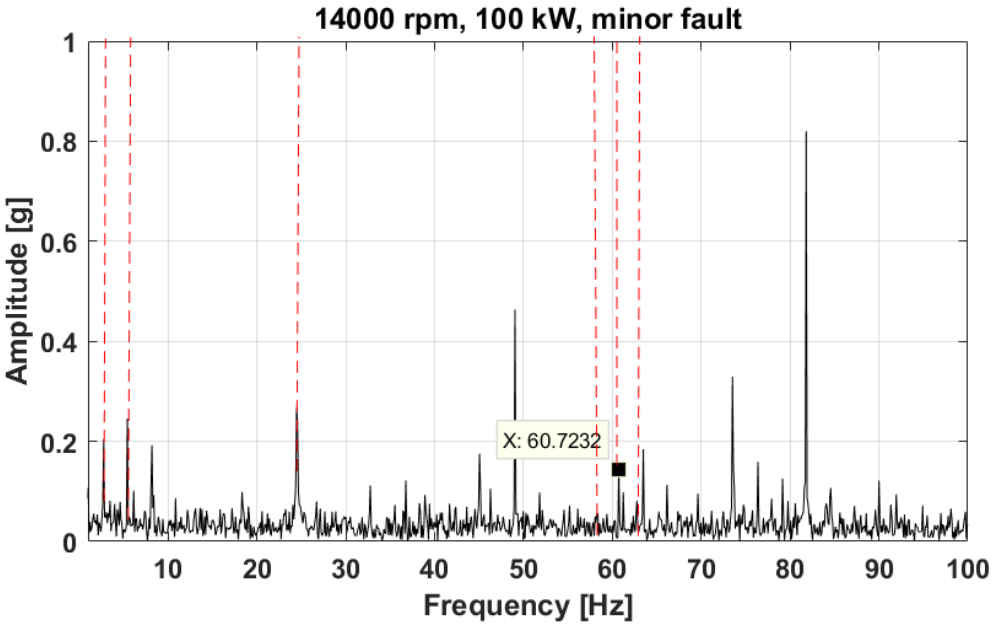

Figure 4.22: Envelope spectrum of 14000 rpm, 100 kW, minor fault condition

For major fault condition, the BPFO is not distinctly shown in Figure 4.23. The sideband of 62.9 Hz is resulted from 2.7 Hz planetary carrier plate modulation as previously explained. It is also evident that, the frequencies in integer multiplies of 2.7 Hz are much more intensely spread across the spectrum, due to the seeded major defect. Comparing with the FFT analysis result shown in Figure 4.12, this outcome is reduced in

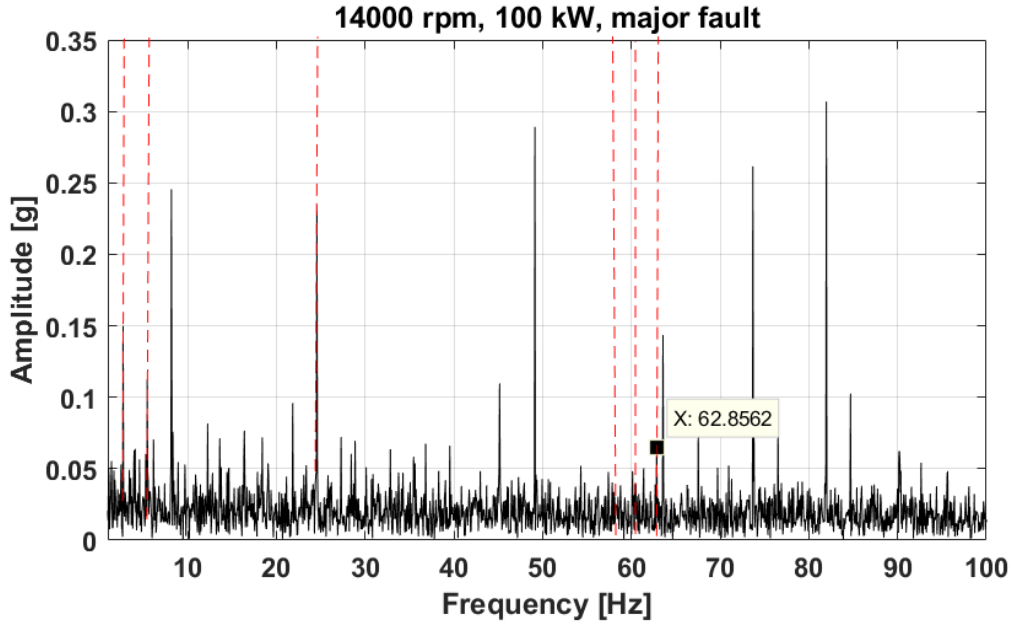

Figure 4.23: Envelope spectrum of 14000 rpm, 100 kW, major fault condition

effectiveness of identifying the fault associated signatures. This is likely to be caused by the wide demodulation bandwidth selected, hence allowing more gear-related frequencies to remain unfiltered. To further investigate on producing results that are more accurate, the bandwidth has been modified to 300 Hz to mitigate the interferences from gear signal, and the results are presented in Figure 4.24. It is evident that, in Figure 4.24(b), the BPFO and corresponding 62 Hz sideband are more obvious comparing with those shown in Figure 4.24(a). This concludes that, for major fault condition, it could be beneficial to select a narrower filtering bandwidth for clearer fault frequency identification.

With the processing routine of utilising signal separation combined with carefully select demodulation centre frequency and bandwidth, the results shown in Figure 4.22 and Figure 4.24(b) have successfully extracted the faulty bearing associated frequencies, including BPFO and sidebands, for both minor fault and major fault conditions. To further enhance the fault related frequencies, the squared envelope analysis was performed for each condition, with a new centre frequency and bandwidth listed in Table 4.3. Using a squared envelope spectrum rather than amplitude spectrum has been recommended in many researches [3, 18, 45, 59], typically for bearing fault diagnosis.

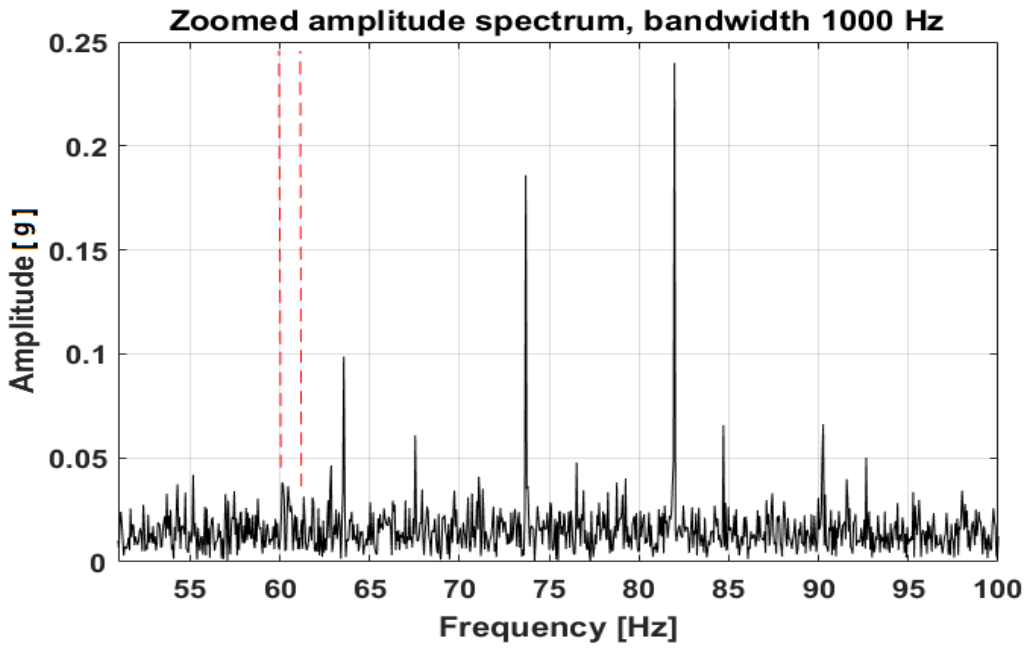

(a) Envelope spectrum with 1000 Hz bandwidth

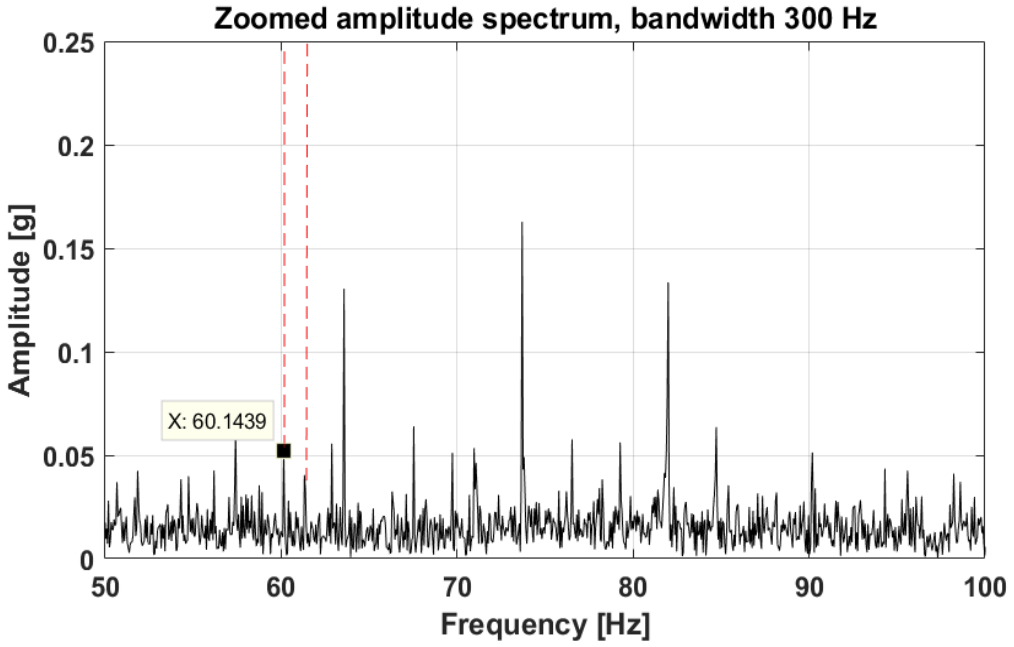

(b) Envelope spectrum with 300 Hz bandwidth

Figure 4.24: Demonstration of the effect of demodulation bandwidth

Table 4.3: Modified parameters envelope analysis, 14000 rpm, 100 kW

Conditions	Centre Frequency [Hz]	Bandwidth [Hz]	Delay d
Healthy	10754.7	300	850
Minor Fault	10797.8	300	850
Major Fault	10819.1	300	850

Additionally, in order to reduce the noise, a smaller delay, which is 850 has been implemented. The smaller delay is also determined by choosing a narrower bandwidth, which affects the calculation in Equation 4.11.

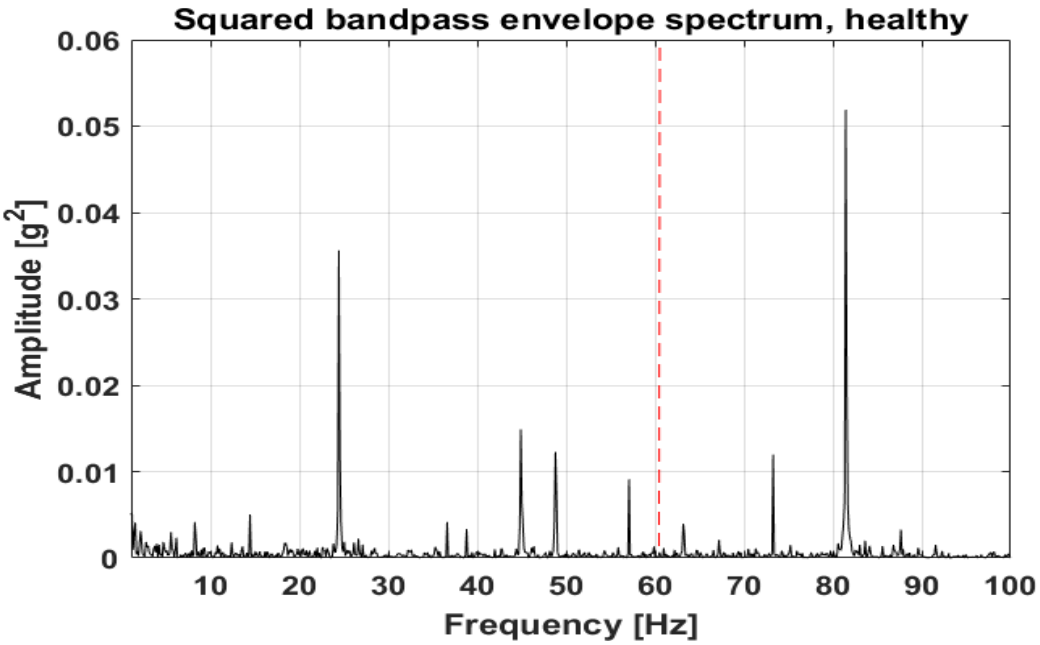

Figure 4.25: Squared envelope spectrum of 14000 rpm, 100 kW healthy data using updated filtering parameters

It can be concluded from the squared envelope spectra shown from Figure 4.25 to Figure 4.27 that, no evidence of BPFO is found in healthy condition, whereas in minor fault condition shown in Figure 4.26, a prominent increase in the BPFO is discovered comparing with the result prior processing in Figure 4.11. The BPFO is also evident in major fault condition shown in Figure 4.27. This discovery supports that the incipient planetary bearing outer race defects can be identified in the operational condition similar to helicopter being idle on the ground, using advanced frequency domain signal processing techniques.

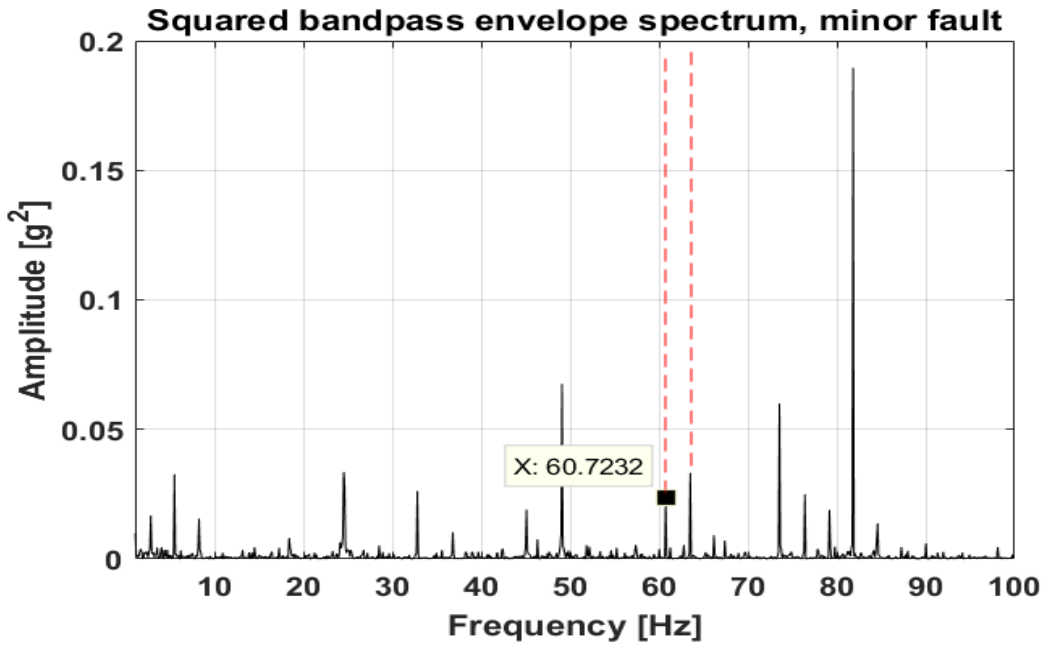

Figure 4.26: Squared envelope spectrum of 14000 rpm, 100 kW minor fault data using updated filtering parameters

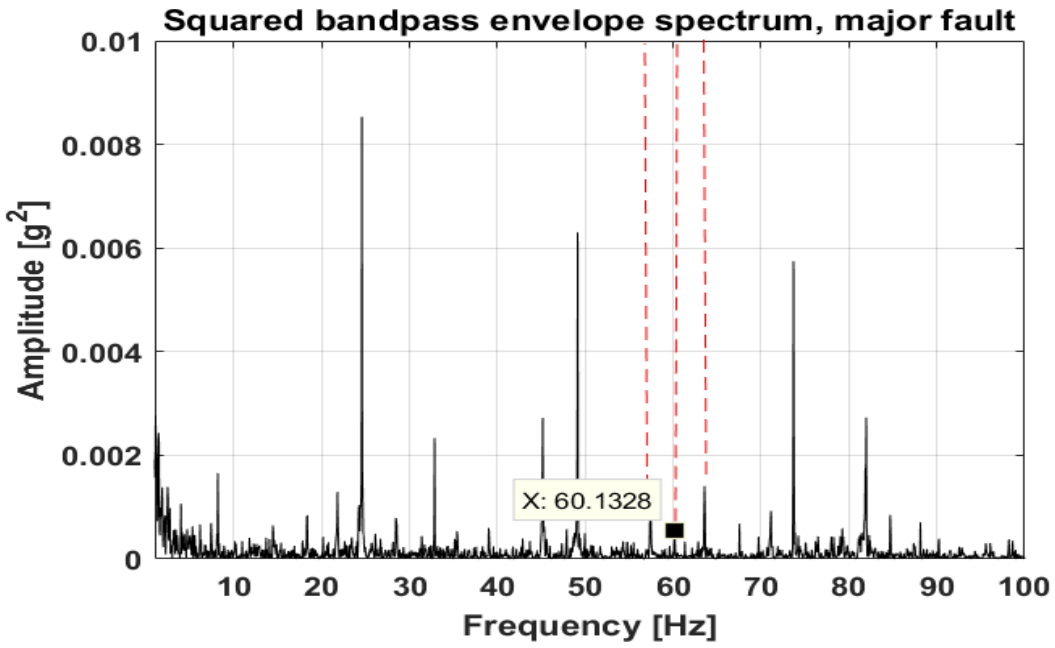

Figure 4.27: Squared envelope spectrum of 14000 rpm, 100 kW major fault data using updated filtering parameters

However, as demonstrated, this routine involves optimisations steps to be effective. It requires one to have certain prior knowledge, such as the selection of centre frequency and bandwidth. Thus, a more automatic and computationally efficient algorithm, namely

the IEC, was applied and validated.

As explained in Chapter 2, IEC essentially computes the envelope iteratively until the certain threshold $0 \leqslant \eta \leqslant 1$ is satisfied. To investigate IEC's effectiveness, firstly performed was the IEC using a recommended $\eta = 0.85$, without gear/bearing signal separations on faulty data, collected under 14000 rpm, 100 kW condition. It can be observed from the Figure 4.28 that, the IEC processing without signal separation for minor fault condition has achieved comparable outcome in Figure 4.28(a), where the BPFO and sidebands are observed directly. However, in major fault condition in Figure 4.28(b), the fault related frequencies cannot be observed other than the 57 Hz sideband.

To improve the capability of IEC, the separation results from SANC are high-passed at 8500 Hz to reduce the effect of overwhelming gear meshes slower than 8500 Hz, then adopted as input for IEC. With a more generous $\eta = 0.7$ selected to allow less suppression on bearing signals, the results are produced in Figure 4.29.

It is revealed in Figure 4.29 that, the results are improved both in minor and major fault conditions, where the BPFO and the fault related sidebands are distinctly shown, comparing with the results in Figure 4.24. This concludes that IEC is applicable as an alternative technique to the traditional envelope analysis. Additionally, the inherent iterative process does not demand the selection of optimal centre frequency and bandwidth for demodulation. As discussed above, with a high-pass filter that remove the frequency contents below the highest gear mesh frequencies will result in similar diagnostic results as shown in Figure 4.27.

4.4.2 Diagnosis on Vibration Data Collected at 14000 rpm, 180 kW Condition

From this section onwards, the diagnosis of vibration data collected under 14000 rpm, and 180 kW condition is presented. Since it has already been explained in detail in the processing of 100 kW condition, the gear mesh frequency components in amplitude spectrum will not be elaborated. Similar diagnosis steps are performed based on the conclusions from 100 kW condition. Two routines are performed:

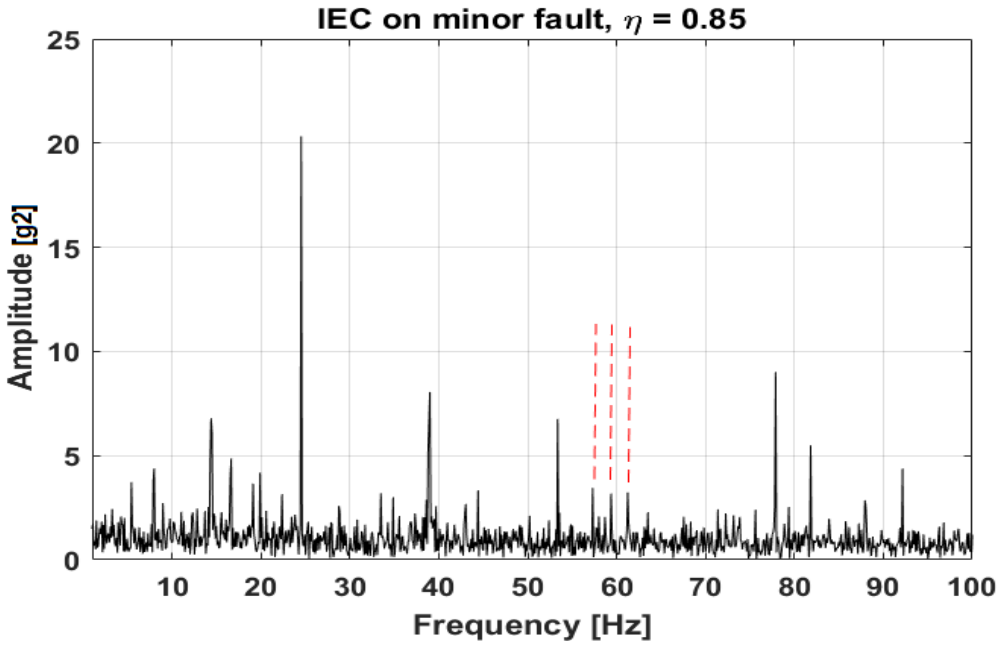

(a) IEC on minor fault, $\eta = 0.85$

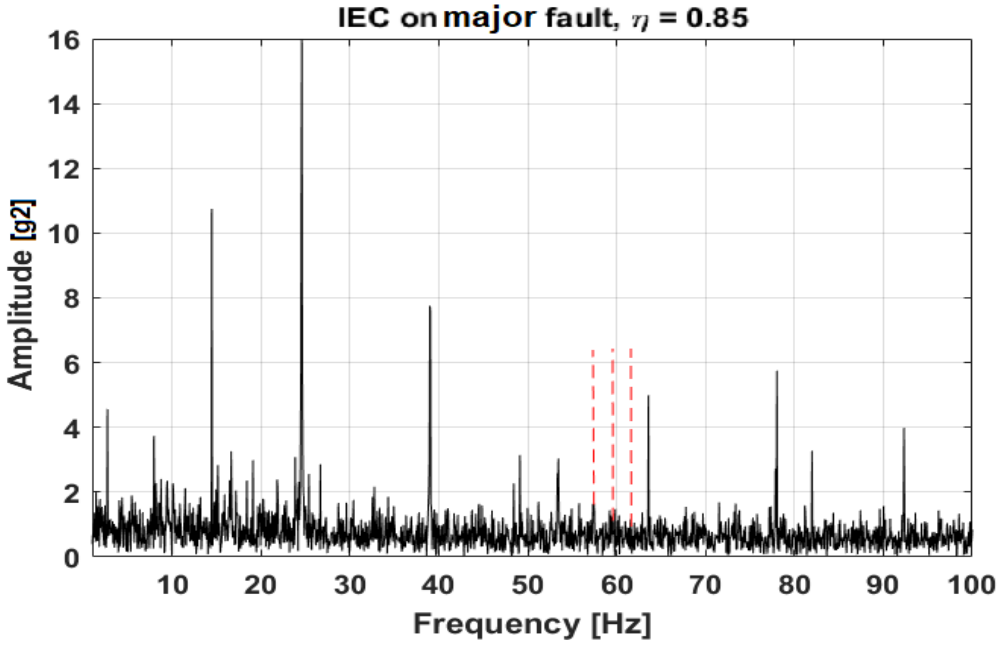

(b) IEC on major fault, $\eta = 0.85$

Figure 4.28: Direct IEC squared envelope spectrum on 14000 rpm, 100 kW data

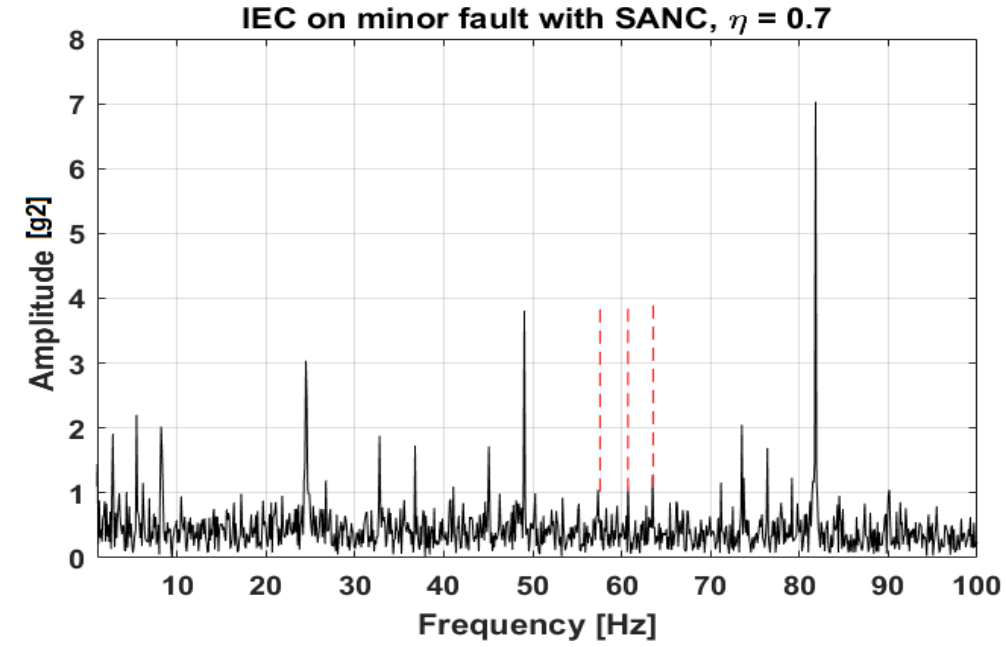

(a) IEC on minor fault with SANC, $\eta = 0.7$

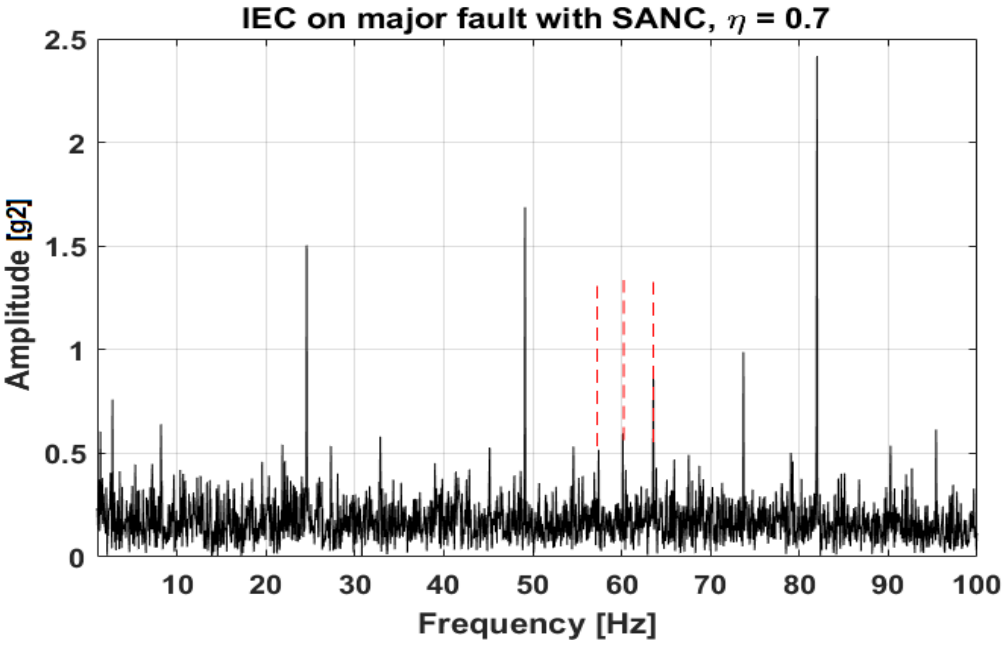

(b) IEC on major fault with SANC, $\eta = 0.7$

Figure 4.29: Demonstration of the IEC squared envelope spectrum after signal separation

1. Perform signal separation technique, then investigate on high-passed IEC analysis to make use of its fast computation.
2. Perform signal separation technique, then select optimal demodulation centre frequency and its bandwidth for squared envelope analysis.

The relevant diagnostic information for 14000 rpm, 180 kW condition is summarised in Table 4.4.

Table 4.4: Diagnostic parameters of 14000 rpm, 180 kW condition

Conditions	Load	Speed	F_{sampling}	BPFO	ω_{c1}	ω_{c2}
Healthy	180 kW	14034 rpm	25600 Hz	N/A	7.90 Hz	2.71 Hz
Minor Fault	180 kW	14088 rpm	25600 Hz	59.67 Hz	7.93 Hz	2.72 Hz
Major Fault	180 kW	16110 rpm	25600 Hz	59.77 Hz	7.95 Hz	2.73 Hz

Firstly, the zoomed amplitude spectra are plotted in Figure 4.30, Figure 4.31 and Figure 4.32. It is noticeable that there are no BPFO or sidebands found in healthy condition. In minor fault condition, the fault related sidebands, namely 57 Hz and 62.7 Hz are obvious.

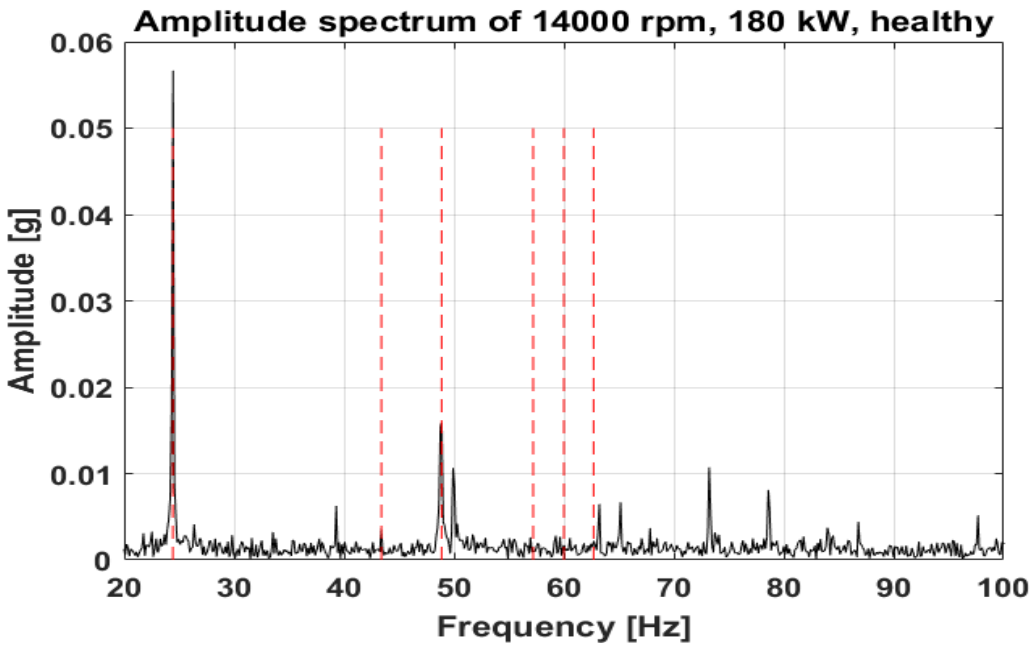

Figure 4.30: Zoomed amplitude spectrum, 14000 rpm, 180 kW, healthy condition

Similarly, as discussed in 14000 rpm, 100 kW condition, the fast bandpassed IEC was

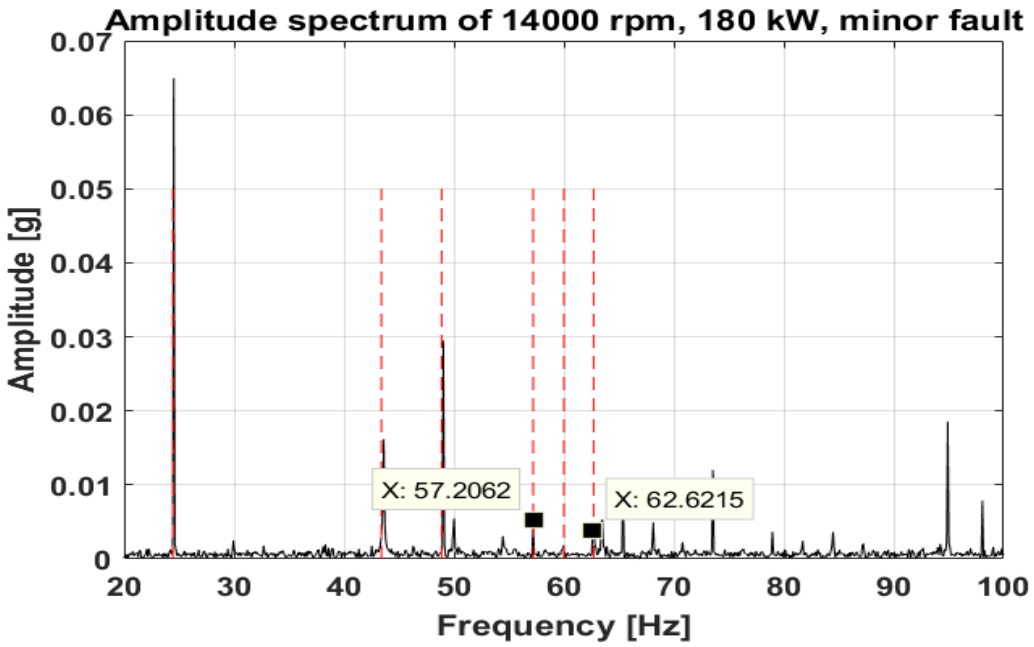

Figure 4.31: Zoomed amplitude spectrum, 14000 rpm, 180 kW, minor fault condition

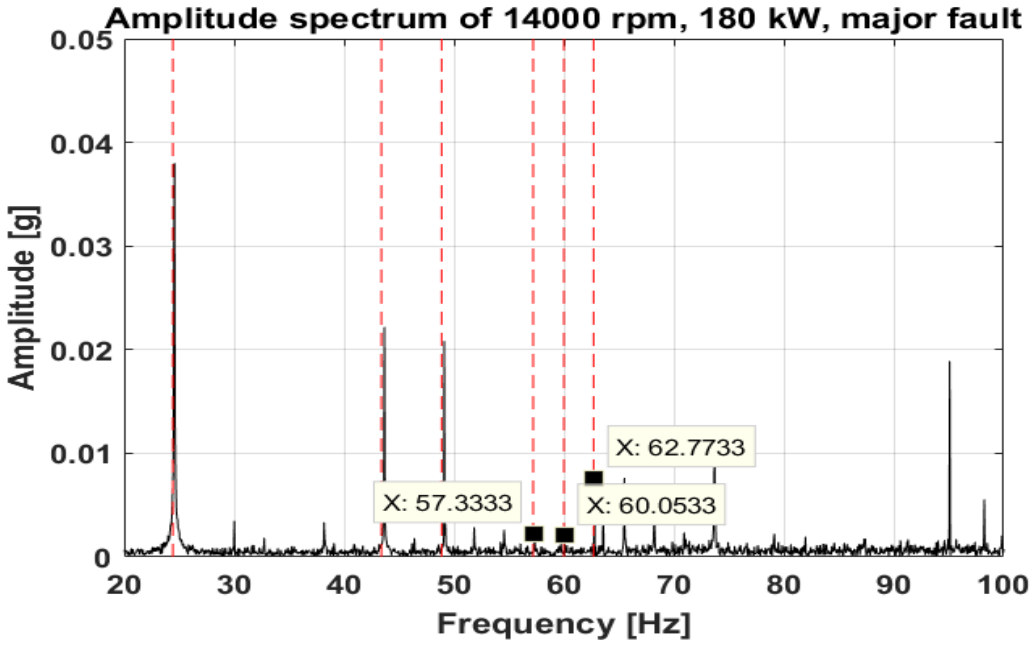

Figure 4.32: Zoomed amplitude spectrum, 14000 rpm, 180 kW, major fault condition

performed after the SANC analysis, with a 8500 Hz high-pass filter and $\eta = 0.7$ applied. However, the results are not successful. The major fault processed with IEC after SANC is presented in Figure 4.33 for discussion.

It is evidently shown in Figure 4.33 that, although the frequency at 63.59 Hz could indicate

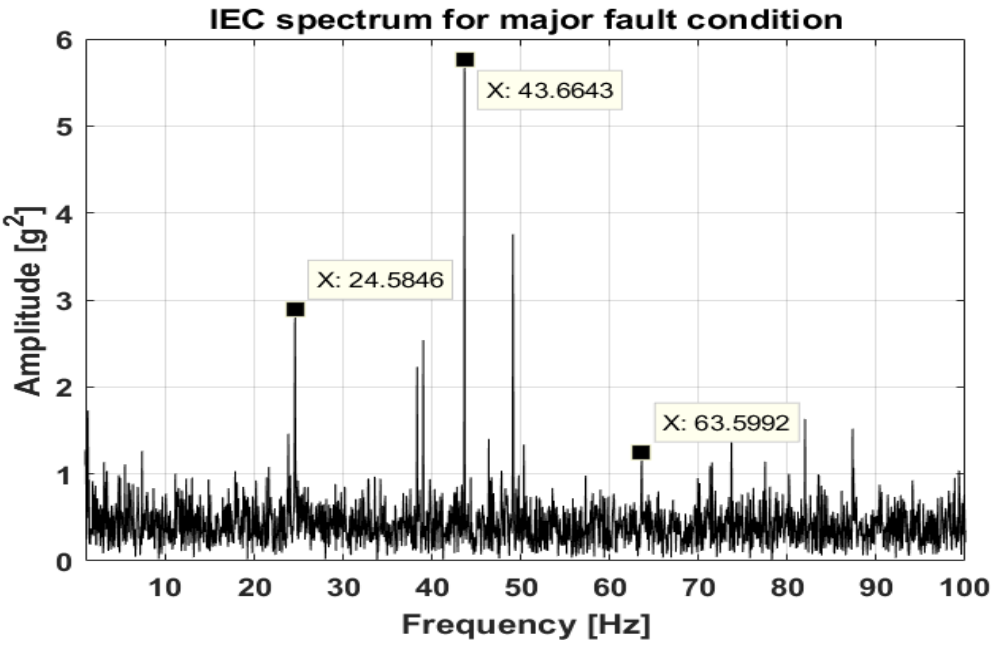

Figure 4.33: Unsuccessful IEC analysis on 14000 rpm, 180 kW major fault data

the existence of fault related sideband frequency, there lacks support to identify BPFO. Therefore, IEC has failed in diagnosing 14000 rpm, 180 kW condition. The envelope analysis which looks into the exact frequency demodulation will be performed to diagnose this condition.

The amplitude spectra are zoomed to the range of [9000 Hz, 12800 Hz] for the localising the resonances. The resonances in three conditions are shown from Figure 4.34 to Figure 4.36. The resonances centre frequencies and the bandwidths are selected following similar procedures in 100 kW condition, and are recorded in Table 4.5. It is noted that the demodulation bandwidth for 180 kW condition has been selected to be 200 Hz, narrower that the 300 Hz in 100 kW condition. This is based on the consideration that under higher load condition, the inherently overwhelming gear mesh frequencies were more amplified, hence a more rigid demodulation to mitigate the interferences are beneficial to enhance the overall diagnosis.

With the centre frequency and bandwidth determined, the squared envelope analysis was performed. The results are shown in Figure 4.37, Figure 4.38 and Figure 4.39. It is conclusive that, similar to 100 kW condition, the BPFO is identified in minor fault condition shown in Figure 4.38, while no evidence of BPFO is shown in healthy

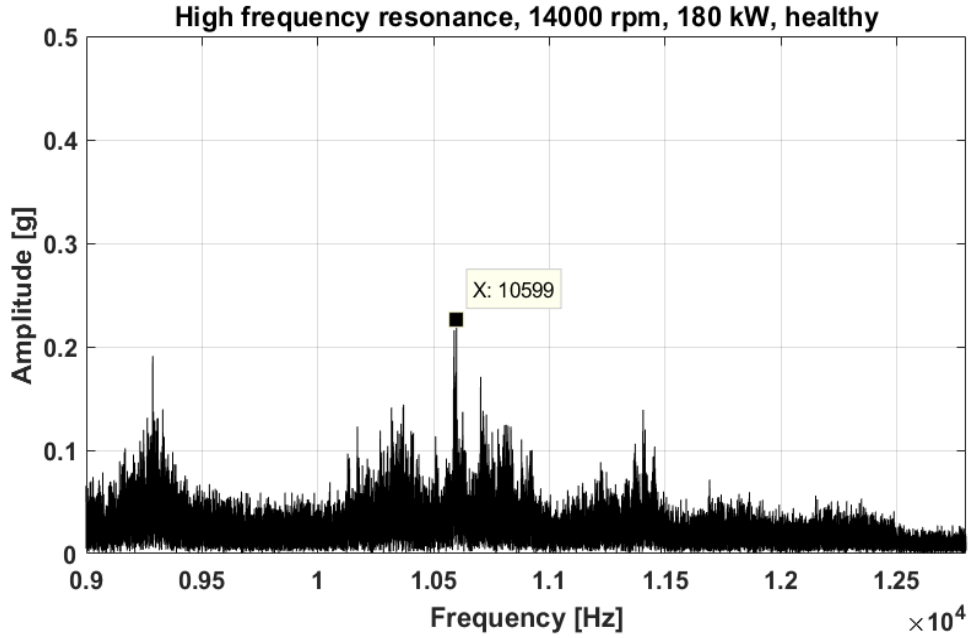

Figure 4.34: Resonance frequencies, 14000 rpm, 180 kW, healthy

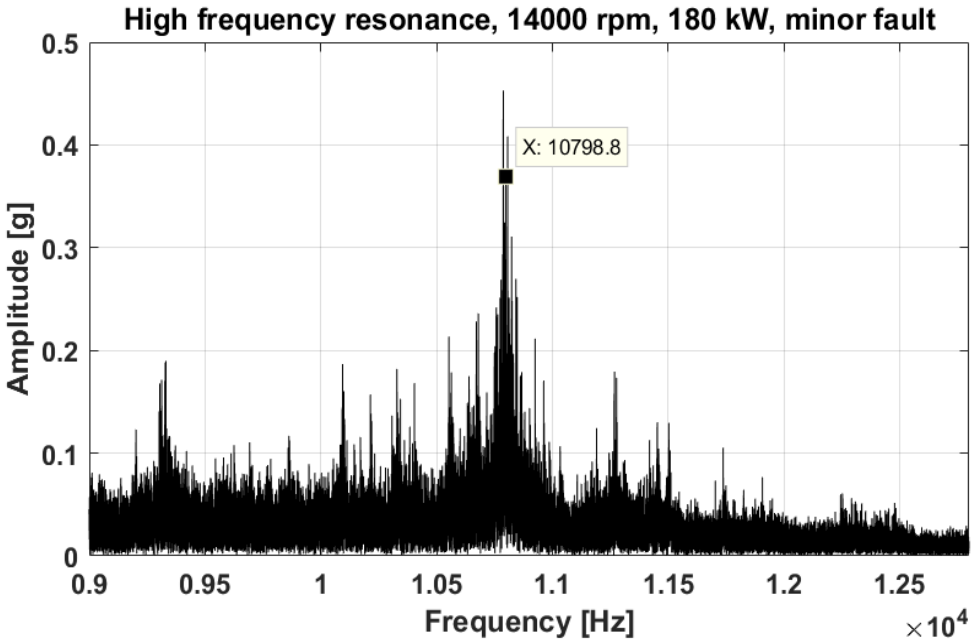

Figure 4.35: Resonance frequencies, 14000 rpm, 180 kW, minor fault

condition. Additionally, fault related sideband 63.45 Hz has also been found in Figure 4.38, supporting the diagnosis conclusion.

In major fault condition result shown in Figure 4.39, the fault related sideband 57.40 Hz is quite distinct, however, the BPFO is barely visible. This is related to the interferences

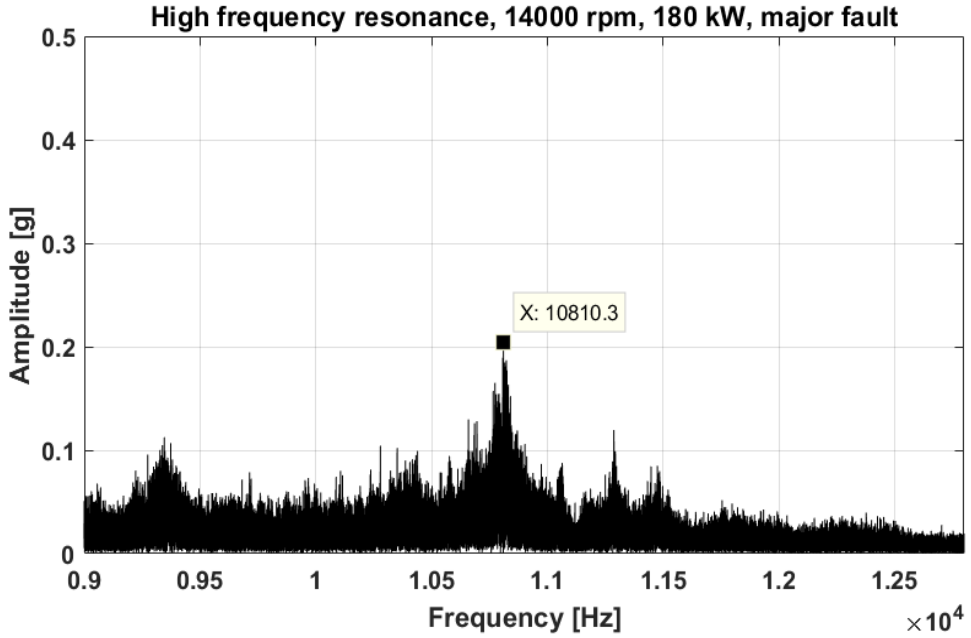

Figure 4.36: Resonance frequencies, 14000 rpm, 180 kW, major fault

Table 4.5: Centre frequency and bandwidth for envelope analysis, 14000 rpm, 180 kW

Conditions	Centre Frequency [Hz]	Bandwidth [Hz]
Healthy	10599	200
Minor Fault	10798.8	200
Major Fault	10810.3	200

from the reinforced gear mesh frequencies and the 1^{st} and 2^{nd} carrier plates amplitude modulations. To specifically investigate on the major fault diagnosis case, the Cepstrum analysis is applied to suppress the gear mesh frequencies. The introduction of Cepstrum analysis has been stated in Section 2.4.2.

Considering the capability of Cepstrum editing in terms of suppressing the fundamental and harmonics frequencies, in this study, a short-pass lifter was applied on major fault data. Short-pass indicates that the purpose of Cepstrum editing in this case was to reserve only the higher frequency resonances, which are more transient. The editing should take place before SANC separation, as recommended in [62, 116]. Based on the requirements of enhancing the frequencies below 65 Hz, a short-pass lifter was designed that, all quefrencies above 1/65 second is removed. This process is showcased in Figure

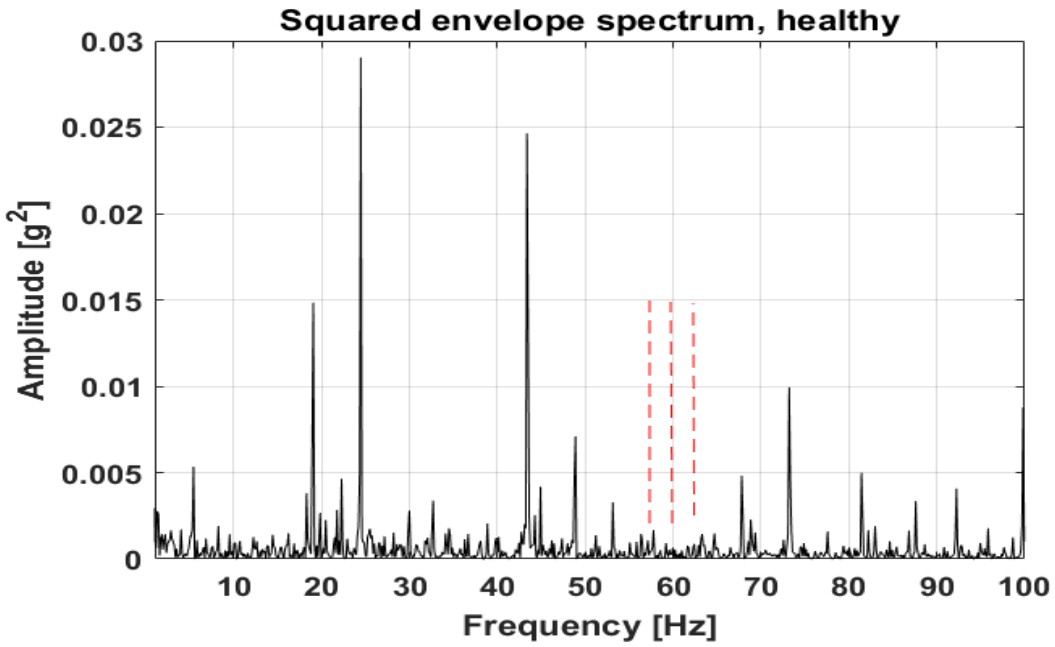

Figure 4.37: Squared envelope spectrum, 14000 rpm, 180 kW, healthy condition

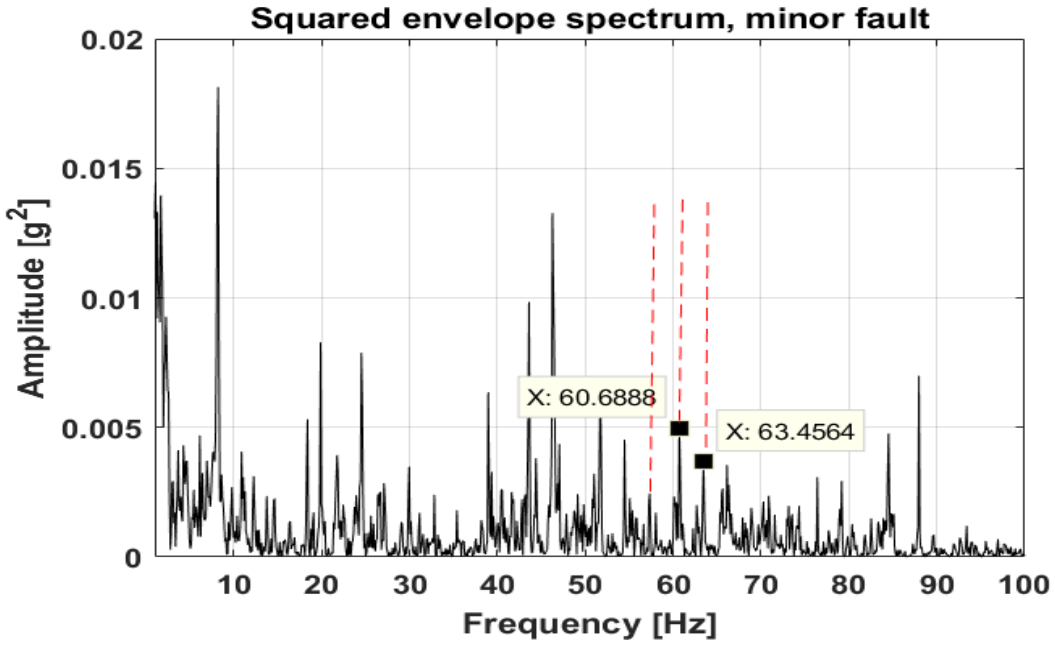

Figure 4.38: Squared envelope spectrum, 14000 rpm, 180 kW, minor fault condition

4.40.

After the Cepstrum editing was performed in Figure 4.40, the similar processing steps were performed. The processing result is demonstrated in Figure 4.41, which is produced with Cepstrum, SANC and squared bandpassed envelope analysis. It has been revealed in

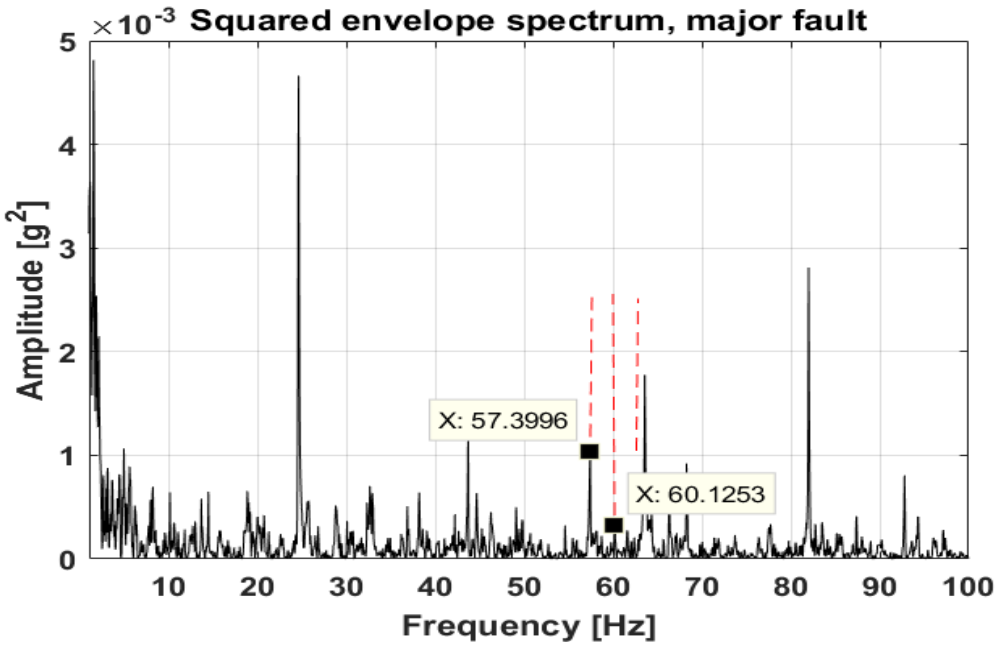

Figure 4.39: Squared envelope spectrum, 14000 rpm, 180 kW, major fault condition

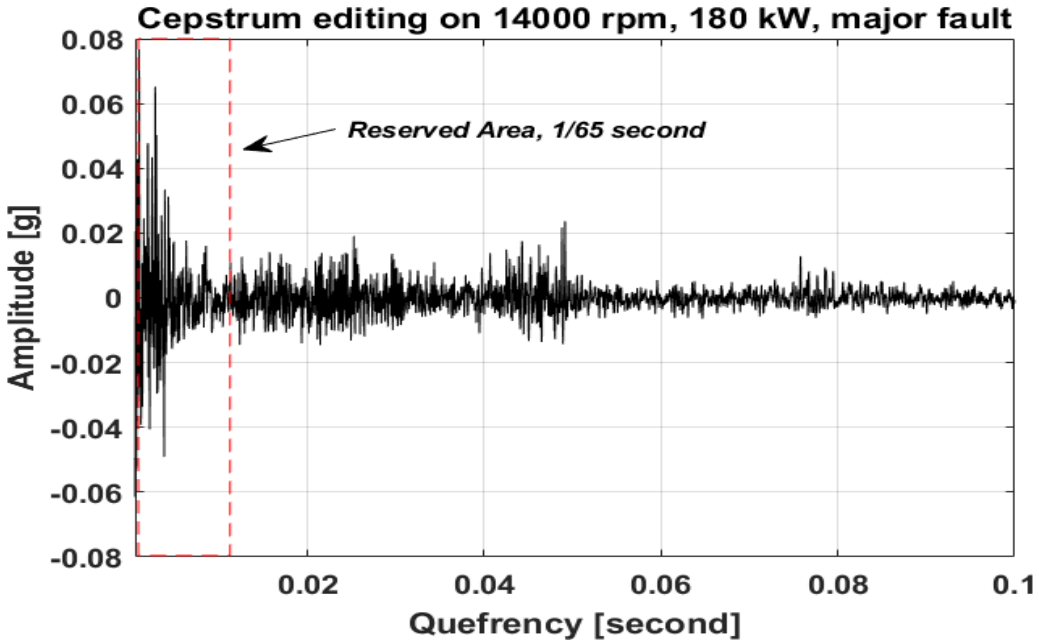

Figure 4.40: Cepstrum editing on major fault condition of 14000 rpm, 180 kW

Figure 4.41 that, the BPFO as well as the fault related sidebands have been successfully extracted, and the diagnosis for this condition is conclusive.

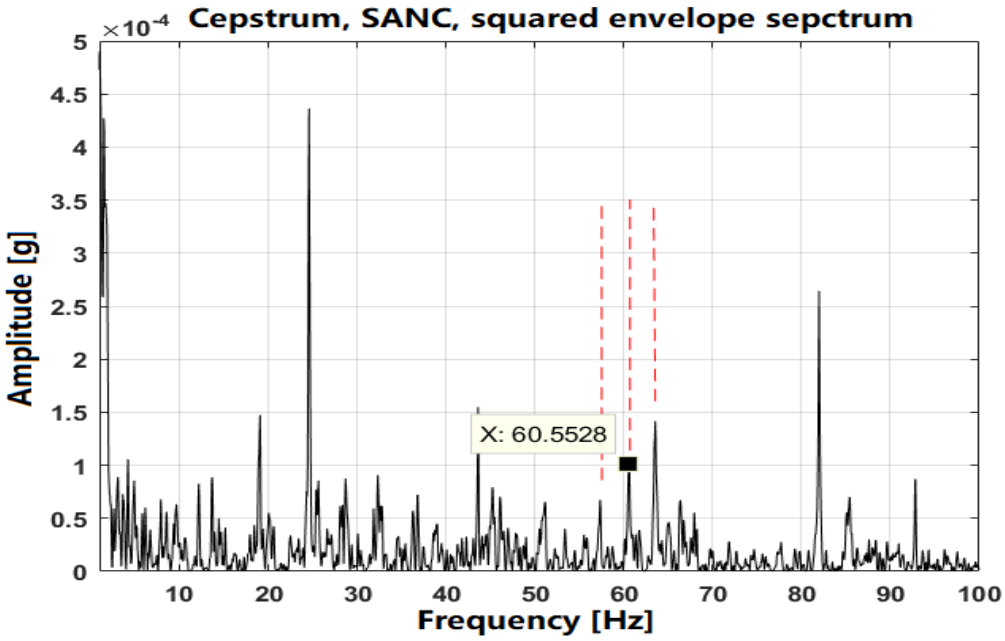

Figure 4.41: Optimised diagnosis on major fault condition of 14000 rpm, 180 kW

4.4.3 Diagnosis on Vibration Data Collected at 16000 rpm, 100 kW Condition

Table 4.6: Diagnostic parameters of 16000 rpm, 100 kW condition

Conditions	Load	Speed	F_{sampling}	BPFO	ω_{c1}	ω_{c2}
Healthy	100 kW	16038 rpm	25600 Hz	N/A	9.03 Hz	3.10 Hz
Minor Fault	100 kW	16074 rpm	25600 Hz	68.08 Hz	9.05 Hz	3.11 Hz
Major Fault	100 kW	16110 rpm	25600 Hz	68.24 Hz	9.07 Hz	3.12 Hz

The diagnostic parameters of 16000 rpm, 100 kW condition are presented in Table 4.6. The FFT spectrum for each health condition is plotted for inspection in Figure 4.42, Figure 4.43 and Figure 4.44, respectively.

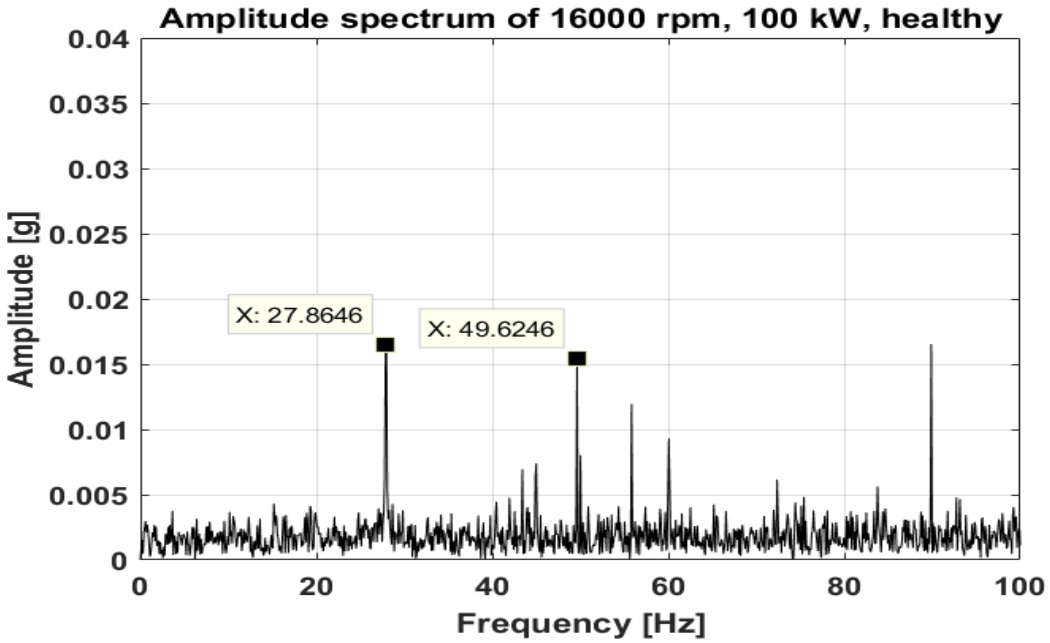

Figure 4.42: Zoomed amplitude spectrum, 16000 rpm, 100 kW healthy condition

It has clearly demonstrated that in healthy condition, there is no sign of BPFO or any sidebands shown in the spectrum in Figure 4.42. The 1^{st} and 2^{nd} epicyclic carrier induced frequencies, namely the 27.9 Hz and 49.7 Hz can be found in both healthy and faulty conditions spectrum, showing persistent modulation effects from the carrier gears. In Figure 4.43, the fault related sideband frequency 65.2 Hz ($BPFO - \omega_{c2}$) has been identified, while the BPFO and sidebands can be seen directly in major fault in Figure

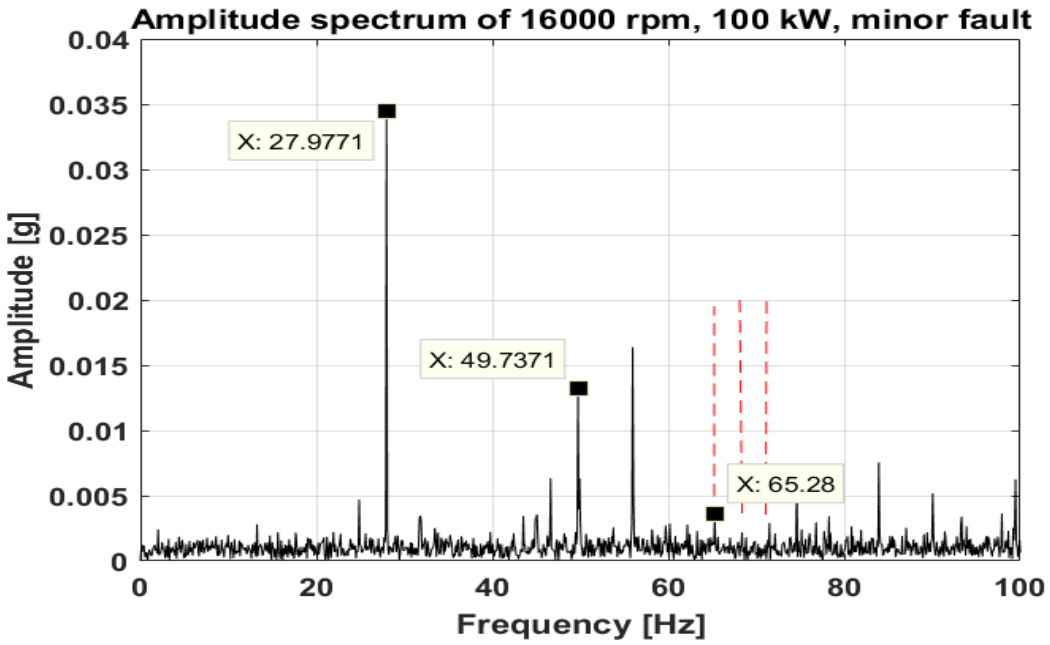

Figure 4.43: Zoomed amplitude spectrum, 16000 rpm, 100 kW minor fault condition

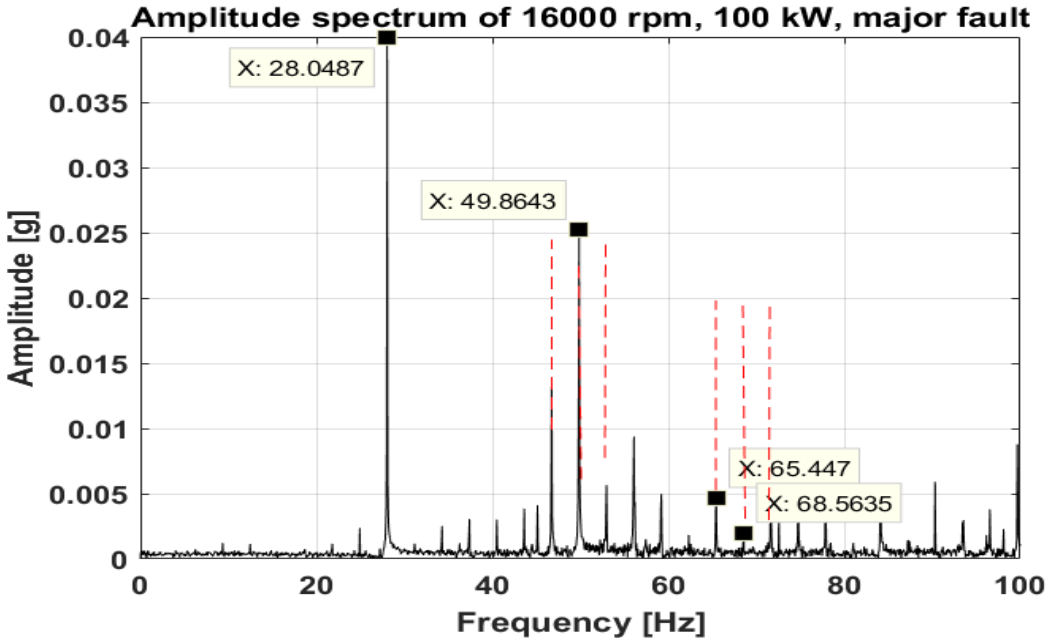

Figure 4.44: Zoomed amplitude spectrum, 16000 rpm, 100 kW major fault condition

4.44, indicating that the major fault has severe and more obvious impact on the spectrum of the vibration data.

It is worth-noticing that, in Figure 4.44, the 49.86 Hz frequency component has been modulated by the drive frequency ω_{c2}. As explained in detail in Section 4.4.1, the

frequency 49.86 Hz is a result from the 1^{st} sun gear modulated by 2^{nd} carrier gear speed. The modulations shown in the spectrum hence are the result of the increased impact from the major fault at 2^{nd} epicyclic module.

To reduce the interferences from the deterministic gear mesh frequencies, the SANC processing has been conducted, following similar procedures explained in 14000 rpm condition. The demodulation centre frequencies and corresponding bandwidths are then determined in Table 4.7.

Table 4.7: Centre frequency and bandwidth for envelope analysis, 16000 rpm, 100 kW

Conditions	Centre Frequency [Hz]	Bandwidth [Hz]
Healthy	9783	200
Minor Fault	9801	200
Major Fault	9826	200

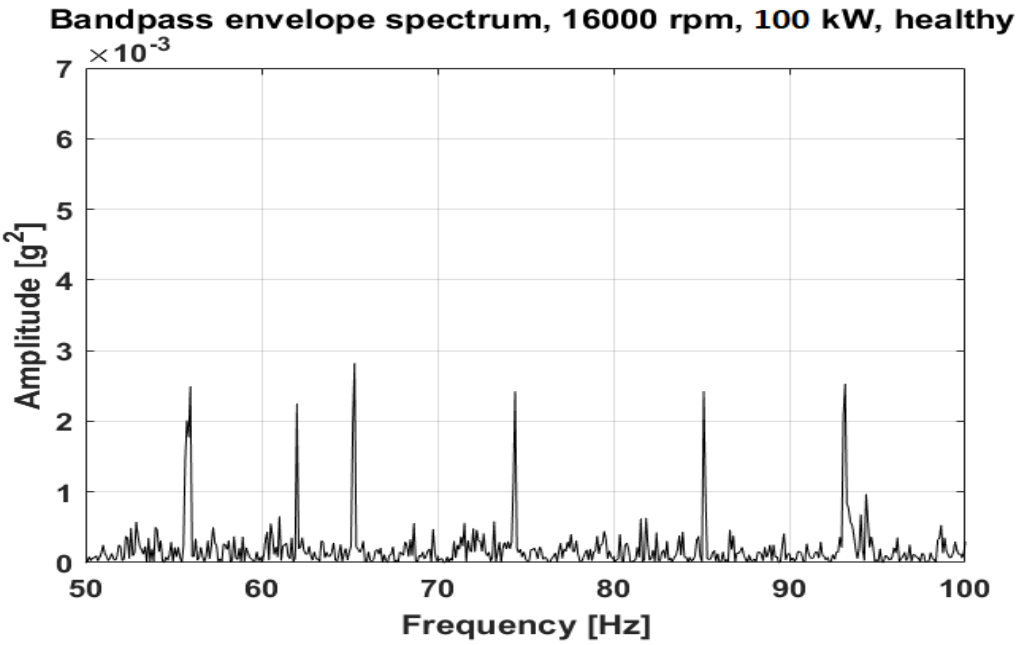

Figure 4.45: Squared envelope spectrum, 16000 rpm, 100 kW, healthy condition

The squared envelope spectrum of the bandpassed signal is plotted for each health conditions in Figure 4.45, Figure 4.46 and Figure 4.47. It can be concluded that, the major fault condition shows the most prominent diagnosis results, where the BPFO and fault associated frequency sidebands, namely 62.3 Hz, 71.7 Hz have been clearly

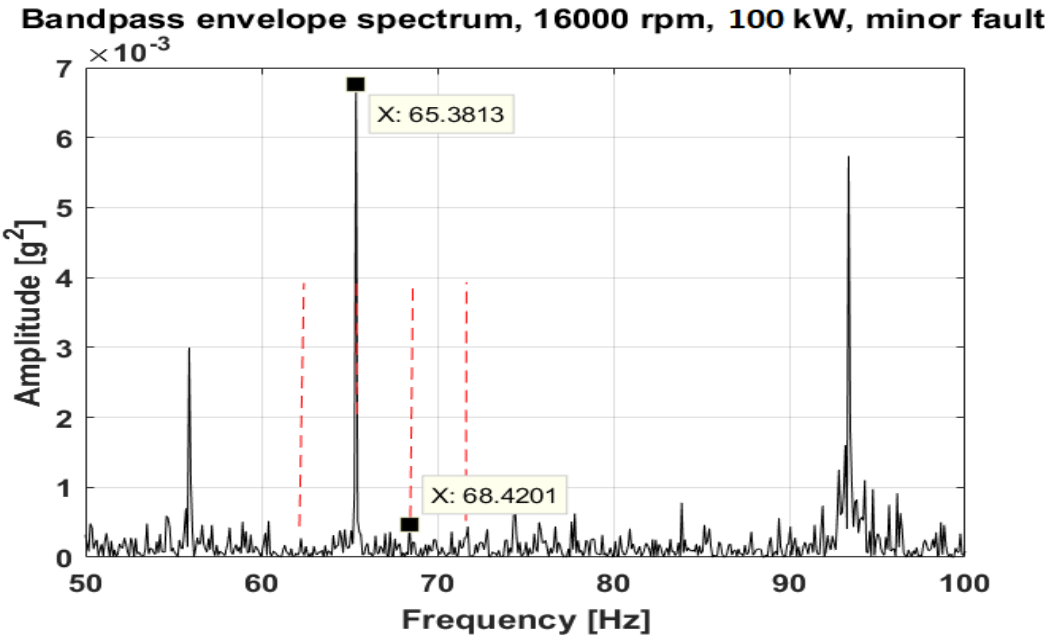

Figure 4.46: Squared envelope spectrum, 16000 rpm, 100 kW, minor fault condition

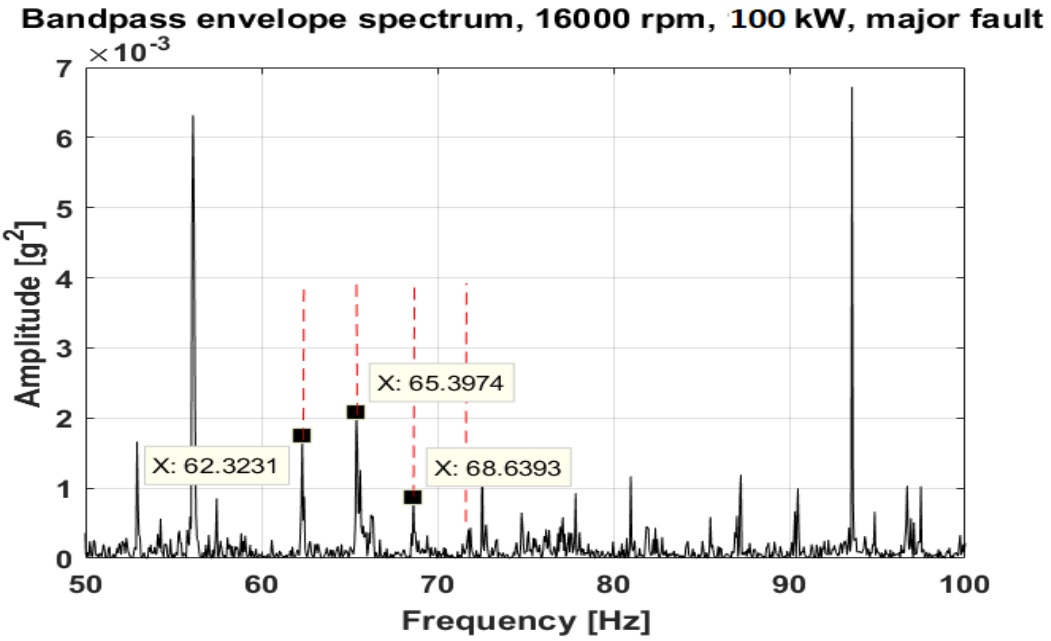

Figure 4.47: Squared envelope spectrum, 16000 rpm, 100 kW, major fault condition

extracted. In minor fault condition shown in Figure 4.46, while the BPFO has a low energy, the sideband frequency 65.38 Hz has dramatically increased. The outcomes of squared envelope analysis have conclude that the diagnosis of the planetary bearing fault is successful, using vibration data collected under 16000 rpm, 100 kW condition.

4.4.4 Diagnosis on Vibration Data Collected at 16000 rpm, 180 kW Condition

Table 4.8: Diagnostic parameters of 16000 rpm, 180 kW condition

Conditions	Load	Speed	F_{sampling}	BPFO	ω_{c1}	ω_{c2}
Healthy	100 kW	16044 rpm	25600 Hz	N/A	9.03 Hz	3.10 Hz
Minor Fault	180 kW	16074 rpm	25600 Hz	68.08 Hz	9.05 Hz	3.11 Hz
Major Fault	180 kW	16110 rpm	25600 Hz	68.24 Hz	9.07 Hz	3.12 Hz

The diagnostic parameters of 16000 rpm, 180 kW condition are presented in Table 4.8. Similar to 100 kW condition under 16000 rpm speed, the FFT spectrum for each health condition does not give a clear fault-related indication.

The spectrum for each health condition is plotted in Figure 4.48 to Figure 4.50. It is shown that the amplitude modulation associated with the 1^{st} epicyclic carrier speed at 72.25 Hz and 2^{nd} epicyclic carrier speed at 27.9 Hz are obvious in all three spectra. Notably, the 72.25 Hz is quite close to the sidebands frequency, which can be calculated as BPFO$+\omega_{c2} = 71.3\ Hz$. This frequency can be observed in Figure 4.50 major fault spectrum, increasing the difficulty in diagnosing faults with sidebands. In terms of the BPFO, no clear indication can be found in healthy or the major fault condition. Only in minor fault condition, the BPFO can be observed directly in spectrum, shown in Figure 4.49. The rest of the diagnosis is performed aiming to extract the BPFO in faulty conditions.

Following similar steps defined in 100 kW condition, the resonance frequencies that amplified the bearing signals are selected and reported in Table 4.9. Using these parameters, the squared envelope spectrum of the bandpassed signal is plotted for each health conditions in Figure 4.51, Figure 4.52 and Figure 4.53.

It is evidently shown in Figure 4.51 to Figure 4.53 that, after the bandpass filtering, BPFO remains unseen in Figure 4.51, but has been successfully extracted in both minor and major fault conditions shown in Figure 4.52 and Figure 4.53, respectively. Additionally, the sidebands are more revealing comparing with unprocessed raw FFT spectrum. At this

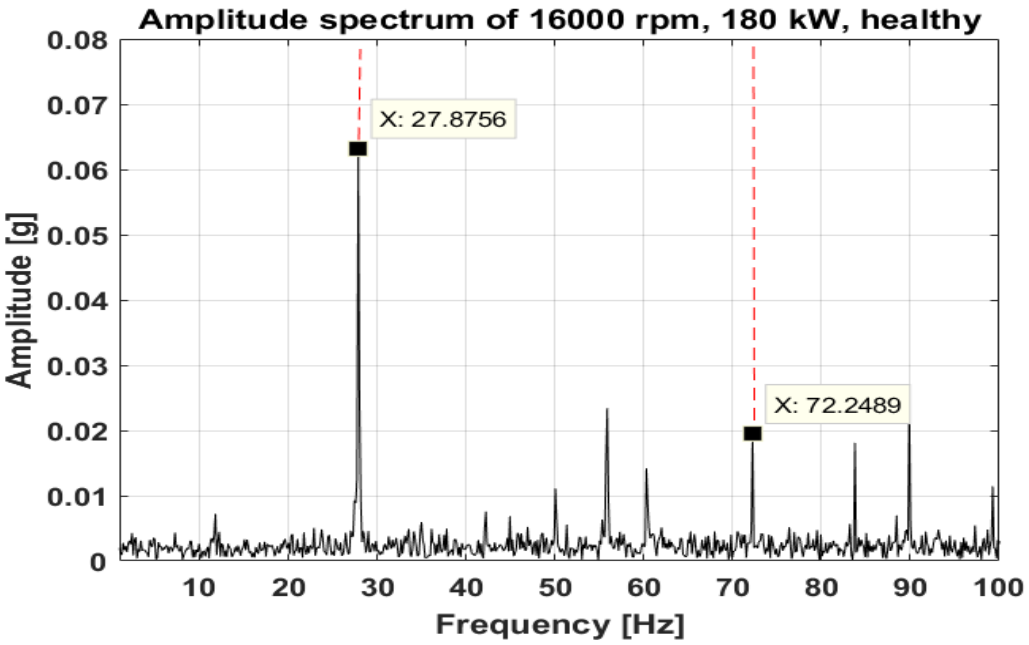

Figure 4.48: Zoomed amplitude spectrum, 16000 rpm, 180 kW healthy condition

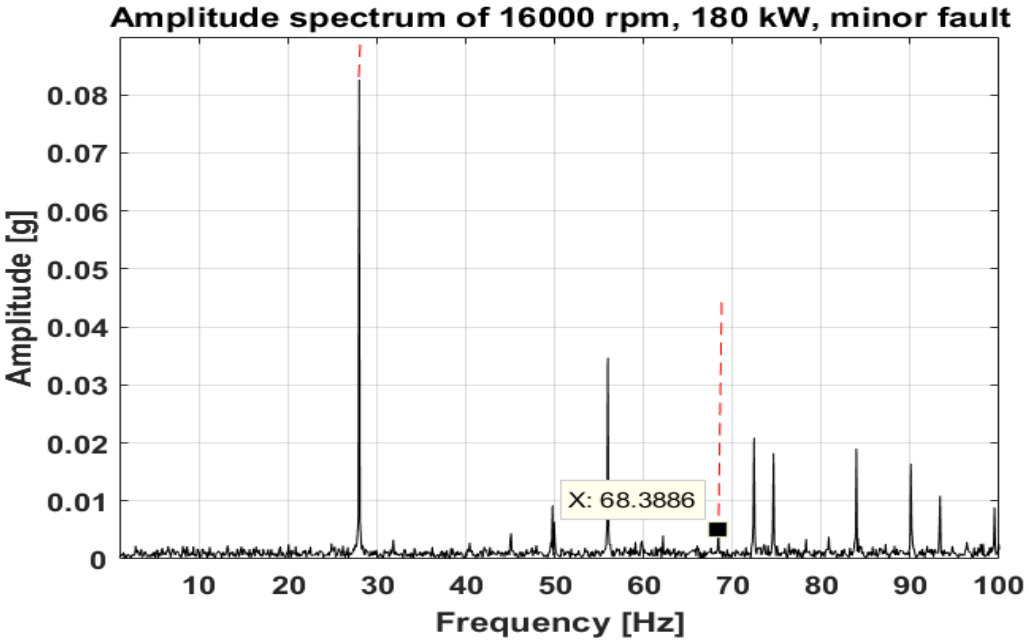

Figure 4.49: Zoomed amplitude spectrum, 16000 rpm, 180 kW minor fault condition

point, no further techniques are required to be employed to further enhance the BPFO, as the results in Figure 4.52 and Figure 4.53 have indicated a conclusive successful diagnosis for the planetary bearing outer race defects under this condition.

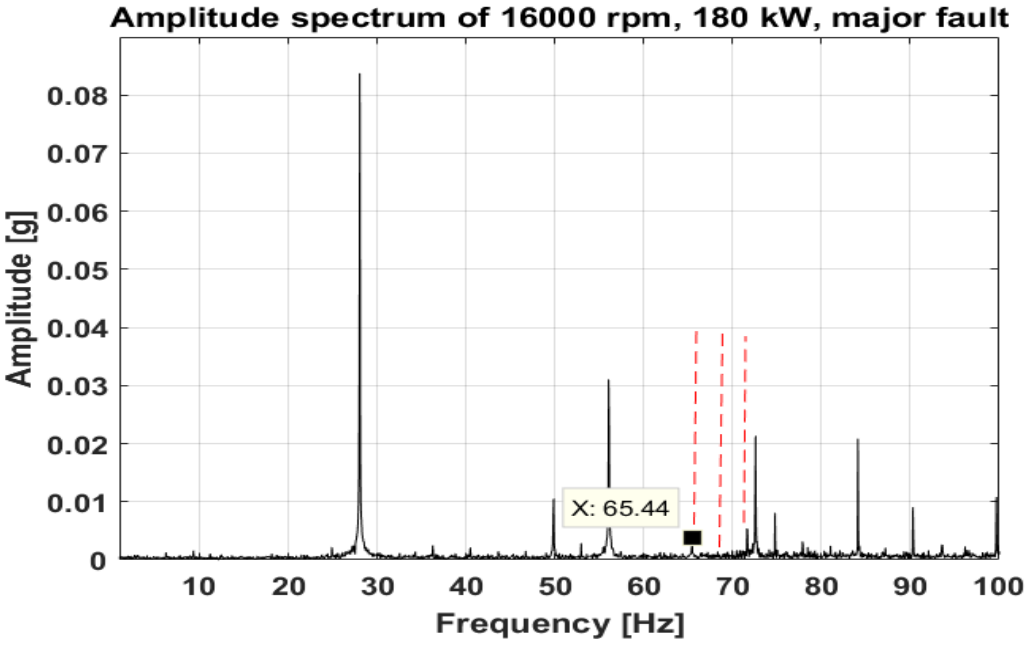

Figure 4.50: Zoomed amplitude spectrum, 16000 rpm, 180 kW major fault condition

Table 4.9: Centre frequency and bandwidth for envelope analysis, 16000 rpm, 180 kW

Conditions	Centre Frequency [Hz]	Bandwidth [Hz]
Healthy	9793	200
Minor Fault	9802	200
Major Fault	9824	200

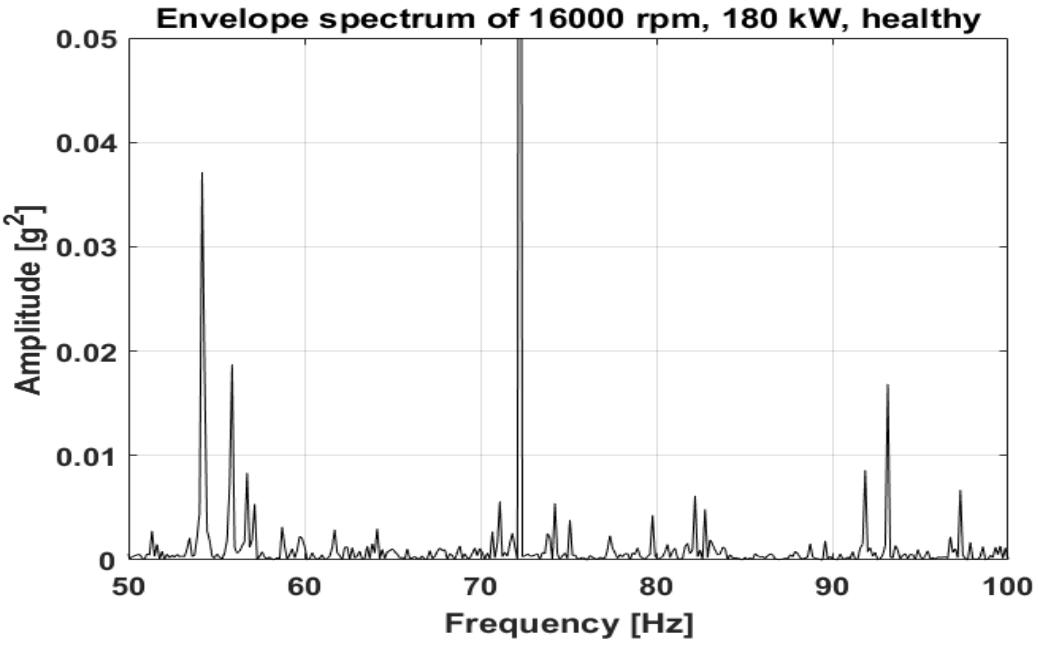

Figure 4.51: Squared envelope spectrum, 16000 rpm, 180 kW healthy condition

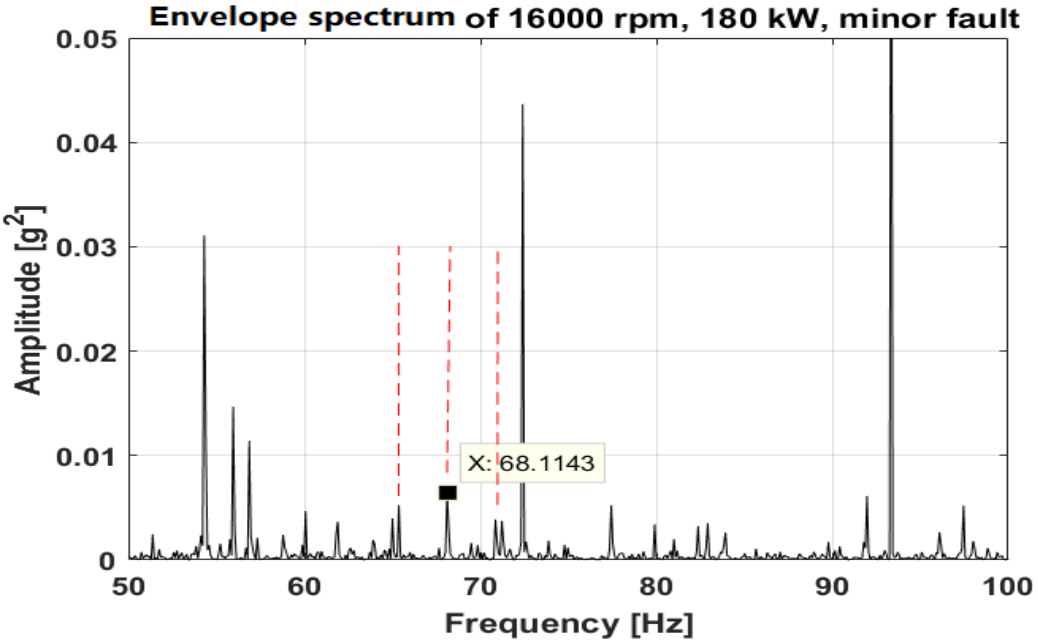

Figure 4.52: Squared envelope spectrum, 16000 rpm, 180 kW minor fault condition

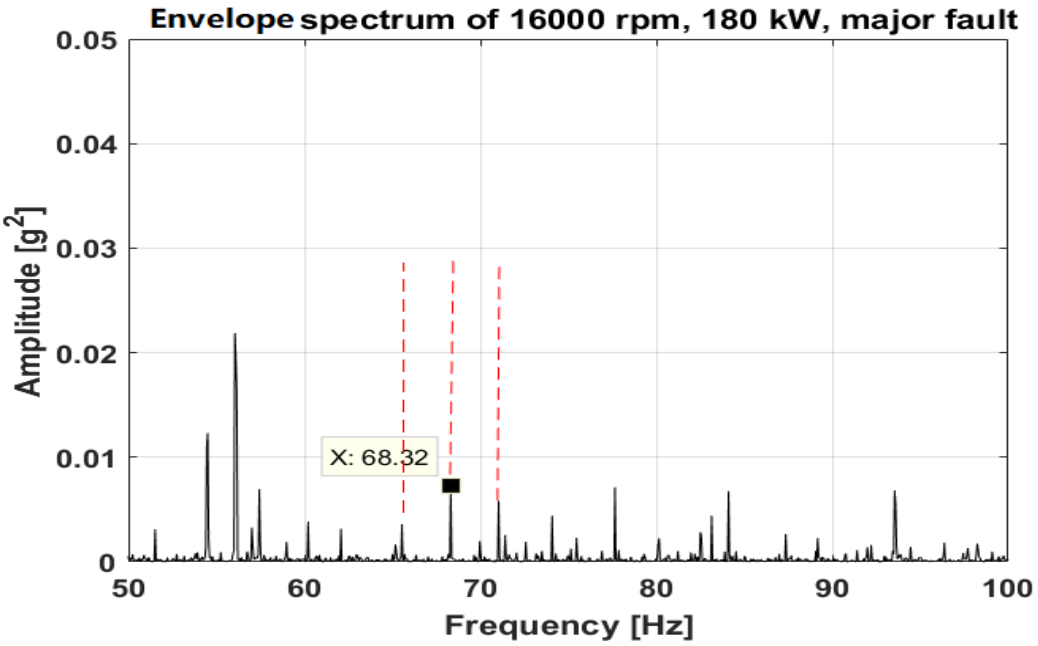

Figure 4.53: Squared envelope spectrum, 16000 rpm, 180 kW major fault condition

4.5 Conclusions

In this Chapter, diagnosis of MGB planetary bearing outer race fault has been investigated. By employing frequency domain based signal analysis techniques, the fault associated frequency components have been successfully extracted. Processing results using data from four conditions, namely 14000 rpm input speed with 100 kW / 180 kW load, and 16000 rpm input speed with 100 kW / 180 kW load, are presented. Detailed frequency inspection has been performed on the 14000 rpm, 100 kW condition, which simulates a relatively relaxed condition for helicopters to stay on ground before taking-off. Explanations to the primary frequencies are given. The diagnosis results for each condition are summarised in below:

1. For 14000 rpm, 100 kW condition, it has been demonstrated that the dominant frequencies are related to gear meshes, 1^{st} epicyclic and 2^{nd} epicyclic module modulations. Additionally, it was discovered that the bicoherence method excels at identifying theses primary frequencies, but fails in diagnosing BPFO. To mitigate the detrimental effect from the gear meshes, SANC has been applied. The effect of SANC has been demonstrated, showing that SANC is effective in eliminating the gear mesh frequencies, given proper delay selected. Kurtogram, which is an algorithm to scan the most impulsive frequency bands hidden in the entire spectrum, did not indicate the accurate centre frequency or bandwidth in this case, concluding that the complex spectrum of MGB movement has a negative impact on the capabilities of Kurtogram, which is in line with the reported conclusion in [117]. The incipient size of the seeded defect has also added difficulties in employing Kurtogram. In order to enable the envelope analysis, manual inspection of frequency resonances and bandwidth were conducted, and optimal results have been acquired in Figure 4.26 and Figure 4.27. Another fast computational algorithm IEC has also been tested and achieved comparable results, shown in Figure 4.29, with a high-pass filter applied.
2. For 14000 rpm, 180 kW condition, similar analysis procedures were performed, and achieved optimal diagnosis result for minor fault condition, shown in Figure 4.38. Cepstrum editing has been applied to further improve the result for major

fault condition diagnosis. Optimised result has been obtained by using a Cepstrum lifter, shown in Figure 4.41.

3. For 16000 rpm, 100 kW condition, it has been observed that the SANC and squared envelope analysis have achieved optimal result in major fault condition in Figure 4.47, which clearly demonstrates the fault associated sidebands and BPFO. For minor condition, the sidebands have shown abnormal increases that are associated with seeded faults, supporting the diagnosis results.
4. For 16000 rpm, 180 kW condition, it has been discovered that applying the squared envelope analysis have been adequate enough to diagnose the faults in both minor and major conditions. Due to the high speed and load, the separation of deterministic gear signals and nondeterministic bearing signals brings limited benefits.

The diagnosis demonstrated for all conditions have concluded that, it is successful, although very challenging, to diagnose incipient planetary bearing outer race defects with frequency domain analysis techniques. The MGB was operated under relatively slow speed and light load conditions, indicating that the diagnosis is feasible to be performed in a non-extreme helicopter flying conditions. Based on the results summarised in the list, generic methods are proposed for the diagnosis of the helicopter main gearbox planetary bearing faults:

1. For 14000 rpm, 100 kW condition, due to that the speed and load adopted were not significant, the fault-associated signals were inherently weak. Therefore, it is proposed to apply adaptive algorithms to filter out the strong gear meshes. Additionally, by utilising Kurtogram in combination with detailed inspections on high frequency resonances, envelop analysis should then be applied to extract the fault frequencies.
2. For 14000 rpm, 180 kW condition, similarly, due to the higher load condition, sidebands were more obvious in spectrum, therefore incorporating the Cepstrum editing can be beneficial to the processing routine.
3. For 16000 rpm, 100 kW condition, with higher speed condition, the signal energy of the fault frequency components increased. Therefore, by applying signal separation

and envelope analysis, the fault frequencies can be extracted. What's more, the sidebands induced by the amplitude modulation of the 2^{nd} epicyclic module carrier have shown to be effective in detecting the planetary bearing faults.

4. For 16000 rpm, 180 kW condition, based on the results, the envelope analysis is applicable to successfully diagnosis the inserted fault.

To intuitively recapitulate the processing routine, it is depicted in Figure 4.54 in below. In the next Chapter, a further evaluation analysis study is presented, demonstrating the diagnosis process applied on a CH-46E helicopter aft gearbox, with seeded planetary bearing inner race defects.

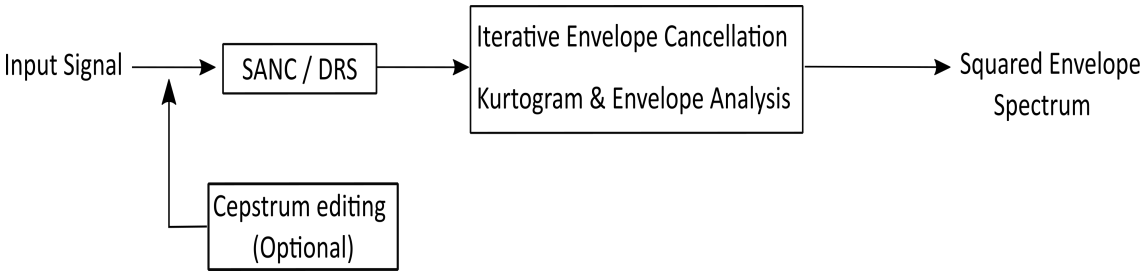

Figure 4.54: Schematic diagram of signal processing procedures

Chapter 5

Planetary Bearing Fault Diagnosis on A CH-46E Helicopter Aft Gearbox

5.1 Introduction

In Chapter 4, successful diagnosis has been demonstrated for identifying seeded incipient planetary bearing outer race defects, under four different conditions. In this Chapter, a comparative study is performed, where the data was collected from a faulty CH-46E helicopter aft gearbox, showcasing the processing routine's capabilities in detecting a different type of the planetary bearing fault, namely the inner race fault, in a different gearbox.

5.2 Description of the Data Acquisition

The vibration data was collected from series of seeded defect tests in a CH-46E aft gearbox, conducted by Westland Helicopter Limited. The collected vibration data was digitalised by Naval Research and Development Centre (NRAD) in 1993 [118]. Based on the information reported in [119], eight conditions were tested, including seven seeded defect conditions and a no-defect condition. Only one type of defect was introduced per test condition. These test conditions are listed as follows:

1. No defect
2. Planetary gear bore / bearing inner race corrosion
3. Spiral bevel input pinion spalling
4. Helical input pinion chipping
5. Collector gear cracking
6. Quill shaft cracking

7. Input pinion bearing corrosion
8. Helical idler gear cracking

Specifically for this Chapter, data collected from the condition "Planetary gear bore / bearing inner race corrosion" was analysed. Eight Endevco 7259A accelerometers were installed on the test-rig, an optical tachometer was also fitted near scavenge pump drive. All data was recorded on individual channels via an analogue tape recorder, and digitalised at a sampling frequency of 103116.08 Hz. The two most relevant accelerometers were installed near epicyclic module, where the fault was seeded. In the rest of the Chapter, the vibration data acquired from the two channels will be referred to as A5 and A6 data, named after the marker of the two accelerometers in the test report [118]. The transmission schematic diagram is illustrated in Figure 5.1. The number of teeth is shown for each gears.

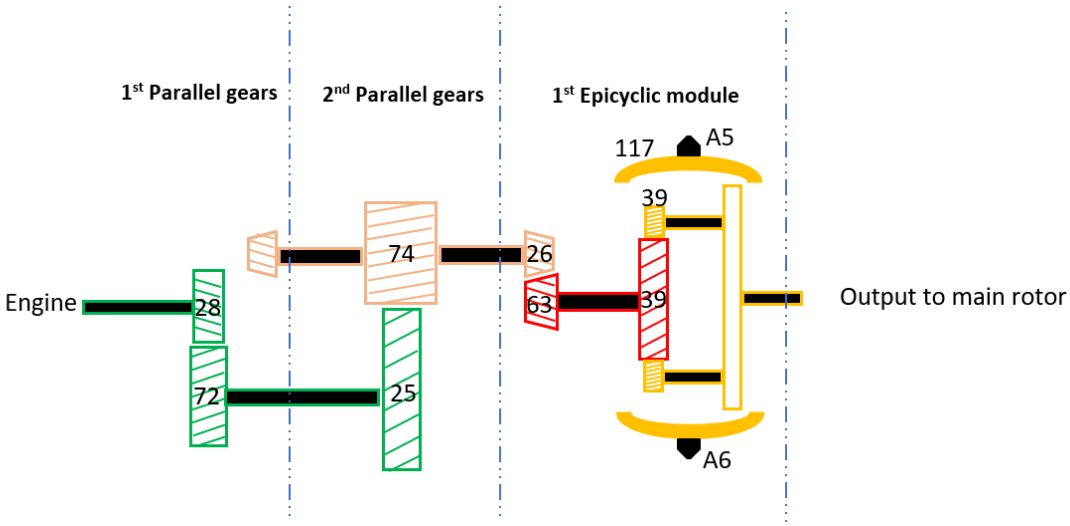

Figure 5.1: Transmission schematic diagram of CH-46E aft gearbox

Table 5.1 details all relevant frequency components associated with the test rig. The planetary bearing inner race defect frequency BPFI and outer race defect frequency BPFO are calculated according to the bearings' geometry structure and rotating speed, utilising the Equation 2.14 and Equation 2.15 specified in Chapter 2. Similarly, the observed defect frequencies could have slight deviations from the calculated values, due to the randomness induced by the slip of bearing rolling elements.

Table 5.1: Diagnostic information for CH-46E aft gearbox

MGB input shaft speed	324.6 Hz
MGB output shaft speed	4.4 Hz
Sampling frequency	103116.1 Hz
Data recording length	21.9 s
Tachometer shaft speed	114.4 Hz
Bearing outer race defect F_{ORD}	68.4 Hz
Bearing inner race defect frequency F_{IRD}	101.7 Hz

Unfortunately, since this experiment was conducted decades ago, it was not possible to track the seeded defect sizes and conditions. Introduced in Chapter 2 and summarised in Chapter 4, frequency-based analysis techniques are essential for extracting defect-induced repetitive signal patterns in frequency domain, therefore providing more indications of defects that cannot be discovered in the time domain. Specifically for bearing fault diagnosis, demodulating structural-related high frequency resonances where bearing signals are amplified is effective in mitigating amplitude modulations, speed fluctuations and the gear meshes [18]. To enhance such processing approach, techniques can be applied to separate non-deterministic bearing signals from deterministic gear signals [64, 72, 73]. To benefit from envelope demodulation, the Kurtogram was developed to identify the frequency band that contains the most impulsive signals associated with structural resonances [93–95]. In the event that Kurtogram cannot given accurate indications, it is required to inspect the spectrum and select the resonances along with the bandwidth, as shown in Chapter 4 results.

5.3 CH-46E helicopter aft planetary bearing fault diagnosis

The schematic diagram for signal processing is depicted in Figure 4.54, summarising from Chapter 4. The strategy adopted to diagnose CH-46 helicopter planetary bearing fault was firstly extracting faulty bearing related signals from the originally acquired vibration data using SANC or DRS, followed by applying iterative envelope cancellation technique. Cepstrum editing was employed as an optional step before SANC or DRS,

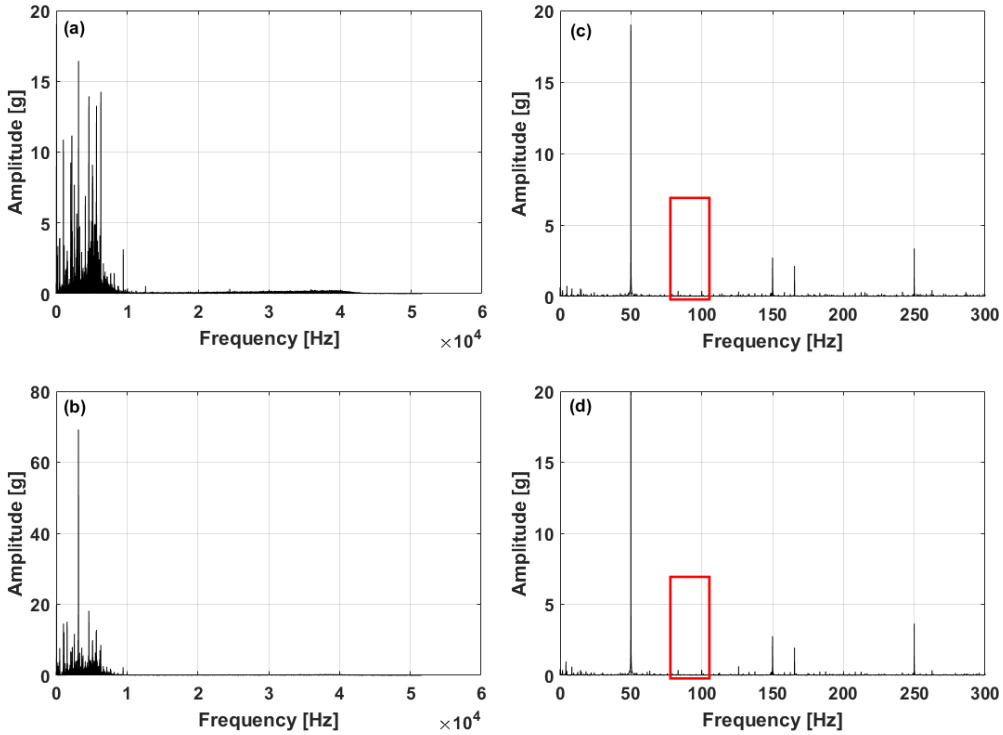

Figure 5.2: Amplitude spectrum of raw vibration data
(a), (c): Amplitude spectrum of A5 data and zoomed spectrum of A5 data
(b), (d): Amplitude spectrum of A6 data and zoomed spectrum of A6 data

where there were requirements to suppress excessive frequency sidebands that cannot be eliminated by separation techniques. This step has been utilised in diagnosing 14000 rpm, 180 kW condition for optimal results. Kurtogram combined with envelope analysis were implemented for comparison with IEC. Basic inspection of the raw vibration data spectrum was first conducted for raw A5 and A6 data, as shown in Figure 5.2.

From Figure 5.2, it is observed that very limited information can be found in bandwidth higher than approximately 10 kHz. It is inferred that frequency contents higher than 10 kHz were pre-filtered during the acquisition process. From zoomed spectrum, no existence of inner race or outer race defect frequency can be observed. Discrete frequency spikes that are related to gear meshes and shaft rotations are dominant in Figure 5.2(c) and 5.2(d).

DRS and SANC were then applied to provide comparative separation results for iterative

envelope cancellation. To determine the best delays for both techniques, a range of time delays from 100 to 300 periods of 10 kHz were considered, according to the recommendations from Randall and Antoni [45] . In Figure 5.3, the separation using DRS for A5 data is demonstrated. The delay was selected to be 1400 data points, filter length was chosen to allow 2000 times of averages to mitigate potential speed fluctuations. It is clearly shown that large discrete frequency components in Figure 5.3(a) have been effectively eliminated in Figure 5.3(b).

Similar steps were taken to process A6 data, then the separated signals from A5 and A6 were processed with IEC. For A5 signal, to control the optimal output with least interferences, a 5 kHz high-pass filter was applied to further reduce low frequency gear meshes. A stop factor η was selected at 0.85. The output of iterative envelope cancellation was squared envelope spectrum, which was zoomed into 0-300 Hz range for defect frequency identification.

Figure 5.4 clearly demonstrates the existence of the 70.28 Hz outer race defect frequency and the 101.02 Hz inner race defect frequency. The presence of 13.18 Hz, which is 3 times the planetary carrier shaft speed (4.4 Hz), is associated with the planetary gear rotation speed, i.e. $4.4 \times 117/39 = 13.2$ Hz, where 117 is the number of ring gear tooth and 39 is the number of planet gear tooth. The frequency at 105.4 Hz was noted as a modulation sideband that resulted from 4.4 Hz drive shaft frequency. To further suppress unwanted frequency components, Cepstrum editing was attempted to A5 data. The real Cepstrum of A5 data is shown in Figure 5.5.

In Figure 5.5, it is evident that the 0.23 quefrency which corresponds to 4.4 Hz is dominant. In order to retain the characteristics of low quefrency contents and suppress high quefrency contents, a short-pass lifter was applied for all quefrency components below $1/114.2\ Hz$. The pass region is marked in Figure 5.5. This step was performed according to the diagnosis for 14000 rpm, 180 kW condition.

Figure 5.6 shows the squared envelope spectrum after incorporating short-passed Cepstrum editing. The inner race defect frequency of BPFI at 101.02 Hz is more distinct compared with that shown in Figure 5.4, while the outer race defect frequency BPFO at

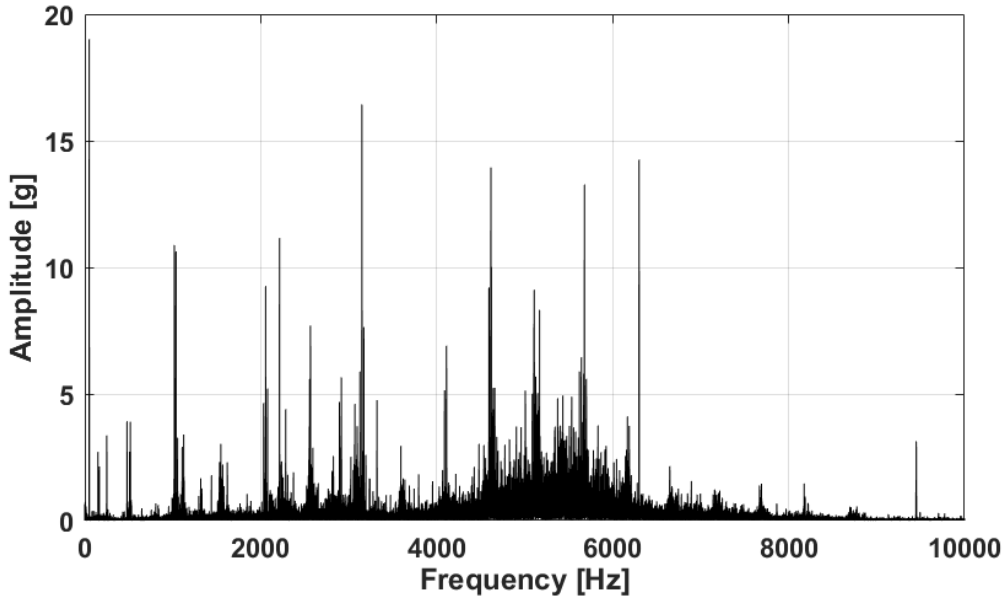

(a) Amplitude spectrum of A5 data before DRS separation

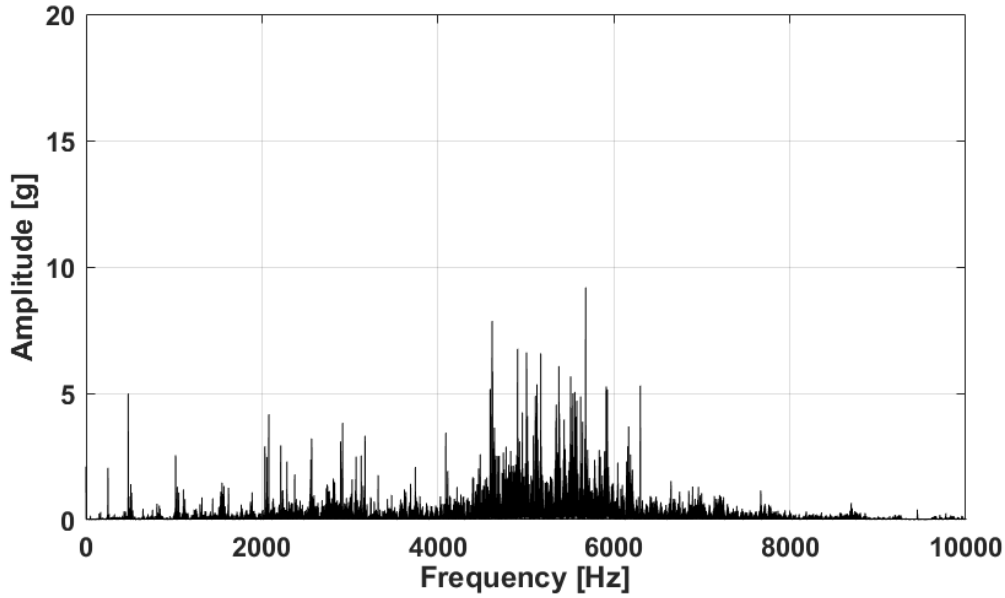

(b) Amplitude spectrum of A5 data after DRS separation

Figure 5.3: Demonstration of DRS separation effect for A5 data, delay = 1400

70.28 Hz has been suppressed. However, the 65.9 Hz component which is a 4.4 Hz sideband of BPFO can still be observed. The other interference sidebands have been largely suppressed.

Comparatively, the results using Cepstrum editing, SANC and IEC are shown in Figure

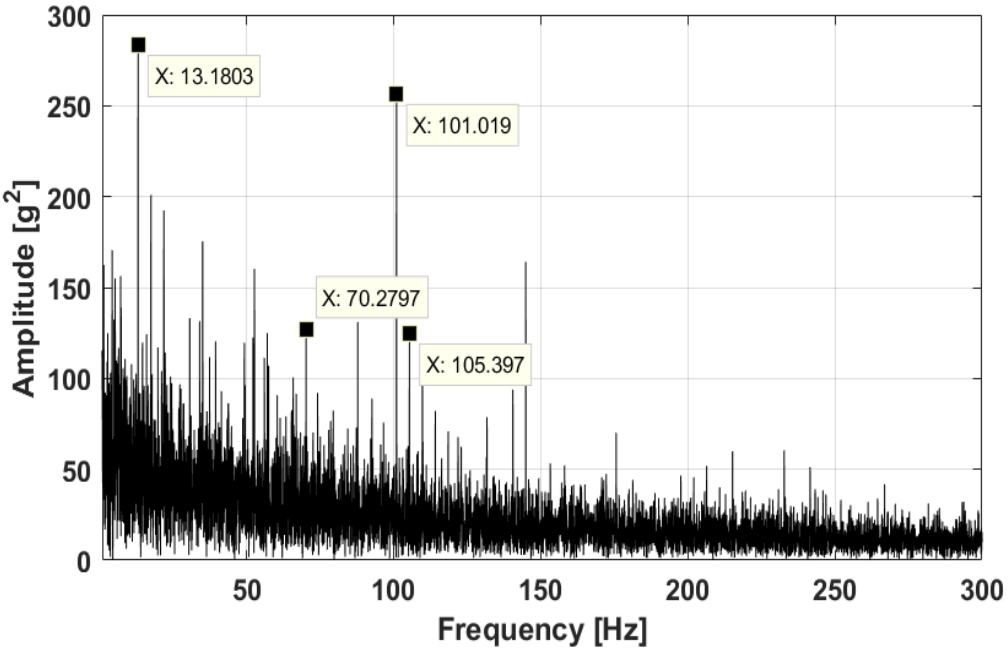

Figure 5.4: Squared envelope spectrum with DRS and iterative envelope cancellation, A5 data

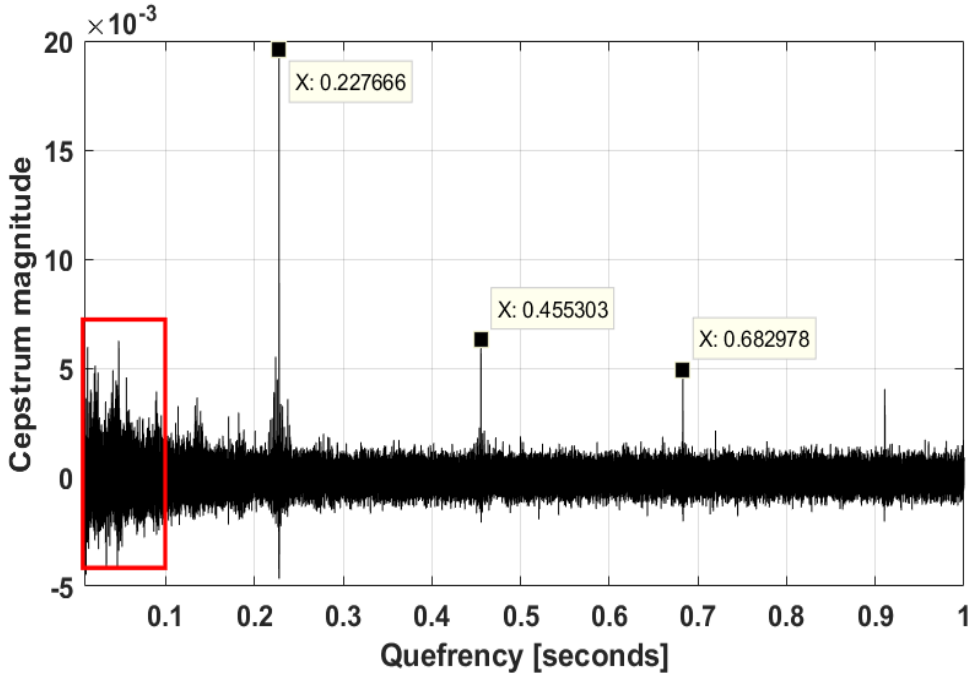

Figure 5.5: Real Cepstrum of A5 data

5.7. In Figure5.7(a), it is demonstrated that, using SANC with IEC can reveal inner race defect frequency at 101.2 Hz. However, only 4.4 Hz sideband of outer race defect frequency can be observed at 74.67 Hz. In Figure 5.7(b), the result suggests that

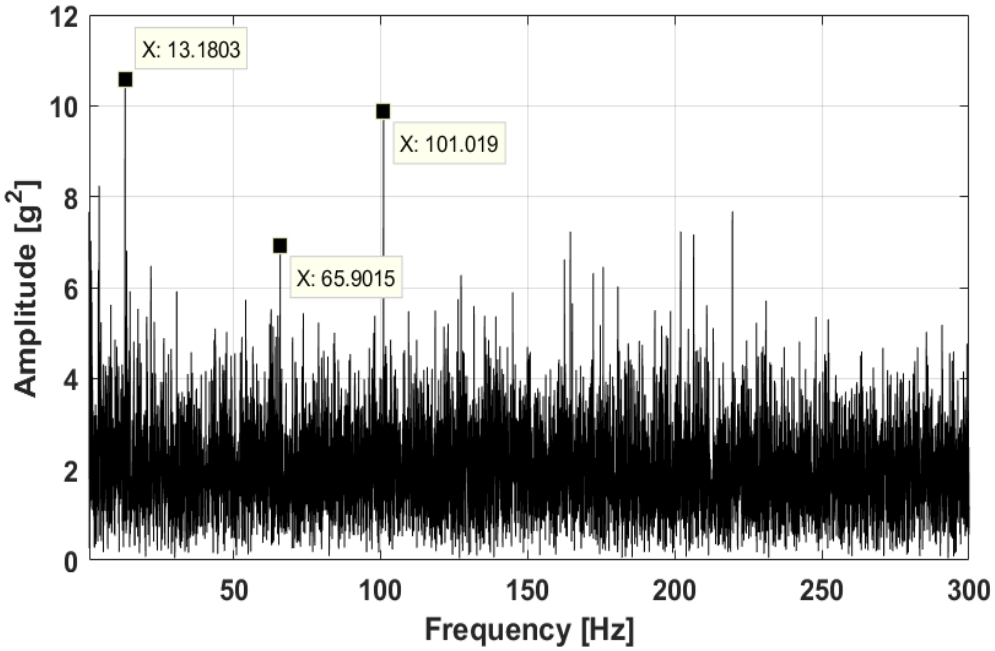

Figure 5.6: Squared envelope spectrum of A5 data, processed using Cepstrum editing, DRS and IEC

combining Cepstrum editing and SANC can achieve suppression of 101.02 Hz BPFI component, but revealing 70.27 Hz BPFO.

The signal processing for A6 data followed similar procedures. Cepstrum editing, DRS separation and iterative envelope cancellation techniques were applied to A6 data. The results are shown in Figure 5.8.

In Figure 5.8(a), the diagnosis result is conclusive. The 101.02 Hz BPFI was clearly evident, as well as the ‘4.4 Hz drive shaft speed, while the BPFO is still masked. Practically at this point, applying Cepstrum editing could be redundant since the sidebands around BPFI are not dominant, but for the investigation of BPFO, Cepstrum editing is performed in Figure 5.8(b). Result proves that Cepstrum editing may render some losses for inner race defect bearing signal, whereas the 70.3 Hz BPFO is revealed.

Comparatively, squared envelope spectrum results produced using SANC as separation technique is demonstrated in Figure 5.9. Applying SANC without Cepstrum for A6 data can reveal the fault-related sideband 105.4 Hz, but no direct indication of fault frequency can be observed for both BPFO and BPFI. Moreover, applying Cepstrum editing in Figure

5.9(b) tends to severely eliminate residual bearing signal under this circumstance.

Kurtogram combined with envelope spectrum analysis were implemented as a comparison to the optimal results demonstrated in Figure 5.4 and Figure 5.8. DRS filtered A5 and A6 data were adopted as inputs for Kurtogram.

Kurtogram indication for A5 data and corresponding squared envelope spectrum are shown in Figure 5.10. It is indicated that the optimal bandpass centre frequency is 12889.5 Hz with a bandwidth of 25779.02 Hz. The demodulated squared envelope spectrum in Figure 5.11 contains distinct indication of F_{IRD} near 101 Hz and F_{ORD} near 70 Hz, however, the sidebands and harmonics are excessive compared with result shown in Figure 5.4 using iterative envelope cancellation techniques. Similarly, processing result using Kurtogram for A6 data is shown in Figure 5.12, where fault frequencies can be identified, but the spectrum is also contaminated by excessive frequency sidebands and harmonics.

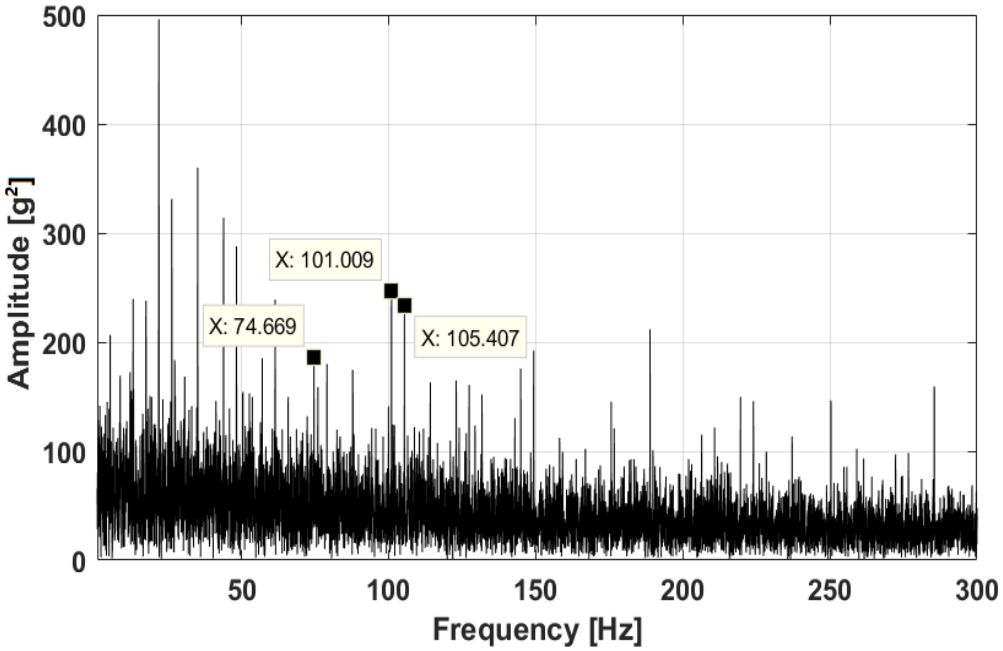

(a) Squared envelope spectrum of A5 data, processed using SANC and IEC

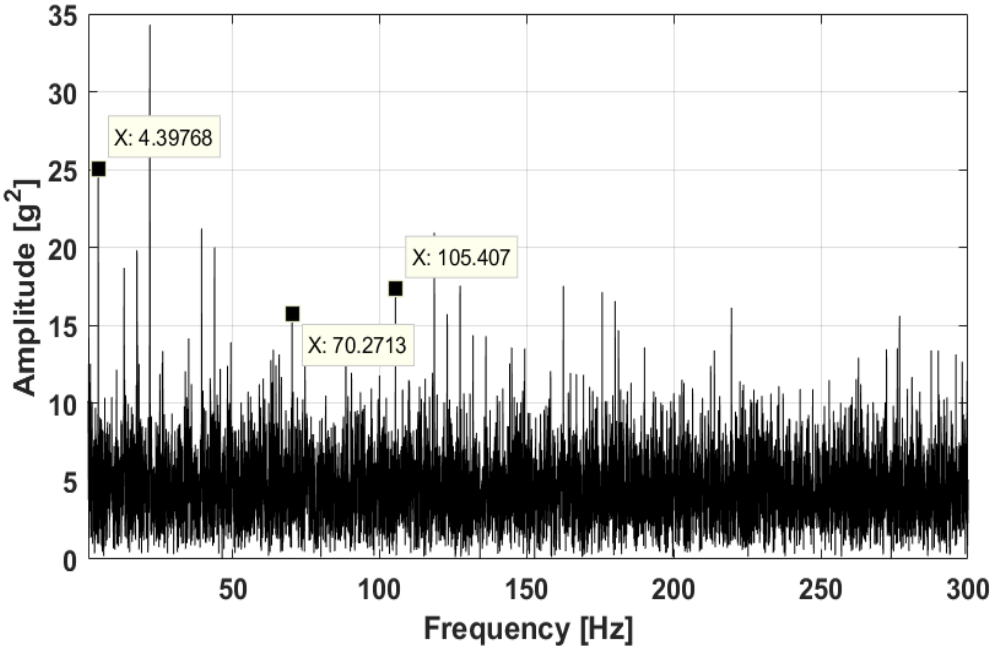

(b) Squared envelope spectrum of A5 data, processed using Cepstrum editing, SANC and IEC

Figure 5.7: Squared envelope spectrum of A5 data processed using SANC, IEC and Cepstrum editing techniques

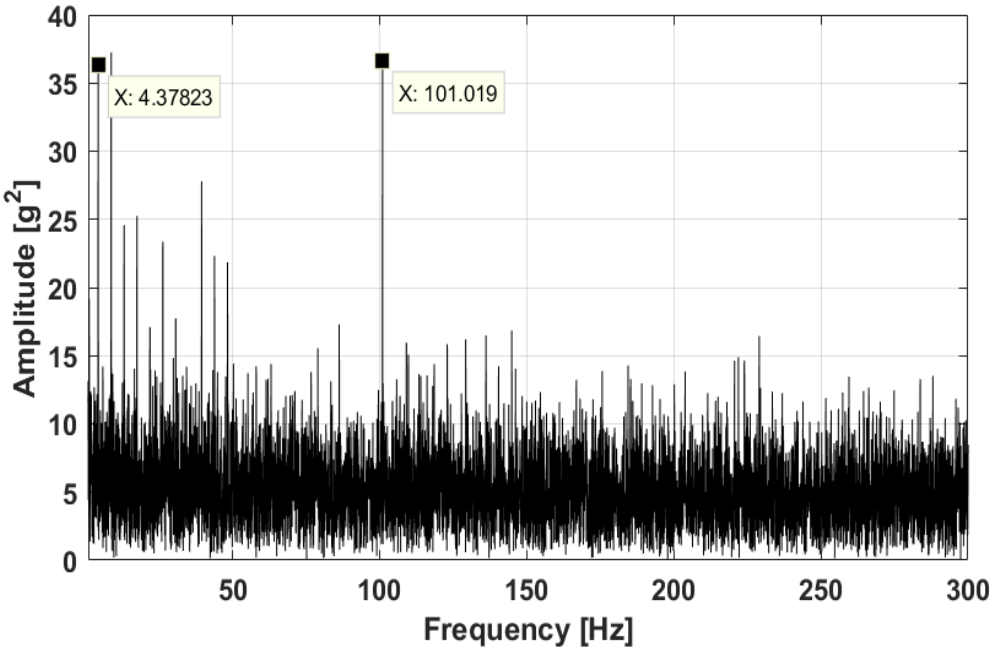

(a) Squared envelope spectrum of A6 data, processed using DRS and IEC

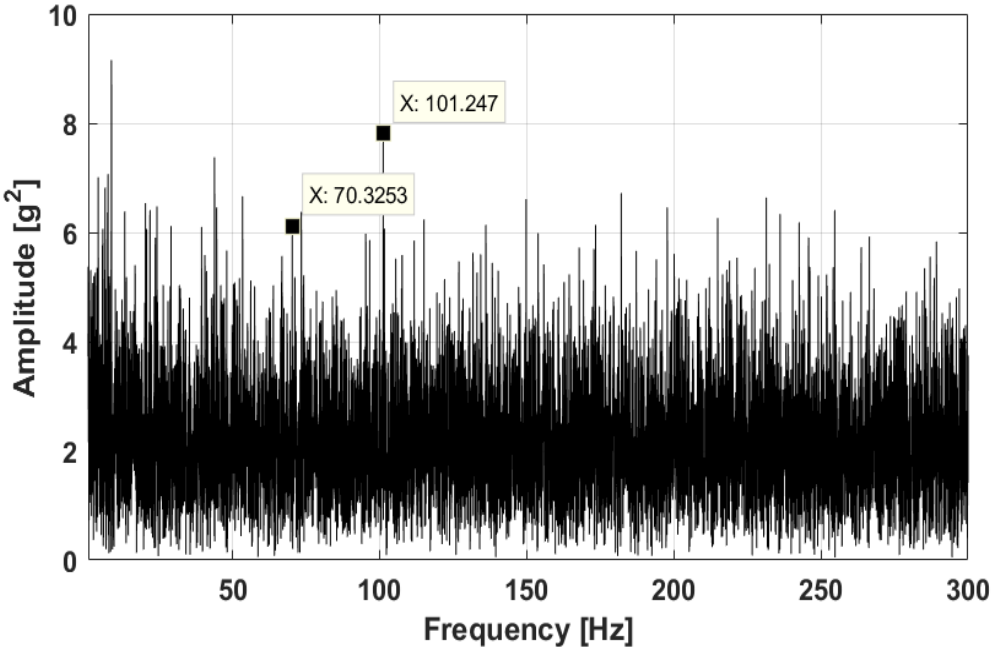

(b) Squared envelope spectrum of A6 data, processed using Cepstrum editing, DRS and IEC

Figure 5.8: Squared envelope spectrum of A6 data processed using DRS, IEC and Cepstrum editing techniques

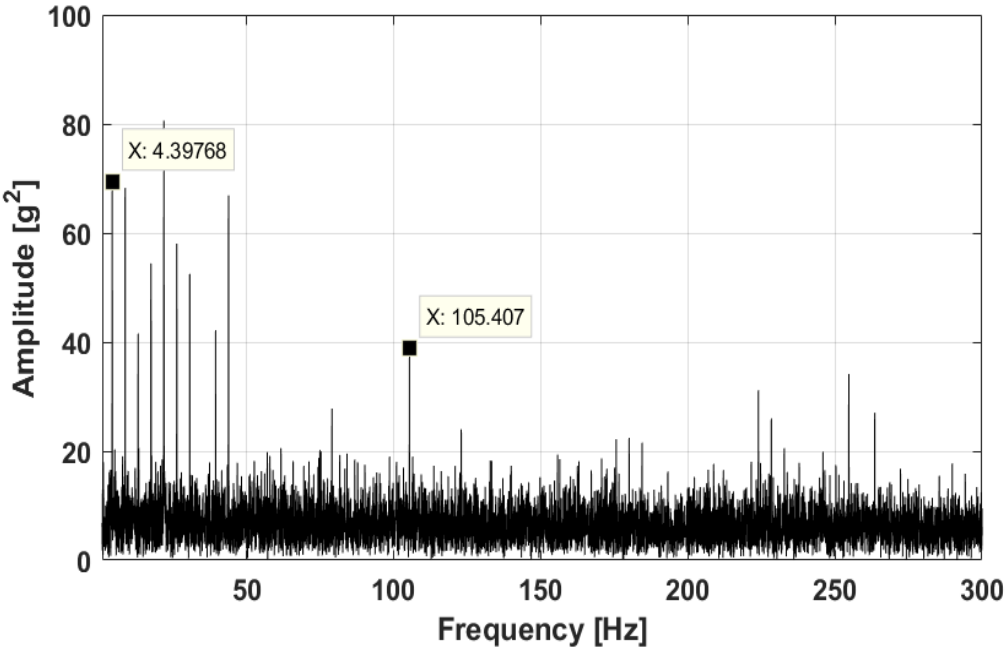

(a) Squared envelope spectrum of A6 data, processed using SANC and IEC

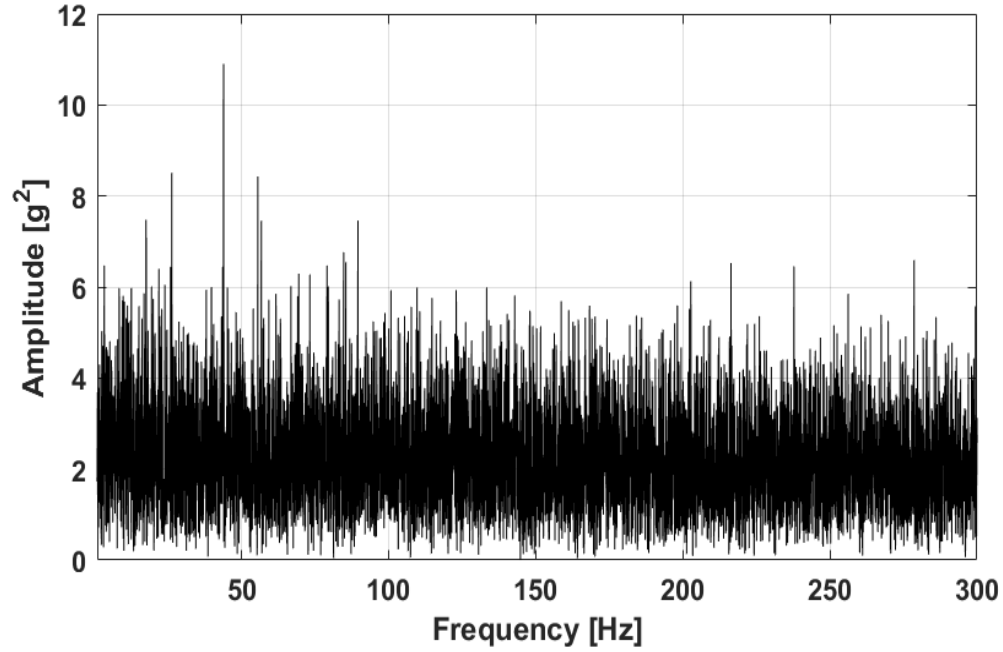

(b) Squared envelope spectrum of A6 data, processed using Cepstrum editing, SANC and IEC

Figure 5.9: Squared envelope spectrum of A6 data processed using SANC, IEC and Cepstrum editing techniques

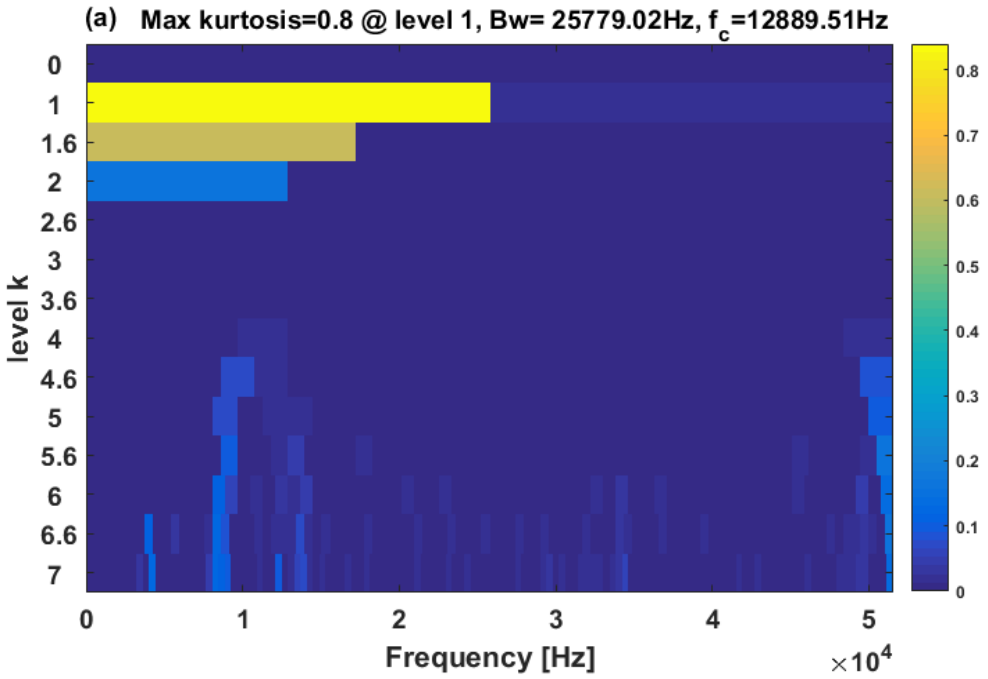

Figure 5.10: Kurtogram of A5 data after DRS filteriing

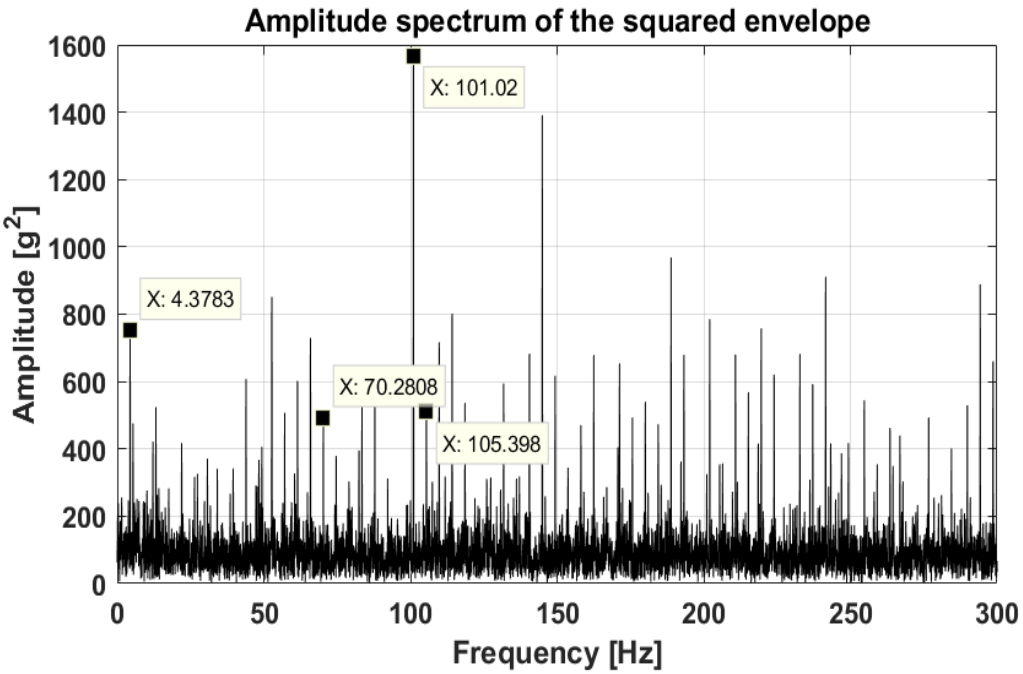

Figure 5.11: Squared envelope spectrum based on the indication from Figure 5.10

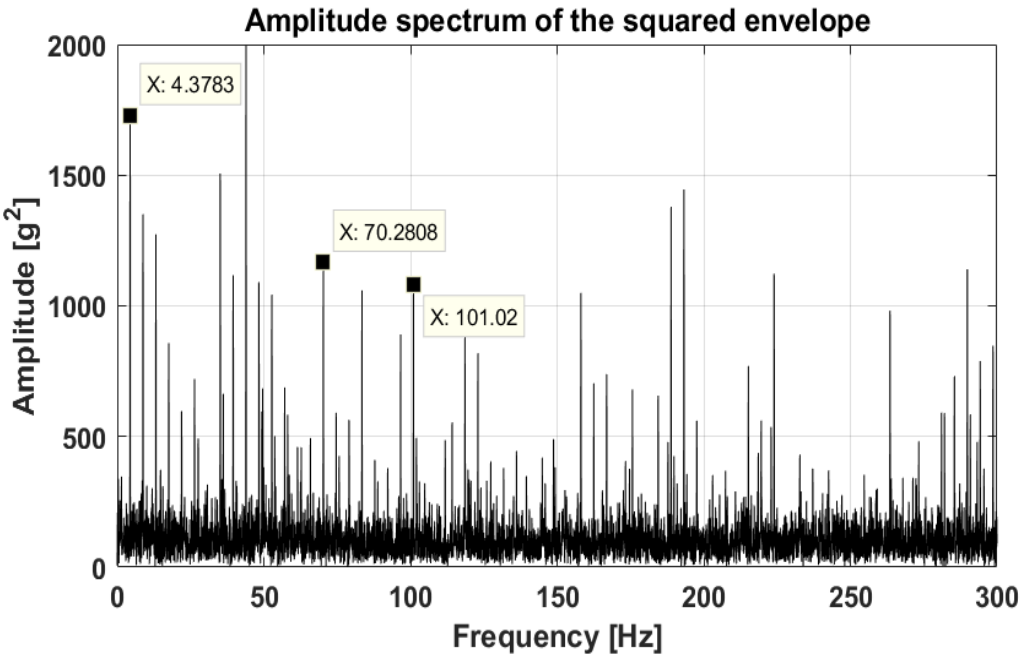

Figure 5.12: Squared envelope spectrum of DRS filtered A6 data

5.4 Conclusion

In this Chapter, the CH-46E helicopter planetary bearing inner race defect and outer race defect were successfully diagnosed for both A5 and A6 channel by implementing frequency domain analysis techniques including DRS, SANC, Cepstrum editing, IEC and Kurtogram combined with envelope analysis. Decisive indications of fault-related frequency components can be directly observed in squared envelope spectrum shown in Figure 5.4 and Figure 5.8. Processing techniques were evaluated in terms of their efficacy and effectiveness. Regarding the CH-46E helicopter dataset, due to the high data sampling frequency (103116.08 Hz) and large data size, SANC was less efficient, attributed to its adaptive process. Meanwhile, the DRS technique has performed considerably well in combination with the iterative envelope cancellation technique, which is capable of suppressing residual gear mesh and frequency sidebands. Cepstrum editing can be adopted as an additional technique to deal with frequency sidebands, but it could also potentially hinder the extraction of the weak bearing signals, e.g. A6 data in this case. Kurtogram has given reliable diagnosis results, comparing with the analysis in Chapter 4, due to less complicated gearbox structure, and significantly higher sampling rate.

The successful extraction of frequency domain diagnostic information has produced intuitive indications for CH-46E helicopter planetary bearing defects. The frequency domain analysis routine for helicopter planetary bearing fault diagnosis is thus established and validated with the successful diagnosis shown in both Chapter 4 and this Chapter.

Chapter 6

Conclusions and Future Work

6.1 Summary of the Thesis

In summary, the study reported in this thesis established and evaluated the diagnosis of helicopter incipient planetary bearing fault, using frequency domain signal processing techniques. Experiments under various test conditions were undertaken on a SA330 helicopter MGB to facilitate the diagnosis study. The results have shown that it is prominent and beneficial to incorporate frequency domain analysis routine to enhance the helicopter condition monitoring system, HUMS.

In Chapter 1, the background of this study was described, summarising that while MGB is critical to ascertain the helicopter's airworthiness and flight safety, HUMS has not always been accurate and sensitive to the planetary bearing faults. This is due to the complex structure of the planetary speed reduction system, resulted in varying signal transmission paths; and also the unique structure of planetary gears sharing race with planetary bearings, hence overwhelming the bearing signals. In Chapter 2, literature review was conducted to investigate in possible solutions to resolve these issues. Firstly the fundamentals of vibration-based condition monitoring was presented, introducing that the most prevailing vibration processing techniques are enabled with frequency based analysis. The introduction of VHM employed in HUMS was then reviewed, where the commonly used CIs were also discussed, summarising that most of the CIs are designed for deterministic gear signals. Additionally, CIs' performance are subject to the severities and propagations of the fault, resulting in inaccuracy and insensitivities to incipient bearing faults. Therefore, the frequency domain processing techniques that specifically target and inspect the bearing fault related frequencies were reviewed.

In Chapter 3, the experimental work was described. A deep understanding was developed to the fundamentals of the planetary speed reduction system. The work principles for such system and the analysis to determine the speed reduction ratios were explained, which were essential for conducting the diagnosis work in Chapter 4. The setup of the test rig, data acquisitions and test conditions were described in detail. The lowest test speed conditions were selected to be 14000 rpm, based on the considerations of simulating the relaxed helicopter operational condition, which was idle on the ground before take-off. Another speed was selected to be 16000 rpm, with a slight safety margin applied to the maximum rig speed 17842 rpm. The seeded bearing defects were created with the incipient sizes recommended by EASA, making the diagnosis increasingly challenging compared with previous study in [3]. It was also reported in Chapter 3, that an emergency shutdown of the MGB test rig has occurred, lead by an imbalance or material issue at the speed-increase gearbox connection assembly gears. After rectifying the issues, seeded bearing fault tests were carried out and invaluable vibration data has been successfully captured at various test conditions using this MGB test rig.

In Chapter 4, diagnosis of MGB planetary bearing outer race fault using frequency domain signal analysis techniques was investigated. Processing results using data from four conditions, namely 14000 rpm input speed with 100 kW / 180 kW load, and 16000 rpm input speed with 100 kW / 180 kW load, were presented. Detailed analysis has been performed, the dominant frequency components were explained, showing a complex and gear mesh dominant spectrum characteristics. The processing routine that comprised of steps including gear/bearing separation, interference suppression, signal demodulation and fault frequency extraction was performed and evaluated. In Chapter 5, a comparative study was conducted on diagnosis of a CH-46E helicopter Aft gearbox with seeded bearing outer and inner race defects. The diagnosis results further support the prominent conclusion from Chapter 4. Summarising the analysis from Chapter 4 and Chapter 5, the conclusions have been drawn:

1. The diagnosis routine was successful in identifying the seeded planetary bearing outer race defect, in 14000 rpm 100/180 kW and 16000 rpm 100/180 kW conditions. Observations can be made that higher speed and higher load conditions

were easier to diagnose. No signal separation was needed for 16000 rpm, 180 kW load whereas the other conditions did require this step to be performed.

2. In terms of the effectiveness of the applied processing techniques, the conclusions are drawn as the following. For suppressing gear mesh frequencies, Cepstrum analysis is not mandated, but does have enhanced the diagnosis under very low speed condition, e.g. 14000 rpm,180 kW. The effect of Cepstrum analysis was also evaluated in combination with DRS in the comparative study, where the CH-46E Aft gearbox data was utilised. Due to its computational efficiency, DRS excels at processing data collected under stable speed conditions with large data size, either resulted from excessive sampling rate or long recording time. Whereas SANC, as has prominently shown in Chapter 4, provides better separation results when the data size was not an issue.
3. Kurtogram has shown situational applications, whose successes can be found when the data contains significant diagnostic information, due to either severe defect sizes, extreme speed/load conditions or simple machinery structures. Kurtogram was not very successful when dealing with the experimental data collected in this study, because of the incipient seeded defect sizes and low speed/load condition.
4. Similar to DRS, IEC offers quite the efficiency in computation, which is beneficial for industrial application, but it suffers from the negative effects aforementioned. Both Kurtogram and IEC can be effective when MGB was operated under heavy load condition with severe fault sizes, showing descend application in addressing epicyclic carrier modulation and gear mesh masking bearing signals as reported in [120].
5. Envelope analysis is overall the key technique to extract the bearing-associated information, and then perform the inspection in frequency spectrum. The squared envelope has been proven to be effective with appropriate centre frequency and bandwidth selected.

The successful diagnosis of the planetary bearing defects using frequency domain signal processing techniques has produced intuitive indications for the fault existence and types. The analysis provides immense benefits if appropriately incorporated into current HUMS signal analysis procedure, enhancing its capabilities of detecting planetary

bearings associated defect in early stages.

6.2 Contributions of This Study

The major contribution of this study are listed below.

1. Collecting invaluable experimental data. Not many studies have been published using data collected from real helicopter MGB. Additionally, the MGB was operated under slow speed, light load conditions with incipient defect sizes, making the diagnosis increasingly challenging. The collected data has already been supplied to other researchers to enable their studies [121].
2. Investigating, evaluating of the applicability of various frequency domain signal analysis techniques as well as proposing using frequency sidebands induced by the carrier of epicyclic module as novel indicators for planetary bearing faults. These contribute to the knowledge of diagnosing incipient helicopter planetary bearing faults in challenging conditions as mentioned above.
3. Establishing and validating the diagnosis routine, consisting of suppressing and eliminating dominant gear mesh frequencies, determining optimal centre frequency and associated bandwidth for demodulation, squared envelope spectrum analysis. A further evaluation study on diagnosis of CH-46E helicopter geearbox supports these conclusions.

6.3 Future Work

The recommendations for the continuation of this research in future are summarised as follows:

1. With the diagnosis concluded to be successful, planetary bearing CIs can be effectively developed and validated as the next step, providing more accurate and sensitive indications to planetary bearing faults.
2. It is highly beneficial and desirable to develop an automatic analyser incorporating the established processing routine, so that the diagnosing process can be both efficient and industrial applicable.

3. It has been reported in literature facilitated by this study that, it can be beneficial to investigate on applying cyclostationary analysis to optimise the selection of centre frequency and bandwidth for envelope analysis. Although successes have been reported in [121] using helicopter data collected under severe fault conditions, further validations are required using the experimental data collected under incipient defect and light load conditions within this study.
4. In this study, the speed of the rig was maintained in a relatively stable condition. It is desirable to conduct subsequent tests under varying speed conditions, and investigate on the effectiveness of including signal processing techniques to address diagnosis of planetary bearing fault under varying operational speed.

Appendix A

Accelerometers specification sheet

Figure A.1: Specification sheet of PCB 356A43

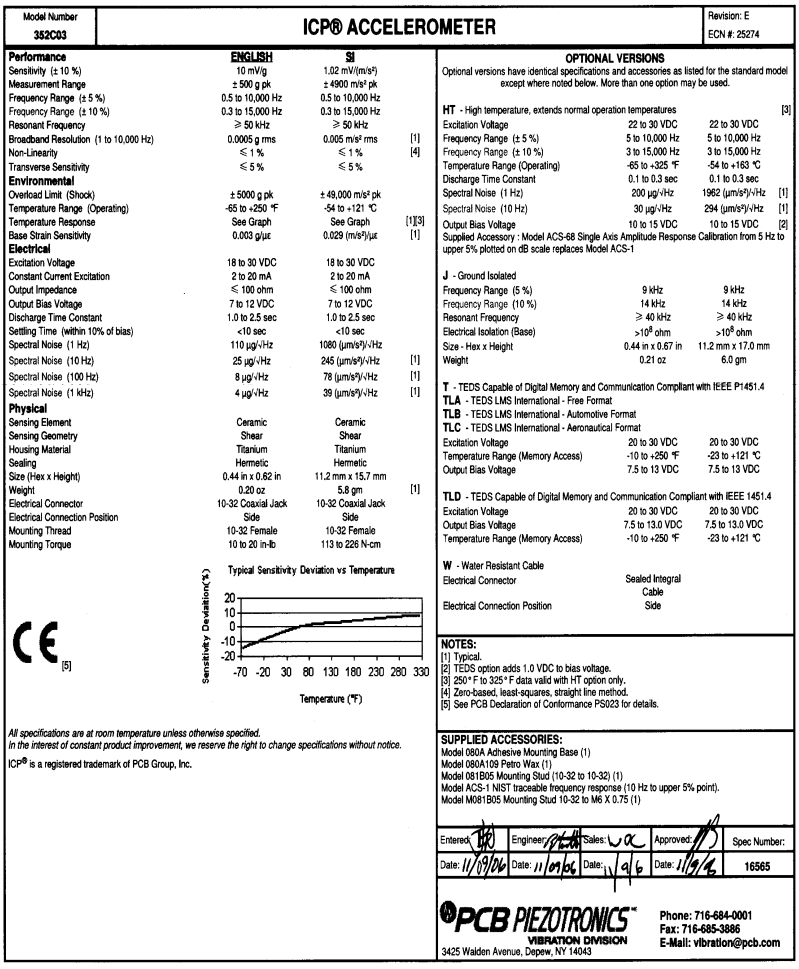

Model Number 352C03

ICP® ACCELEROMETER

Revision: E
ECN #: 25274

Performance	ENGLISH	SI	
Sensitivity (± 10 %)	10 mV/g	1.02 mV/(m/s²)	
Measurement Range	± 500 g pk	± 4900 m/s² pk	
Frequency Range (± 5 %)	0.5 to 10,000 Hz	0.5 to 10,000 Hz	
Frequency Range (± 10 %)	0.3 to 15,000 Hz	0.3 to 15,000 Hz	
Resonant Frequency	≥ 50 kHz	≥ 50 kHz	
Broadband Resolution (1 to 10,000 Hz)	0.0005 g rms	0.005 m/s² rms	[1]
Non-Linearity	≤ 1 %	≤ 1 %	[4]
Transverse Sensitivity	≤ 5 %	≤ 5 %	
Environmental			
Overload Limit (Shock)	± 5000 g pk	± 49,000 m/s² pk	
Temperature Range (Operating)	-65 to +250 °F	-54 to +121 °C	
Temperature Response	See Graph	See Graph	[1][3]
Base Strain Sensitivity	0.003 g/με	0.029 (m/s²)/με	[1]
Electrical			
Excitation Voltage	18 to 30 VDC	18 to 30 VDC	
Constant Current Excitation	2 to 20 mA	2 to 20 mA	
Output Impedance	≤ 100 ohm	≤ 100 ohm	
Output Bias Voltage	7 to 12 VDC	7 to 12 VDC	
Discharge Time Constant	1.0 to 2.5 sec	1.0 to 2.5 sec	
Settling Time (within 10% of bias)	<10 sec	<10 sec	
Spectral Noise (1 Hz)	110 μg/√Hz	1080 (μm/s²)/√Hz	
Spectral Noise (10 Hz)	25 μg/√Hz	245 (μm/s²)/√Hz	[1]
Spectral Noise (100 Hz)	8 μg/√Hz	78 (μm/s²)/√Hz	[1]
Spectral Noise (1 kHz)	4 μg/√Hz	39 (μm/s²)/√Hz	[1]
Physical			
Sensing Element	Ceramic	Ceramic	
Sensing Geometry	Shear	Shear	
Housing Material	Titanium	Titanium	
Sealing	Hermetic	Hermetic	
Size (Hex x Height)	0.44 in x 0.62 in	11.2 mm x 15.7 mm	
Weight	0.20 oz	5.8 gm	[1]
Electrical Connector	10-32 Coaxial Jack	10-32 Coaxial Jack	
Electrical Connection Position	Side	Side	
Mounting Thread	10-32 Female	10-32 Female	
Mounting Torque	10 to 20 in-lb	113 to 226 N-cm	

Typical Sensitivity Deviation vs Temperature

CE [5]

All specifications are at room temperature unless otherwise specified.
In the interest of constant product improvement, we reserve the right to change specifications without notice.

ICP® is a registered trademark of PCB Group, Inc.

OPTIONAL VERSIONS

Optional versions have identical specifications and accessories as listed for the standard model except where noted below. More than one option may be used.

HT - High temperature, extends normal operation temperatures			[3]
Excitation Voltage	22 to 30 VDC	22 to 30 VDC	
Frequency Range (± 5 %)	5 to 10,000 Hz	5 to 10,000 Hz	
Frequency Range (± 10 %)	3 to 15,000 Hz	3 to 15,000 Hz	
Temperature Range (Operating)	-65 to +325 °F	-54 to +163 °C	
Discharge Time Constant	0.1 to 0.3 sec	0.1 to 0.3 sec	
Spectral Noise (1 Hz)	200 μg/√Hz	1962 (μm/s²)/√Hz	[1]
Spectral Noise (10 Hz)	30 μg/√Hz	294 (μm/s²)/√Hz	[1]
Output Bias Voltage	10 to 15 VDC	10 to 15 VDC	[2]

Supplied Accessory : Model ACS-68 Single Axis Amplitude Response Calibration from 5 Hz to upper 5% plotted on dB scale replaces Model ACS-1

J - Ground Isolated		
Frequency Range (5 %)	9 kHz	9 kHz
Frequency Range (10 %)	14 kHz	14 kHz
Resonant Frequency	≥ 40 kHz	≥ 40 kHz
Electrical Isolation (Base)	$>10^8$ ohm	$>10^8$ ohm
Size - Hex x Height	0.44 in x 0.67 in	11.2 mm x 17.0 mm
Weight	0.21 oz	6.0 gm

T - TEDS Capable of Digital Memory and Communication Compliant with IEEE P1451.4
TLA - TEDS LMS International - Free Format
TLB - TEDS LMS International - Automotive Format
TLC - TEDS LMS International - Aeronautical Format

Excitation Voltage	20 to 30 VDC	20 to 30 VDC
Temperature Range (Memory Access)	-10 to +250 °F	-23 to +121 °C
Output Bias Voltage	7.5 to 13 VDC	7.5 to 13 VDC

TLD - TEDS Capable of Digital Memory and Communication Compliant with IEEE 1451.4

Excitation Voltage	20 to 30 VDC	20 to 30 VDC
Output Bias Voltage	7.5 to 13.0 VDC	7.5 to 13.0 VDC
Temperature Range (Memory Access)	-10 to +250 °F	-23 to +121 °C

W - Water Resistant Cable

Electrical Connector	Sealed Integral Cable	
Electrical Connection Position	Side	

NOTES:
[1] Typical.
[2] TEDS option adds 1.0 VDC to bias voltage.
[3] 250° F to 325° F data valid with HT option only.
[4] Zero-based, least-squares, straight line method.
[5] See PCB Declaration of Conformance PS023 for details.

SUPPLIED ACCESSORIES:
Model 080A Adhesive Mounting Base (1)
Model 080A109 Petro Wax (1)
Model 081B05 Mounting Stud (10-32 to 10-32) (1)
Model ACS-1 NIST traceable frequency response (10 Hz to upper 5% point).
Model M081B05 Mounting Stud 10-32 to M6 X 0.75 (1)

Entered:	Engineer:	Sales:	Approved:	Spec Number:
Date: 11/09/06	Date: 11/09/06	Date: 11/9/06	Date: 11/09/06	16565

PCB PIEZOTRONICS™
VIBRATION DIVISION
3425 Walden Avenue, Depew, NY 14043
Phone: 716-684-0001
Fax: 716-685-3886
E-Mail: vibration@pcb.com

Figure A.2: Specification sheet of PCB 352C03

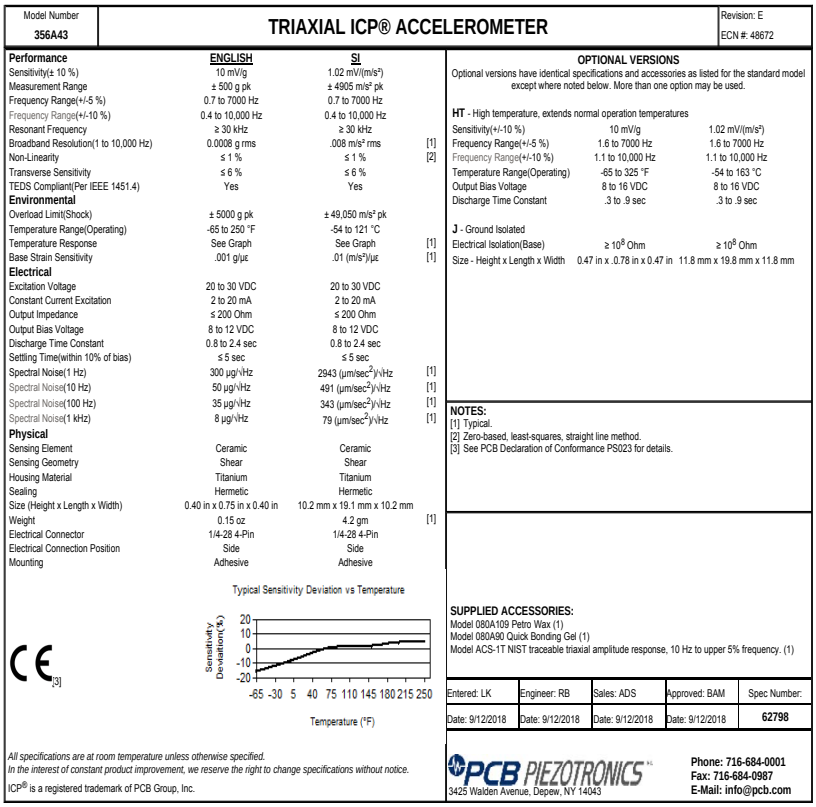

Model Number **356A43**

TRIAXIAL ICP® ACCELEROMETER

Revision: E
ECN #: 48672

Performance	ENGLISH	SI	
Sensitivity(± 10 %)	10 mV/g	1.02 mV/(m/s²)	
Measurement Range	± 500 g pk	± 4905 m/s² pk	
Frequency Range(+/-5 %)	0.7 to 7000 Hz	0.7 to 7000 Hz	
Frequency Range(+/-10 %)	0.4 to 10,000 Hz	0.4 to 10,000 Hz	
Resonant Frequency	≥ 30 kHz	≥ 30 kHz	
Broadband Resolution(1 to 10,000 Hz)	0.0008 g rms	.008 m/s² rms	[1]
Non-Linearity	≤ 1 %	≤ 1 %	[2]
Transverse Sensitivity	≤ 6 %	≤ 6 %	
TEDS Compliant(Per IEEE 1451.4)	Yes	Yes	
Environmental			
Overload Limit(Shock)	± 5000 g pk	± 49,050 m/s² pk	
Temperature Range(Operating)	-65 to 250 °F	-54 to 121 °C	
Temperature Response	See Graph	See Graph	[1]
Base Strain Sensitivity	.001 g/με	.01 (m/s²)/με	[1]
Electrical			
Excitation Voltage	20 to 30 VDC	20 to 30 VDC	
Constant Current Excitation	2 to 20 mA	2 to 20 mA	
Output Impedance	≤ 200 Ohm	≤ 200 Ohm	
Output Bias Voltage	8 to 12 VDC	8 to 12 VDC	
Discharge Time Constant	0.8 to 2.4 sec	0.8 to 2.4 sec	
Settling Time(within 10% of bias)	≤ 5 sec	≤ 5 sec	
Spectral Noise(1 Hz)	300 μg/√Hz	2943 (μm/sec²)/√Hz	[1]
Spectral Noise(10 Hz)	50 μg/√Hz	491 (μm/sec²)/√Hz	[1]
Spectral Noise(100 Hz)	35 μg/√Hz	343 (μm/sec²)/√Hz	[1]
Spectral Noise(1 kHz)	8 μg/√Hz	79 (μm/sec²)/√Hz	[1]
Physical			
Sensing Element	Ceramic	Ceramic	
Sensing Geometry	Shear	Shear	
Housing Material	Titanium	Titanium	
Sealing	Hermetic	Hermetic	
Size (Height x Length x Width)	0.40 in x 0.75 in x 0.40 in	10.2 mm x 19.1 mm x 10.2 mm	
Weight	0.15 oz	4.2 gm	[1]
Electrical Connector	1/4-28 4-Pin	1/4-28 4-Pin	
Electrical Connection Position	Side	Side	
Mounting	Adhesive	Adhesive	

Typical Sensitivity Deviation vs Temperature

[3]

All specifications are at room temperature unless otherwise specified.
In the interest of constant product improvement, we reserve the right to change specifications without notice.

ICP® is a registered trademark of PCB Group, Inc.

OPTIONAL VERSIONS

Optional versions have identical specifications and accessories as listed for the standard model except where noted below. More than one option may be used.

HT - High temperature, extends normal operation temperatures

Sensitivity(+/-10 %)	10 mV/g	1.02 mV/(m/s²)
Frequency Range(+/-5 %)	1.6 to 7000 Hz	1.6 to 7000 Hz
Frequency Range(+/-10 %)	1.1 to 10,000 Hz	1.1 to 10,000 Hz
Temperature Range(Operating)	-65 to 325 °F	-54 to 163 °C
Output Bias Voltage	8 to 16 VDC	8 to 16 VDC
Discharge Time Constant	.3 to .9 sec	.3 to .9 sec

J - Ground Isolated

Electrical Isolation(Base)	≥ 10^8 Ohm	≥ 10^8 Ohm
Size - Height x Length x Width	0.47 in x .0.78 in x 0.47 in	11.8 mm x 19.8 mm x 11.8 mm

NOTES:
[1] Typical.
[2] Zero-based, least-squares, straight line method.
[3] See PCB Declaration of Conformance PS023 for details.

SUPPLIED ACCESSORIES:
Model 080A109 Petro Wax (1)
Model 080A90 Quick Bonding Gel (1)
Model ACS-1T NIST traceable triaxial amplitude response, 10 Hz to upper 5% frequency. (1)

Entered: LK	Engineer: RB	Sales: ADS	Approved: BAM	Spec Number:
Date: 9/12/2018	Date: 9/12/2018	Date: 9/12/2018	Date: 9/12/2018	62798

PCB PIEZOTRONICS
3425 Walden Avenue, Depew, NY 14043
Phone: 716-684-0001
Fax: 716-684-0987
E-Mail: info@pcb.com

Bibliography

[1] Federal Aviation Administration, *Helicopter Flying Handbook*. FAA-H-8083-21A ed., 2012.

[2] Air Accidents Investigation Branch, "Report on the accident to Aerospatiale Eurocopter AS332 L2 super puma, registration G-REDL 11 nm NE of Peterhead, Scotland on 1 April 2009," tech. rep., 2009.

[3] M. Greaves, F. Elasha, J. Worskett, D. Mba, H. Rashid, and R. Keong, "VHM: Vibration health or alternative monitoring technologies for helicopters," tech. rep., European Aviation Safety Agency, 2012.

[4] Air Accidents Investigation Branch, "Report on the accident to aerospatiale Eurocopter AS 332L Super Puma, G-PUMI, at Aberdeen airport, Scotland on 13 October 2006," tech. rep., 2010.

[5] Air Accidents Investigation Branch, "AAIB special bulletin to EC225 LP Super Puma, G-REDW accident," tech. rep., 2016.

[6] Accident Investigation Board Norway, "Accident at Turoy, near Bergen, Norway on 29 April 2016, involving Airbus helicopters H225, LN-OJF," tech. rep., 2016.

[7] J. E. Land, "Hums-the benefits-past, present and future," in *Aerospace Conference, 2001, IEEE Proceedings.*, vol. 6, pp. 3083–3094, IEEE, 2001.

[8] Air Accidents Investigation Branch, "Report on the accident to Boeing Vertol (BV) 234 LR, G-BWFC 2.5 miles east of Sumburgh, Shetland Isles, 6 November 1986," tech. rep., 1988.

[9] Joint Helicopter Safety Implementation Team, "Health and usage monitoring systems toolkit," 2013.

[10] Civil Aviation Authority, "CAP 753," *Helicopter Vibration Health Monitoring (VHM) Guidance Material for Operators Utilizing VHM in Rotor and Rotor Drive Systems of Helicopters, First Edition June*, 2006.

[11] R. Hess, A. Duke, and D. Kogut, "The IMD HUMS as a tool for rotorcraft health management and diagnostics," in *Aerospace Conference, 2001, IEEE Proceedings.*, vol. 6, pp. 3039–3058, IEEE, 2001.

[12] J. Zhu, T. Nostrand, C. Spiegel, and B. Morton, "Survey of condition indicators for condition monitoring systems," in *Annu. Conf. Progn. Heal. Manag. Soc*, vol. 5, pp. 1–13, 2014.

[13] F. Elasha and D. Mba, "Improving condition indicators for helicopter health and usage monitoring systems," *International Journal of Structural Integrity*, vol. 7, no. 4, pp. 584–595, 2016.

[14] P. J. Rzeszucinski, *Development of Reliable Vibration-Based Condition Indicators and Their Data Fusion for the Robust Health Diagnosis of Gearboxes*. PhD thesis, The University of Manchester (United Kingdom), 2012.

[15] S. Edwards, A. Lees, and M. Friswell, "Fault diagnosis of rotating machinery," *Shock and Vibration Digest*, vol. 30, no. 1, pp. 4–13, 1998.

[16] A. K. Jardine, D. Lin, and D. Banjevic, "A review on machinery diagnostics and prognostics implementing condition-based maintenance," *Mechanical systems and signal processing*, vol. 20, no. 7, pp. 1483–1510, 2006.

[17] D. Tobon-Mejia, K. Medjaher, and N. Zerhouni, "CNC machine tool's wear diagnostic and prognostic by using dynamic bayesian networks," *Mechanical Systems and Signal Processing*, vol. 28, pp. 167–182, 2012.

[18] R. B. Randall, *Vibration-based condition monitoring: industrial, aerospace and automotive applications*. John Wiley & Sons, 2011.

[19] R. Bishop, "The vibration of rotating shafts," *Journal of Mechanical Engineering Science*, vol. 1, no. 1, pp. 50–65, 1959.

[20] H. Decker, "Crack detection of aerospace quality gears," tech. rep., 2002.

[21] J. W. Cooley and J. W. Tukey, "An algorithm for the machine calculation of complex fourier series," *Mathematics of computation*, vol. 19, no. 90, pp. 297–301, 1965.

[22] S. G. Johnson and M. Frigo, "A modified split-radix FFT with fewer arithmetic operations," *IEEE Transactions on Signal Processing*, vol. 55, no. 1, pp. 111–119, 2006.

[23] K. Fraser, "An overview of health and usage monitoring systems (HUMS) for military helicopters," tech. rep., 1994.

[24] Civil Aviation Authority, "HUMS extension to rotor health monitoring," *CAA Paper*, vol. 5, pp. 2008–, 2008.

[25] K. Pipe, "Measuring the performance of a hum system-the features that count," in *Third international conference on health and usage monitoring-HUMS2003*, p. 5, 2002.

[26] A. P. Paulson, P. Emeai, and Paulson, "Hums FACT SHEET," tech. rep., mar.

[27] D. G. Lewicki and J. J. Coy, "Vibration characteristics of oh-58a helicopter main rotor transmission," 1987.

[28] D. G. Lewicki and J. J. Coy, "Helicopter transmission testing at NASA Lewis research center," 1987.

[29] J. J. Coy, D. P. Townsend, D. G. Lewicki, and H. H. Coe, "Helicopter transmission research at nasa lewis research center," tech. rep., National Aeronautics and Space Administration Cleveland OH Lewis Research Center, 1988.

[30] I. R. Delgado, P. J. Dempsey, and D. L. Simon, "A survey of current rotorcraft propulsion health monitoring technologies," 2012.

[31] J. Bristow, "Integrated health and usage monitoring system (IHUMS)," *Aircraft Engineering*, pp. 12–13, 1992.

[32] R. Stewart, *Some useful data analysis techniques for gearbox diagnostics*. University of Southampton, 1977.

[33] J. J. Zakrajsek, D. P. Townsend, and H. J. Decker, "An analysis of gear fault detection methods as applied to pitting fatigue failure data," tech. rep., 1993.

[34] J. J. Zakrajsek and D. G. Lewicki, "Detecting gear tooth fatigue cracks in advance of complete fracture," *Lubrication Science*, vol. 4, no. 4, pp. 407–422, 1998.

[35] M. Lebold, K. McClintic, R. Campbell, C. Byington, and K. Maynard, "Review of vibration analysis methods for gearbox diagnostics and prognostics," in *Proceedings of the 54th meeting of the society for machinery failure prevention technology*, vol. 634, pp. 16–, 2000.

[36] H. J. Decker and D. G. Lewicki, "Spiral bevel pinion crack detection in a helicopter gearbox," 2003.

[37] T. R. Kurfess, S. Billington, and S. Y. Liang, "Advanced diagnostic and prognostic techniques for rolling element bearings," in *Condition Monitoring and Control for Intelligent Manufacturing*, pp. 137–165, Springer, 2006.

[38] P. Vecer, M. Kreidl, and R. Smid, "Condition indicators for gearbox condition monitoring systems," *Acta Polytechnica*, vol. 45, no. 6, 2005.

[39] L. J. Antolick, J. S. Branning, D. R. Wade, and P. J. Dempsey, "Evaluation of gear condition indicator performance on rotorcraft fleet," 2010.

[40] P. Dempsey, J. Branning, R. Arsenal, A. D. R. Wade, and A. N. Bolander, "Comparison of test stand and helicopter oil cooler bearing condition indicators," in *AHS 66th Annual Forum and Technology*, 2010.

[41] Aviation, Army and Missile Life Cycle Command, *ADS-79B-HDBK (2011), Handbook for Condition Based Maintenance Systems for US Army aircrafts*, ADS-79B-HDBK ed., 2011.

[42] E. Bechhoefer and M. Kingsley, "A review of time synchronous average algorithms," in *Annual Conference of the Prognostics and Health Management Society, San Diego, CA, Sept*, pp. 24–33, 2009.

[43] P. McFadden, "A revised model for the extraction of periodic waveforms by time domain averaging," *Mechanical systems and signal processing*, vol. 1, no. 1, pp. 83–95, 1987.

[44] A. Szczepanik, "Time synchronous averaging of ball mill vibrations," *Mechanical Systems and Signal Processing*, vol. 3, no. 1, pp. 99–107, 1989.

[45] R. B. Randall and J. Antoni, "Rolling element bearing diagnostics–a tutorial," *Mechanical systems and signal processing*, vol. 25, no. 2, pp. 485–520, 2011.

[46] E. D. S. Munck and K. R. Fyfe, "Computed order tracking applied to vibration analysis of rotating machinery," *Canadian Acoustics*, vol. 19, no. 4, pp. 57–58, 1991.

[47] K. Fyfe and E. Munck, "Analysis of computed order tracking," *Mechanical Systems and Signal Processing*, vol. 11, no. 2, pp. 187–205, 1997.

[48] S. J. Idehara, A. L. A. Mesquita, U. A. Miranda, and M. Dias Jr, "Order tracking methods analysis,"

[49] F. Bonnardot, M. El Badaoui, R. Randall, J. Daniere, and F. Guillet, "Use of the acceleration signal of a gearbox in order to perform angular resampling (with limited speed fluctuation)," *Mechanical Systems and Signal Processing*, vol. 19, no. 4, pp. 766–785, 2005.

[50] M. D. Coats and R. Randall, "Order-tracking with and without a tacho signal for gear fault diagnostics," in *Proceedings of Acoustics*, pp. 1–6, 2012.

[51] S. Braun, "The synchronous (time domain) average revisited," *Mechanical Systems and Signal Processing*, vol. 25, no. 4, pp. 1087–1102, 2011.

[52] D. Hochmann and E. Bechhoefer, "Gear tooth crack signals and their detection via the fm4 measure in application for a helicopter hums (health usage and management system)/sup/spl omega," in *Aerospace Conference, 2003. Proceedings. 2003 IEEE*, vol. 7, pp. 3313–3326, IEEE, 2003.

[53] J. Keller and P. Grabill, "Inserted fault vibration monitoring tests for a ch-47d aft swashplate bearing," in *Proceedings of the American helicopter society 61st annual forum, Grapevine, TX*, 2005.

[54] M. Delgado, J. Cusido, and L. Romeral, *Bearings fault detection using inference tools*. In-Tech, 2011.

[55] A. Bellini, F. Filippetti, C. Tassoni, and G.-A. Capolino, "Advances in diagnostic techniques for induction machines," *IEEE Transactions on industrial electronics*, vol. 55, no. 12, pp. 4109–4126, 2008.

[56] R. B. Randall, "A history of cepstrum analysis and its application to mechanical problems," *Mechanical Systems and Signal Processing*, 2016.

[57] B. P. Bogert, M. J. Healy, and J. W. Tukey, "The quefrency alanysis of time series for echoes: Cepstrum, pseudo-autocovariance, cross-cepstrum and saphe cracking," in *Proceedings of the symposium on time series analysis*, vol. 15, pp. 209–243, chapter, 1963.

[58] R. Randall, B. Peeters, J. Antoni, and S. Manzato, "New cepstral methods of signal preprocessing for operational modal analysis," in *Proc. Int. Conference on Noise and Vibration Engineering (ISMA)*, pp. –, 2012.

[59] R. Randall, N. Sawalhi, and M. Coats, "A comparison of methods for separation of deterministic and random signals," *International Journal of Condition Monitoring*, vol. 1, no. 1, pp. 11–19, 2011.

[60] N. Sawalhi and R. Randall, "Signal pre-whitening using cepstrum editing (liftering) to enhance fault detection in rolling element bearings," in *Proceedings of the 24 international congress on condition monitoring and diagnostic engineering management (comadem2011), may*, pp. 330–336, 2011.

[61] R. Randall and W. Smith, "New cepstral methods for the diagnosis of gear and bearing faults under variable speed conditions," in *ICSV23 conference, Athens*, 2016.

[62] P. Borghesani, P. Pennacchi, R. Randall, N. Sawalhi, and R. Ricci, "Application of cepstrum pre-whitening for the diagnosis of bearing faults under variable speed conditions," *Mechanical Systems and Signal Processing*, vol. 36, no. 2, pp. 370–384, 2013.

[63] J. Antoni and R. Randall, "Differential diagnosis of gear and bearing faults," *TRANSACTIONS-AMERICAN SOCIETY OF MECHANICAL ENGINEERS JOURNAL OF VIBRATION AND ACOUSTICS*, vol. 124, no. 2, pp. 165–171, 2002.

[64] J. Antoni and R. Randall, "Unsupervised noise cancellation for vibration signals: part i–evaluation of adaptive algorithms," *Mechanical Systems and Signal Processing*, vol. 18, no. 1, pp. 89–101, 2004.

[65] H. Wold, "A study in the analysis of stationary time series," 1939.

[66] D. Ho and R. Randall, "Effects of time delay, order of fir filter and convergence factor on self-adaptive noise cancellation," in *International Conference on Sound and Vibration (ICSV5), Adelaide*, pp. –, 1997.

[67] C. Ruiz-Carcel, E. Hernani-Ros, P. Chandra, Y. Cao, and D. Mba, "Application of linear prediction, self-adaptive noise cancellation, and spectral kurtosis in identifying natural damage of rolling element bearing in a gearbox," in *Proceedings of the 7th World Congress on Engineering Asset Management (WCEAM 2012)*, pp. 505–513, Springer, 2015.

[68] A. Singh, "Adaptive noise cancellation," *Central Elektronica Engineering Research Institute, University of Dehli*, pp. –, 2001.

[69] D. Ho and R. Randall, "Optimisation of bearing diagnostic techniques using simulated and actual bearing fault signals," *Mechanical systems and signal processing*, vol. 14, no. 5, pp. 763–788, 2000.

[70] B. Widrow, J. R. Glover, J. M. McCool, J. Kaunitz, C. S. Williams, R. H. Hearn, J. R. Zeidler, J. E. Dong, and R. C. Goodlin, "Adaptive noise cancelling: Principles and applications," *Proceedings of the IEEE*, vol. 63, no. 12, pp. 1692–1716, 1975.

[71] S. S. Haykin, *Adaptive filter theory*. Pearson Education India, 2008.

[72] J. Antoni and R. Randall, "Unsupervised noise cancellation for vibration signals: part ii–a novel frequency-domain algorithm," *Mechanical Systems and Signal Processing*, vol. 18, no. 1, pp. 103–117, 2004.

[73] F. Bonnardot, R. B. Randall, J. Antoni, and F. Guillet, "Enhanced unsupervised noise cancellation (e-sanc) using angular resampling application for planetary bearing fault diagnosis," *Surveillance*, vol. 5, pp. 11–13, 2004.

[74] F. Elasha, C. Ruiz-Carcel, D. Mba, and P. Chandra, "A comparative study of the effectiveness of adaptive filter algorithms, spectral kurtosis and linear prediction in detection of a naturally degraded bearing in a gearbox," *Journal of Failure Analysis and Prevention*, vol. 14, no. 5, pp. 623–636, 2014.

[75] N. Sawalhi and R. Randall, "Localized fault detection and diagnosis in rolling element bearings: A collection of the state of art processing algorithms.," *no. Hums*, 2013.

[76] T. Barszcz, "Decomposition of vibration signals into deterministic and nondeterministic components and its capabilities of fault detection and identification," *International Journal of Applied Mathematics and Computer Science*, vol. 19, no. 2, pp. 327–335, 2009.

[77] A. Swami, J. M. Mendel, and C. L. Nikias, "Higher order spectral analysis toolbox, for use with matlab, the mathworks," 1998.

[78] W. Collis, P. White, and J. Hammond, "Higher-order spectra: the bispectrum and trispectrum," *Mechanical systems and signal processing*, vol. 12, no. 3, pp. 375–394, 1998.

[79] D.-M. Yang, A. Stronach, P. MacConnell, and J. Penman, "Third-order spectral techniques for the diagnosis of motor bearing condition using artificial neural networks," *Mechanical systems and signal processing*, vol. 16, no. 2-3, pp. 391–411, 2002.

[80] E. B. Halim, M. S. Choudhury, S. L. Shah, and M. J. Zuo, "Fault detection of rotating machinery from bicoherence analysis of vibration data," *IFAC Proceedings Volumes*, vol. 39, no. 13, pp. 1348–1353, 2006.

[81] J. R. Stack, R. G. Harley, and T. G. Habetler, "An amplitude modulation detector for fault diagnosis in rolling element bearings," *IEEE Transactions on Industrial Electronics*, vol. 51, no. 5, pp. 1097–1102, 2004.

[82] Y. Nagata, "Bispectra of spike-array type time series and their application to the analysis of oceanic microstructures," *Journal of Oceanography*, vol. 34, no. 5, pp. 204–216, 1978.

[83] G. Frazer, A. Reilly, and B. Boashash, "The bispectral aliasing test," in *Higher-Order Statistics, 1993., IEEE Signal Processing Workshop on*, pp. 332–335, IEEE, 1993.

[84] M. J. Hinich and H. Messer, "On the principal domain of the discrete bispectrum of a stationary signal," *IEEE Transactions on Signal Processing*, vol. 43, no. 9, pp. 2130–2134, 1995.

[85] L. Gelman, P. White, and J. Hammond, "Fatigue crack diagnostics: A comparison of the use of the complex bicoherence and its magnitude," *Mechanical Systems and Signal Processing*, vol. 19, no. 4, pp. 913–918, 2005.

[86] X. Tian, G. M. Abdallaa, I. Rehab, F. Gu, A. D. Ball, and T. Wang, "Diagnosis of combination faults in a planetary gearbox using a modulation signal bispectrum based sideband estimator," in *Automation and Computing (ICAC), 2015 21st International Conference on*, pp. 1–6, IEEE, 2015.

[87] B. Jang, C. Shin, E. Powers, and W. Grady, "Machine fault detection using bicoherence spectra," in *Instrumentation and Measurement Technology Conference, 2004. IMTC 04. Proceedings of the 21st IEEE*, vol. 3, pp. 1661–1666, IEEE, 2004.

[88] P. McFadden and J. Smith, "Vibration monitoring of rolling element bearings by the high-frequency resonance technique–a review," *Tribology international*, vol. 17, no. 1, pp. 3–10, 1984.

[89] L. Marple, "Computing the discrete-time" analytic" signal via fft," *IEEE Transactions on signal processing*, vol. 47, no. 9, pp. 2600–2603, 1999.

[90] F. Bonnardot, R. Randall, J. Antoni, and F. Guillet, "Enhanced unsupervised noise cancellation using angular resampling for planetary bearing fault diagnosis," *International journal of acoustics and vibration*, vol. 9, no. 2, pp. 51–60, 2004.

[91] R. Dwyer, "Use of the kurtosis statistic in the frequency domain as an aid in detecting random signals," *IEEE Journal of Oceanic Engineering*, vol. 9, no. 2, pp. 85–92, 1984.

[92] V. Vrabie, P. Granjon, and C. Serviere, "Spectral kurtosis: from definition to application," in *6th IEEE International Workshop on Nonlinear Signal and Image Processing (NSIP 2003)*, 2003.

[93] J. Antoni, "The spectral kurtosis: a useful tool for characterising non-stationary signals," *Mechanical Systems and Signal Processing*, vol. 20, no. 2, pp. 282–307, 2006.

[94] J. Antoni and R. Randall, "The spectral kurtosis: application to the vibratory surveillance and diagnostics of rotating machines," *Mechanical Systems and Signal Processing*, vol. 20, no. 2, pp. 308–331, 2006.

[95] J. Antoni, "Fast computation of the kurtogram for the detection of transient faults," *Mechanical Systems and Signal Processing*, vol. 21, no. 1, pp. 108–124, 2007.

[96] B. Eftekharnejad, M. Carrasco, B. Charnley, and D. Mba, "The application of spectral kurtosis on acoustic emission and vibrations from a defective bearing," *Mechanical Systems and Signal Processing*, vol. 25, no. 1, pp. 266–284, 2011.

[97] F. Elasha, D. Mba, and C. Ruiz-Carcel, "Effectiveness of adaptive filter algorithms and spectral kurtosis in bearing faults detection in a gearbox," in *Vibration Engineering and Technology of Machinery*, pp. 219–229, Springer, 2015.

[98] A. Ming, W. Zhang, Z. Qin, and F. Chu, "Envelope calculation of the multi-component signal and its application to the deterministic component cancellation in bearing fault diagnosis," *Mechanical Systems and Signal Processing*, vol. 50, pp. 70–100, 2015.

[99] L. Zhou, F. Duan, D. Mba, W. Wang, and S. Ojolo, "Using frequency domain analysis techniques for diagnosis of planetary bearing defect in a ch-46e helicopter aft gearbox," *Engineering Failure Analysis*, vol. 92, pp. 71–83, 2018.

[100] I. W. Selesnick, R. G. Baraniuk, and N. C. Kingsbury, "The dual-tree complex wavelet transform," *IEEE signal processing magazine*, vol. 22, no. 6, pp. 123–151, 2005.

[101] N. G. Kingsbury, "The dual-tree complex wavelet transform: a new technique for shift invariance and directional filters," in *Proc. 8th IEEE DSP workshop*, vol. 8, pp. 86–, Utah, 1998.

[102] N. Kingsbury, "Complex wavelets for shift invariant analysis and filtering of signals," *Applied and computational harmonic analysis*, vol. 10, no. 3, pp. 234–253, 2001.

[103] Y. Wang, Z. He, and Y. Zi, "Enhancement of signal denoising and multiple fault signatures detecting in rotating machinery using dual-tree complex wavelet transform," *Mechanical Systems and Signal Processing*, vol. 24, no. 1, pp. 119–137, 2010.

[104] I. W. Selesnick, "The design of approximate hilbert transform pairs of wavelet bases," *IEEE Transactions on Signal Processing*, vol. 50, no. 5, pp. 1144–1152, 2002.

[105] T. T. Cai, "Adaptive wavelet estimation: a block thresholding and oracle inequality approach," *Annals of statistics*, pp. 898–924, 1999.

[106] T. T. Cai and B. W. Silverman, "Incorporating information on neighbouring coefficients into wavelet estimation," *Sankhya: The Indian Journal of Statistics, Series B*, pp. 127–148, 2001.

[107] M. S. Darlow, R. H. Badgley, and G. Hogg, "Application of high-frequency resonance techniques for bearing diagnostics in helicopter gearboxes.," tech. rep., 1974.

[108] European Aviation Safety Agency, "Annexes to the draft commission regulation on air operations - ops," tech. rep., European Aviation Safety Agency (EASA), Germany.

[109] S. C. Tee and D. Mba, "Helicopter main gearbox loss of oil performance optimisation – HELMGOP II," tech. rep., EASA, 2012.

[110] P. Mishra, "What is epicyclic gearbox – main components, working and application?," 2017.

[111] H. D. Eckhardt, *Kinematic design of machines and mechanisms*. McGraw-Hill New York, 1998.

[112] U. S. A. Aviation and M. Command, "Aeronautical Design Standard Handbook for Condition Based Maintenance Systems for US Army Aircraft Systems," tech. rep.

[113] D. L. Simon, S. Garg, G. W. Hunter, T.-H. Guo, and K. J. Semega, "Sensor needs for control and health management of intelligent aircraft engines," in *ASME Turbo Expo 2004: Power for Land, Sea, and Air*, pp. 873–882, American Society of Mechanical Engineers, 2004.

[114] M. P. Jarvis and P. Sleight, "Report on the accident to aerospatiale (eurocopter) AS332 L2 super puma registration G-REDL," *Aircraft Accident Report*, vol. 2, no. 2011, p. 24, 2011.

[115] L. Zhou, F. Duan, D. Mba, and E. Faris, "A comparative study of helicopter planetary bearing diagnosis with vibration and acoustic emission data," pp. 246–251, Institute of Electrical and Electronics Engineers Inc., 2017.

[116] L. Zhou, F. Duan, D. Mba, W. Wang, and S. Ojolo, "Using frequency domain analysis techniques for diagnosis of planetary bearing defect in a ch-46e helicopter aft gearbox," *Engineering Failure Analysis*, vol. 92, pp. 71–83, 2018.

[117] X. Tian, J. X. Gu, I. Rehab, G. M. Abdalla, F. Gu, and A. D. Ball, "A robust detector for rolling element bearing condition monitoring based on the modulation signal bispectrum and its performance evaluation against the kurtogram," *Mechanical Systems and Signal Processing*, vol. 100, pp. 167–187, 2018.

[118] B. G. Cameron, "Final report on CH-46 aft transmission seeded fault testing," *Westland Helicopters Ltd, UK, Research Paper RP907*, 1993.

[119] B. D. Rex, "Non-invasive detection of CH-46 aft gearbox faults using digital pattern recognition and classification techniques," tech. rep., Naval Aacademy Annapolis MD, 1999.

[120] L. Zhou, F. Duan, E. Faris, and D. Mba, "Seeded planetary bearing fault in a helicopter gearbox—a case study," in *International Conference Design and Modeling of Mechanical Systems*, pp. 495–505, Springer, 2017.

[121] A. Ricardo Mauricio, L. Zhou, D. Mba, and K. Gryllias, "Vibration based condition monitoring of helicopter gearboxes based on cyclostationary analysis," in *Proceedings of ASME Turbo Expo 2019 Turbomachinery Technical Conference and Exposition*, ASME.